Eindhoven University of Technology

MASTER

# Predictive analysis for selective photothermolysis
## modeling, simulation and analysis

Regis, M.

*Award date:*
2014

Link to publication

**Disclaimer**
This document contains a student thesis (bachelor's or master's), as authored by a student at Eindhoven University of Technology. Student theses are made available in the TU/e repository upon obtaining the required degree. The grade received is not published on the document as presented in the repository. The required complexity or quality of research of student theses may vary by program, and the required minimum study period may vary in duration.

**General rights**
Copyright and moral rights for the publications made accessible in the public portal are retained by the authors and/or other copyright owners and it is a condition of accessing publications that users recognise and abide by the legal requirements associated with these rights.

- Users may download and print one copy of any publication from the public portal for the purpose of private study or research.
- You may not further distribute the material or use it for any profit-making activity or commercial gain


Dual Master

Industrial and Applied Mathematics

M. Sc. Thesis

# Predictive Analysis for Selective Photothermolysis: Modeling, Simulation and Analysis

*Author*
Marta Regis

*Supervisors*
Dr. habil. Adrian Muntean
Dr. Mounir Zeitouny
Prof. Dr. Luigi Preziosi

Publishing date: September 2015

# Abstract

We analyze the temperature increase in the skin-hair structure induced by a light-based device. The application aims to damage the hairs inside the skin delivering sufficient light energy. The process is known as photothermolysis.

We use a Monte Carlo approach to simulate the light diffusion in biological tissues. Then, we solve the system of balance equations describing the heat conduction inside the skin with COMSOL. We obtain the temperature profiles that allow the estimation of derived physical values such as the Arrhenius damage integral - a useful quantity for the forecast of treatment efficacy. Because of the high dimensional parameter space, we introduce statistical methods such as multiple linear regression and artificial neural networks. The performance of both models is evaluated through the correlation between the output and the measured efficacy.

From a mathematical perspective, we investigate the weak solvability of the quasi-linear heat conduction model and its response to small perturbations in the parameters. Additionally, we give hints on a well-posed strategy to identify the unknown coefficients involved in the photoepilation process. The presentation of the arguments follows the phases of the photothermolysis process as well as the steps I made during these last challenging six months between Philips Research, in the department of Personal Care and Wellness, and CASA (Centre for Analysis, Scientific computing and Applications) with the Department of Mathematics of TU Eindhoven.

*Keywords:* Monte Carlo, Arrhenius damage integral, predictive analysis, bioheat transfer, semi-linear parabolic equations, inverse problem

2010 Mathematics Subject Classification: 35K57, 31A25, 62J05, 97K80.

2010 Physics and Astronomy Classification Scheme: 02.60.Cb, 87.10.Rt, 87.50.W-.

# Acknowledgments

A chi mi ha insegnato qualcosa che
risplende dentro di me...
Jovanotti

I would like to thank here all those people who made the realization of this manuscript possible. First of all, I warmly acknowledge Dr. Jim Coombs and Dr. Natallia Uzunbajakava who gave me the opportunity of doing my internship at Philips Research in the department of Personal Care and Wellness, and the whole team for making me feel comfortable every day.

A warm thank you is for my three supervisors, because their help goes much far beyond this manuscript. Prof. Adrian Muntean, because since I reached Eindhoven you introduced me to CASA activities and made me try the flavor of a research department. You also helped me in my dream of having an internship in a company before leaving the University and followed up the work with your expert mathematical supervision.
Dr. Mounir Zeitouny and your original way of teaching. What I learnt in Philips thanks to you contributes in a wider way than the only technical achievements: tips on how to behave in a company, how to communicate, what to expect, what to dream.
Prof. Luigi Preziosi, because without you this year in Eindhoven would have not even be possible; even from far, I have always relied on your expert advices and full availability.

A heartily thank you to the members of the examination committee Dr. Sorin Pop and Dr. Martijn Anthonissen, for the prompt precious technical advices and the great patience in waiting the manuscript.
To Dr. Calina Ciuhu-Pijlman, your smile and expert advise are always ready to help me in more or less technical matters and for nice moments together. Because even when your agenda is completely booked, you have time for me.

To my family, Lucia, mum and dad. Because you trust in me even when I do not and push me to do always better. Although sometimes we doubt, we know we are an excellent team.
To my friends and especially to Cristian because nonetheless my crazy decisions, my stubbornness in following a dream and the distance, you are here (distance means so little when people mean so much). To all my new friends here in Eindhoven, because everyone of you was necessary in this great last year of technical and personal growth. Far from home, family and friends, you are the best surprise I could have wished for. Thanks to my grandma Lucia, because from the sky you are daily supporting me and you give me the strength to pursue my dreams.

Thank you all, because everyone was essential in the realization of this work. I feel so lucky I am surrounded by such special people. Your contribution will be part of me forever... shining.

Marta

# Contents

# Chapter 1

# Introduction

Since the laser radiation was introduced by Maiman in 1960, numerous techniques for medical applications have emerged. Nowadays devices emitting high power light are used in ophthalmology, dentistry, gynecology, urology, neurosurgery, cardiology, dermatology, orthopedics and cancer treatment.

The focus of this work is the role played by light-induced thermal interactions in dermatology and especially in the epilation based on selective photothermolysis: the treatment of a selected structure or tissue using specific settings. By tuning the wavelength and the pulse duration it is possible to maximize the absorption of light into the target area and the corresponding energy produces sufficient heat to damage the structure while letting the surroundings relatively untouched. The requirements are determined by the optical and thermal properties of the target area: device parameters must be adjusted in order to reach the goal with the minimal side effect (e.g. skin redness, hypo/hyper pigmentation, burning and pain). Many research studies focused on the effects of the interaction between light and tissue, but the exact description of the underlying photo-biology processes is still a challenge.

Light-induced thermal interactions can be addressed by modeling two processes: as light propagates in tissues and gets partially absorbed, it is converted into heat and becomes a source in the heat transfer inside the skin. Therefore, an in-house Monte Carlo model is used to map the photons diffusion in the tissue and to calculate the rate of absorbed energy. An essential description is presented in Chapter 3, after a short introduction of the needed prerequisites in Chapter 2. Once we have identified the absorbed energy, this is converted into the heat source. In Chapter 4 we propose a model for heat conduction inside the skin-hair structure and we study the possible inclusion of some phase transitions. By using COMSOL Multiphysics, we find the numerical solution which approximates the temperature rise inside the light-irradiated tissue. The modeling platform is used to generate simulated values to be compared with the clinical data. Two statistical methods are built: a multiple linear regression model and a neural network. Both show high correlation between the computed and the measured values of the treatment efficacy (Chapter 5).
This achievement is both a validation of the optothermal model and a new potential tool in the forecast of the clinical efficacy.
Finally in Chapter 6, with a rigorous mathematical approach, we analyze the parabolic equations governing the heat conduction process. We prove the existence, uniqueness and continuous dependence on the data for a linear case. Then we relax some hypotheses to get closer to the physical problem. We introduce the analogous treatment for the quasi-linear case and give inputs for further analysis. Finally, we propose the application of these achievements in the study of the inverse problem which can be used in the identification of non-measurable parameters.

Appendix A has to be used as a reference for the definitions of the new notions introduced in the Chapters.

# Chapter 2

# Preliminaries

In this manuscript, we study the light-induced thermal interaction in human skin. The application targets the usage of light-based cosmetic devices for hair removal commonly known as photoepilation devices. Photoepilation is based on the principle of selective photothermolysis; this term refers to the precise targeting of a structure or tissue using a specific light wavelength with the intention of light absorption into that target area alone. The energy directed to the target area produces sufficient heat to damage the target while allowing the surroundings to remain untouched. In our particular application for hair removal, the target area is the hair and the surrounding is the skin.

In this Chapter we provide information about skin, hair and light that is relevant for the photo epilation topic. In addition, we briefly show a photoepilation device that is currently on the market.

## 2.1 The skin

Skin is the soft outer covering of vertebrates; it has the function of first line in the defense from external factors, insulation, temperature regulation, sensation and the production of vitamin D folate. Its structure is complex and in mammals it is composed of many layers with specific properties, reflecting the ability of carrying out these many functions (see for example [1]).
From the external surface to the interior, the layers are epidermis, dermis and subcutaneous layer (Figure 2.1a).

The epidermis is the part interfacing with the environment and it is composed of dead, keratinized cells; its depth can vary between 0.05 mm and 1.5 mm depending on the body area. It is composed up to 30% of water and it is responsible of the skin tanning since it contains melanin in the melanosomes which discriminate the skin color with their size, concentration and arrangement. With UV radiation exposure, the number of melanosomes in the keratinocytes increases while letting their distribution largely unaffected. Despite this granular organization we consider the melanin to be homogeneously distributed.

The dermis is elastic and is primarily made up of loosely interwoven connective tissue, with about 80% of water. This layer reaches up to 1.4 mm depth and comprehends structural components such as collagen, elastic fibers and extrafibrillar matrix; it also contains mechanoreceptors that provide the sense of touch and heat, hair follicles, sweat glands, sebaceous glands, apocrine glands, lymphatic vessels and blood vessels. Those blood vessels provide nourishment and waste removal for both dermal and epidermal cells.

The subcutis is made of loose connective tissue, in which tiny fat pads are stored. It is traversed by fibrous bands which anchor the skin to the layer of tissue below.

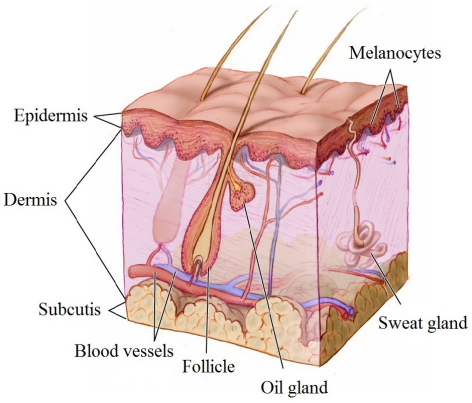


(a) Skin anatomy.

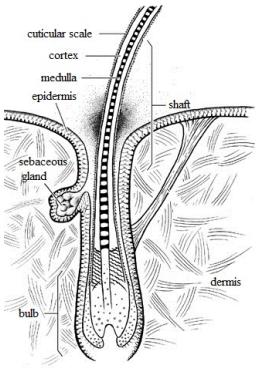


(b) Hair anatomy.

Figure 2.1: Skin and hair anatomy.

## 2.2 The hair

Mammalian skin produces hair almost everywhere with different thickness, length, diameter, depth, density and color; see [2] for details.
The hair is a protein filament partly inside the skin with an external extension called hair shaft (Figure 2.1b). The internal part, the hair follicle, is a highly dynamic organ found only in mammals with an almost unique ability of self regeneration. It can be divided in three anatomical compartments: the infundibulum (from the skin surface to the sebaceous duct), the isthmus (between the sebaceous gland and the exertion of arrector pilli muscle) and the inferior segment, consisting of the suprabulbar area and the hair bulb.

The hair bulb consists of extensively proliferating keratinocytes and pigment-producing melanocytes of the hair matrix that surround the dermal papilla, which contains specialized fibroplasttype cells embedded in an extracellular matrix and separated from the keratinocytes by a basement membrane. The hair matrix keratinocytes move upwards and differentiate into the hair shaft, as well as into the inner root sheath; the melanocytes transfer pigment into the developing hair giving its color.

Externally the hair shaft is a thin and flexible tube of dead, fully keratinised epithelial cells. It has a cylindrical structure and is composed by the medulla, the cortex and the cuticle, sorted by increasing radius order. The medulla is the central part of larger hairs, such as beard hairs, and is an open, unstructured region. The mechanical strength primarily comes from the cortex composed of longitudinally arranged fibers, highly structural and organized. This middle layer contains the melanin coloring the fiber (again depending on the number, distribution and type of the melanin granules). The cuticle is the outer root shaft, a complex structure covered with a single molecular layer of lipid that makes the hair repel water and gives the white/transparent characteristic color to this component. The structure of the hair is not completely filled since there is an empty volume between the cortex and the cuticle.

The tubular glands and the sweat glands have the function of producing watery fluids that cool the body by evaporation; the sebaceous glands at the opening of the hair produce a fatty secretion that lubricates the hair and prevents it from dying.

## 2.3 The light

The light, with its wave-particle duality, can be treated either as a stream of particles (photons) or as an electro-magnetic wave. The first approach allows the understanding of the quantum nature of light: a system absorbing light is subjected to an energy increase which is wavelength dependent (see [3]). When light is seen as a wave on the other hand, it is easier to explain the

constructive/destructive interferences that are observed in natural phenomena. The duality is solved with the relation which states the proportionality of the photon energy to the frequency of the corresponding wave:

$$E = h\nu = \frac{hc}{\lambda}, \tag{2.1}$$

where $E$ is the photon energy, $h$ is Planck's constant ($6.62 \cdot 10^{-34}$ J $\cdot$ s $= 4.14 \cdot 10^{-15}$ eV $\cdot$ s), and $\nu$ is the frequency of the wave (which is related to the wavelength, $\lambda$, by the speed of light, $c$; specifically, $c = \nu\lambda$).
Understanding the interactions of light with materials requires the knowledge of both the wave and particle nature of light. A key observation in dermatological applications of light is that as the wavelength increases, the photon energy decreases. One sees that traversing the light spectrum from the UV to the far-IR, the photon energy decreases significantly. Thus, 500 nm light corresponds to 2.48 eV photons, whereas 1 $\mu$m light to 1.24 eV photons. This difference in energy discriminate whether the use of light can be dangerous or not: high energy photons can induce chemical alterations which are not possible at lower energies.

The selective photothermolysis is based on the proper choice of the device settings and especially of the specific wavelength. According to the observations made before, the choice must respect safety constraints and also address the highest possible absorption in the selected area. For hair removal usually a wavelength in the range $570 - 1100$ nm is chosen and it can be a single wavelength (laser) or IPL (Intense Pulse Light) broadband, a mix of various wavelengths.

To mimic a significant quantity of energy the light source used in the treatment is modeled as a light beam. This is composed of tenths of million of photon packets (or beamlets), entities averaging the energy and the behavior of millions of photons. This approach allows us to simulate in the macroscopic scale. As an example, assume we want to model a light source with optical energy of 1 J. According to (2.1), the energy of a single photon depends only on the frequency $\nu$ or, inversely, on the wavelength $\lambda$. Thus, we need a number $N$ of photons given by

$$1 \text{ J} = N \cdot h \cdot \nu \longrightarrow N = \frac{1 \text{ J}}{h \cdot \nu}. \tag{2.2}$$

For example, for a red light with wavelength $\lambda = 600 \cdot 10^{-9}$, $N$ is

$$\nu = \frac{c}{\lambda} = \frac{3 \cdot 10^8}{600 \cdot 10^{-9}} = 0.5 \cdot 10^{15} \longrightarrow N = \frac{1 \text{ J}}{h\nu} = \frac{1}{6 \cdot 10^{-34} \cdot 0.5 \cdot 10^{15}} \sim 3 \cdot 10^{19}, \tag{2.3}$$

which is hard to be managed computationally; in addition this would require a quantum/molecular scale for the model, making the problem non implementable.
In the remainder we may use the terms photon, beamlet and photon packet as synonyms, but all of them refer to the photon packet when non made explicit.

## 2.4 The device

In Figure 2.2 we show a sample of photoepilation device. This kind of devices has been launched by Philips a couple of years ago under the Philips Lumea series. It is mainly used by female consumers and has different versions to accomplish the treatment of various areas. The device flashes only when it is pressed against a relatively hard surface (e.g. skin) for safety reasons. It is used in a step-and-flash mode, meaning the non continuous application from one point to the adjacent one. The flashing period is of about 3 seconds.
Consumers have to shave (mechanically) before the usage to avoid the burning of the hair on top of the skin and malodor.

Figure 2.2: Light-based device for hair removal - Lumea.

## 2.5 Conclusion

Relevant properties of skin and hair are introduced providing fundamental understanding of photoepilation. Necessary information of light in the dermal applications is provided. As light is the primary physical stimulus in the hair removal process, we aim to study photon diffusion in the skin. This will be addressed in Chapter 3, where we provide a description of light propagation in complex media. The main tool of this is the Monte Carlo analysis.

# Chapter 3

# Monte Carlo simulation for light diffusion in complex media

In this Chapter we introduce the Monte Carlo simulation for light diffusion in complex media. Monte Carlo (MC) is a stochastic method used here to simulate the photon propagation in biological tissues; see for instance [4, 5]. With this method we compute the rate of initial energy which is absorbed by the skin, as a function of the wavelength-dependent optical properties of the tissue. The amount of gained energy is then used as input to calculate the temperature rise in the light-irradiated tissue. In addition, a Design of Experiment is outlined to give guidelines on future investigations about the uncertainty of the optical parameters.

## 3.1 Monte Carlo method

The Monte Carlo class includes a large number of computational algorithms that give the probabilistic distribution of an unknown entity using repeated random sampling.
The algorithm is essentially based on two steps:

1. construction of a stochastic model with expected value equating the one of the physical quantity which has to be determined;

2. estimation of the expected value by averaging multiple independent samples representing the random variable. The samples are constructed with random numbers following the distribution of the variable which must be evaluated.

The Monte Carlo method relies on the random sampling of variables from probability distributions. First we choose a probability density function $p(\chi)$ defining the distribution of $\chi$ over an interval $(a, b)$. Then to sample $\chi$ we choose a value repeatedly based on the density function $p$; to do so we generate a pseudo-random number $\zeta$ uniformly distributed in $[0, 1]$ with the use of the computer. Then, when the chosen PDF is other than the uniform one, we sample $\chi$ by solving

$$\int_0^{\chi} p(\chi')d\chi' = \zeta, \qquad \zeta \in (0, 1). \tag{3.1}$$

Since the left-hand side represents the cumulative distribution function $P(\chi)$, we have

$$P(\chi) = \zeta. \tag{3.2}$$

This means that if $P(\chi)$ is sampled uniformly by $\zeta$ between 0 and 1, the inverse transformation correctly samples $\chi$ as

$$\chi = P^{-1}(\zeta). \tag{3.3}$$

This algorithm is called inverse distribution method (IDM).
The application of the Monte Carlo method to light diffusion in complex media is based on the conception of light as a stream of particles while the polarization and wave phenomena are neglected. The optical path of each photon is traced through the medium; the trajectories are modeled as persistent random walks and the directions at each step depend only on the previous one.
The Monte Carlo simulation presented here mimics the photon transport in a multi-layered tissue infinitely wide with parallel layers, as depicted in Figure 3.1. Although in reality we do not have

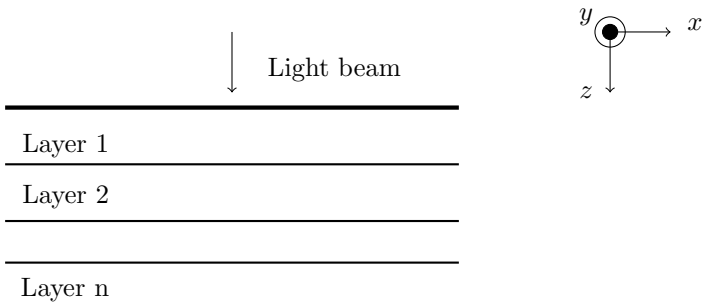


Figure 3.1: Multi-layered tissue and Cartesian coordinate system.

infinite extensions, this assumption is accepted when the light beam is extremely narrow; this way the tissue appears much wider than the spatial extent of the photon distribution.
Each layer is characterized by its thickness, refractive index $n$, absorption coefficient $\mu_a$, scattering coefficient $\mu_s$ and the anisotropy factor $g$; the refractive index of the ambient medium above the tissue is necessary as well. For the definitions and units of measure, we refer to Appendix A.

Two coordinate systems are simultaneously used: a Cartesian and a moving spherical one. The first is shown in Figure 3.1; it is adopted to trace photons positions and has the $z$-axis perpendicular to the tissue surface, coincident with the $xy$-plane. The origin is set at the launch position. The second is employed to sample the changes in the propagation direction; its $z$-axis is dynamically aligned with the photon propagation direction. After the random direction is determined, it is also updated in terms of the directional cosines in the Cartesian coordinate system.

As Monte Carlo simulation uses a stochastic approach, a large number of photon packets is required in order to obtain the minimal statistical spread between various runs. We choose $N = 10^7$ photons packets to be used throughout the simulations since this number is found to deliver stable statistical results (we follow a previous study [6]).

After the launch the path of each photon packet is traced through the encountered media. The flowchart of the method is sketched in Figure 3.2 and follows [4, 5]. Depending on the interaction point reached at each step, the photon packet can either be reflected or transmitted and in the latter case transmission implies absorption and scattering; the type of interaction with the matter depends on the optical properties of the tissue and it is modeled by rules expressed as probability distributions: with the use of the inverse distribution method we determine the step size, the change in the traveling direction, the reflection/refraction choice. Due to the interactions the photon packet loses some of its energy after each step till when it reaches a negligible value, artificially set to zero. The packet representation (mentioned in Chapter 2) instead of single photons, increases the number of interactions needed before each element has no more energy left.

### 3.1.1 Photon representation

The photon packets, representing multiple individual photons, are treated as statistical units: at each step they are characterized by their weight $w \in [0, 1]$, their position $P(x, y, z)$ and the direction for their next step $D = [\mu_x, \mu_y, \mu_z]$ given by the directional cosines in the Cartesian

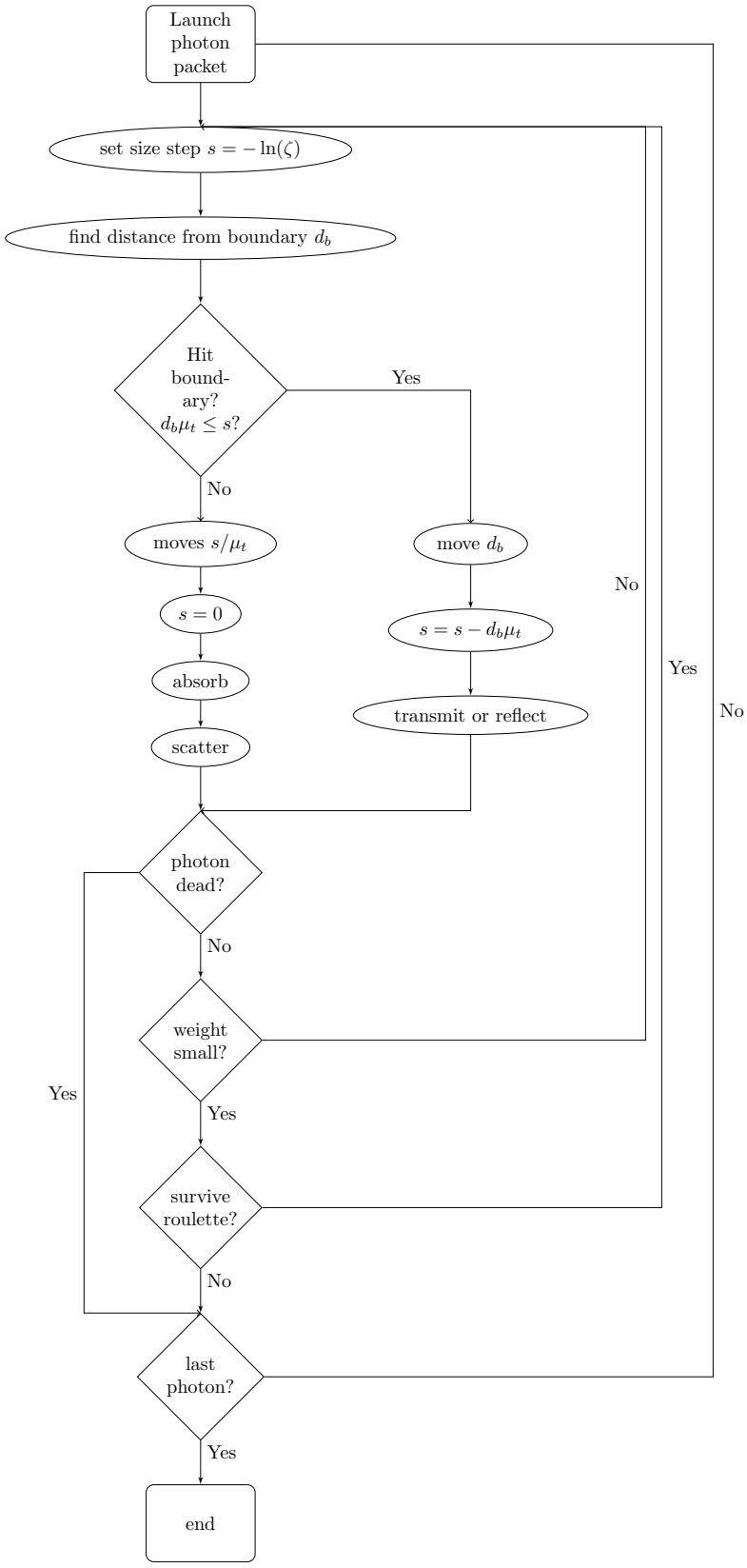


Figure 3.2: Flow chart for the Monte Carlo method for light diffusion in complex media (see [4]).

coordinate system. Position and direction are initialized to the launch settings while the weight is set to one (full statistical packet).

### 3.1.2 Direct reflection of photons

When a photon packet is launched and encounters a different medium on its path, it can be reflected if the indexes of refraction of the two adjacent media are mismatched. Direct reflection is assumed to occur whenever the angle of incidence ($\theta_i$ in Figure 3.3) is bigger than the critical angle

$$\theta_c = \arcsin(n_t/n_i), \tag{3.4}$$

where $n_i$ is the index of refraction for the "incident medium", the one the light is traveling through, and $n_t$ is the index of refraction for the "transmission medium", the new encountered layer. The weight of those who are directly reflected is set to zero since their path is no more related to the considered tissue while the weight of the remaining ones is updated according to

$$w = 1 - R_{sp}. \tag{3.5}$$

Here the specular reflectance $R_{sp}$ is determined by the Fresnel's law (3.6).

$$\begin{aligned} R_s &= \left( \frac{n_i \cos\theta_i - n_t \cos\theta_t}{n_i \cos\theta_i + n_t \cos\theta_t} \right)^2 \\ R_p &= \left( \frac{n_i \cos\theta_t - n_t \cos\theta_i}{n_i \cos\theta_t + n_t \cos\theta_i} \right)^2 \\ R_{sp} &= \frac{R_s + R_p}{2} \end{aligned} \tag{3.6}$$

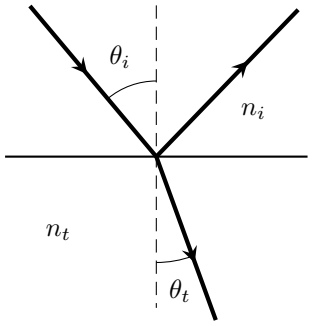


Figure 3.3: Fresnel Law for reflection and refraction.

This equations describe the behavior of light when moving between media of differing refractive indexes. In fact, when light diffuses from a medium of a given refractive index $n_i$ into a second medium with refractive index $n_t$, both reflection and refraction of the light may occur. The Fresnel equations describe what fraction of the light is reflected and what fraction is refracted (i.e. transmitted along a different direction). The equations assume the interface is flat, planar and homogeneous, and that the light is a plane wave. Then, the calculations depend on the polarization of the incident light: $R_s$ refers to the $s-$polarized part, which means polarized with its electric field perpendicularly to the plane containing the incident, reflected and refracted rays. $R_p$ refers to the light polarized with its electric field parallel to the plane.

The subscripts respect the convention of incident and transmission index of refraction ($n_{\{i,t\}}$) and incident and transmission angle ($\theta_{\{i,t\}}$) and they are related according to the Snell's law which states that the ratio of the sine of the angle of incidence to that of the angle of refraction is a constant (known as the index of refraction),

$$n_i \sin\theta_i = n_t \sin\theta_t. \tag{3.7}$$

Note that the angle of incidence is directly obtained from the launch properties, $\theta_i = \arccos(|\mu_z|)$. Direct reflection is specific to the first phase, from the photon launch in the ambient medium to the external surface; later at each step there will be only two possibilities: either internal reflection or scattering-transmission. First, it is necessary to determine the next reached interaction point.

### 3.1.3 Choice of the step size

At every iteration the distance of each photon from the boundaries is computed and a random number representing the step size is generated from a uniform distribution. The comparison between these two quantities discriminates whether the photon reaches the adjacent boundaries (see Section 3.1.4) or lies inside the layer where currently is (Section 3.1.5).

Note that the layer corresponding to the photon position is delimited by an upper and lower boundary; the distance $d_b$ is computed from the one towards which the photon is directed according to the direction $D$ in the $z$ direction,

$$d_b = \begin{cases} \dfrac{z_0 - z}{\mu_z} & \mu_z < 0 \\ \infty & \mu_z = 0 \\ \dfrac{z_1 - z}{\mu_z} & \mu_z > 0 \end{cases} \tag{3.8}$$

where $z_0$ and $z_1$ are the quotes of the two planes representing the current layer's boundaries.
The step size is randomly generated as the logarithm of a sampling from a uniform distribution $\zeta$

$$s = -\ln(\zeta). \tag{3.9}$$

Then, the random step is compared to the distance,

$$d_b \mu_t \leq s, \tag{3.10}$$

where $\mu_t$ is the total attenuation coefficient (see Appendix A for the definition).
It is worth noticing that the formulation of this condition avoids dividing by $\mu_t$ so that its validity is general, including transparent media (case with $\mu_t = 0$).

### 3.1.4 Behavior of photons at the boundaries

When the inequality (3.10) is satisfied the random step size is enough (at least equal to the distance) to make the photon reach the boundary following its direction. In this case the portion of the step necessary to reach the boundary is treaded, the position is updated

$$\begin{cases} x' = x + \mu_x d_b \mu_t \\ y' = y + \mu_y d_b \mu_t \\ z' = z + \mu_z d_b \mu_t \end{cases} \tag{3.11}$$

and the remaining part of the step size is recorded:

$$s = s - d_b \mu_t. \tag{3.12}$$

The photon will complete the prescribed step size along its direction in case it avoids reflection.

The reflection/refraction decision is again up to a comparison between a random generated number and the specular reflectance $R_{sp}$ obtained from the Fresnel's law (3.6),

$$\zeta \leq R_{sp}. \tag{3.13}$$

When this inequality is satisfied, then the photon is reflected: its position is unchanged and the direction is set at the opposite value in the third component

$$(\mu_x, \mu_y, \mu_z) \longrightarrow (\mu_x, \mu_y, -\mu_z).$$

Otherwise the photon packet is transmitted: it propagates in the refraction direction inside the next layer completing the random step and the new direction is set to

$$\begin{aligned} \mu'_x &= \mu_x \frac{\sin\theta_t}{\sin\theta_i} = \mu_x \frac{n_i}{n_t}, \\ \mu'_y &= \mu_y \frac{\sin\theta_t}{\sin\theta_i} = \mu_y \frac{n_i}{n_t}, \\ \mu'_z &= \operatorname{sign}(\mu_z) \cos\theta_t. \end{aligned} \tag{3.14}$$

### 3.1.5 Behavior of photons inside the tissue layer

In case the length of the path is not enough to reach a boundary (i.e. condition (3.10) is not satisfied), the photon packet lies inside the tissue where it currently is. In this case, it treads the random distance: the new coordinates are given by

$$\begin{cases} x' = x + \mu_x s \\ y' = y + \mu_y s \\ z' = z + \mu_z s \end{cases} \tag{3.15}$$

and the step $s$ is reset to zero. At its arrival at the interaction point it is subjected to absorption and scattering; the first term refers to the attenuation of the electromagnetic wave (due to a partial conversion of the light energy into heat motion or certain vibrations of molecules of the absorbing material) and is modeled through a reduction of the photon weight,

$$\Delta w = w \frac{\mu_a}{\mu_a + \mu_s}, \qquad w' = w - \Delta w, \tag{3.16}$$

where $\mu_a$ and $\mu_s$ are the optical properties (absorption and scattering coefficients respectively) of the current medium - see Appendix A.
The scattering is the effect of the interaction between the photon packet and the matter, which modifies the treading direction in a random way. The azimuthal angle ($0 \leq \phi \leq 2\pi$) is always completely random and generated from a uniform distribution

$$\phi = 2\pi\zeta, \tag{3.17}$$

while for the polar angle ($0 \leq \theta \leq \pi$) we use the Henvey-Greenstein phase function. It is a function which, by the variation of one parameter $0 \leq g \leq 1$, ranges from isotropic scattering to forward scattering. In the first case, with the coefficient of anisotropy $g = 0$ (see Appendix A) and no preferred diffusion direction, the cosine of the angle is given by

$$\cos\theta = 2\zeta - 1, \tag{3.18a}$$

with $\zeta$ a random number from uniform distribution. On the other hand, the Henvey-Greenstein function in the anisotropy case $g \neq 0$, defines the cosine of the polar angle as

$$\cos\theta = \frac{1}{2g}\Big(1 + g^2 - \Big(\frac{1-g^2}{1-g+2g\zeta}\Big)^2\Big). \tag{3.18b}$$

### 3.1.6 Photon termination

The packet representation increases the number of interactions needed before the total energy is lost. We stop following the photons either when their energy is below a certain threshold or when they move beyond the layers which are relevant for the analysis. In both cases we report the photon death artificially by setting its weight to zero.

For the first termination condition, since the threshold is artificially defined and some small energy is arbitrarily neglected, a random method called Russian Roulette is used to respect energy conservation. Calling $\zeta$ a pseudo-random number (sample from uniform distribution) and defining an arbitrary integer $m$, we check the weights imposing

$$w = \begin{cases} m\, w & \zeta \leq \dfrac{1}{m} \\ 0 & \zeta > \dfrac{1}{m} \end{cases}. \tag{3.19}$$

The second termination condition is set because our analysis is focused on the absorption inside the skin. We want to estimate how many photon packets reach the interior crossing the epidermis and the dermis and avoiding reflection. This is a measure of the energy increase inside the skin. The weight of photons which went across the dermis is cumulated in the amount of absorbed energy without caring about the specific path treaded in deeper layers. Afterwards, the weight is set to zero.

## 3.2 Monte Carlo simulation

We implemented the Monte Carlo algorithm for light diffusion in multi-layered tissues presented in the previous sections.
The structures are dynamically allocated so that the number of tissue layers can be varied at each simulation. It requires as input the optical properties for each layer (including the ambient medium), the number of photon packets, the position and direction of the launch. The output is the absorption map, a matrix indicating the amount of gained energy in each of the elemental volumes in which the skin-hair structure is discretized.

We show here the result of a run simulation. We consider a single layer tissue of 0.02 cm depth, with coefficient of anisotropy $g = 0.75$, scattering coefficient $\mu_s = 90\ \text{cm}^{-1}$ and absorption coefficient $\mu_a = 10\ \text{cm}^{-1}$. The skin-hair structure is exposed to the air and the chance of direct reflection is avoided by setting the same index of refraction for the ambient medium and the skin. We then simulate the launch of a point-wise light beam, composed of $N = 10^7$, with normal direction with respect to the skin surface. The overall gain of energy (the energy of all the photons which are absorbed in some parts of the skin-hair structure) is about the 70% of the delivered amount.

In Figure 3.4 we show the random walks of some photon packets.

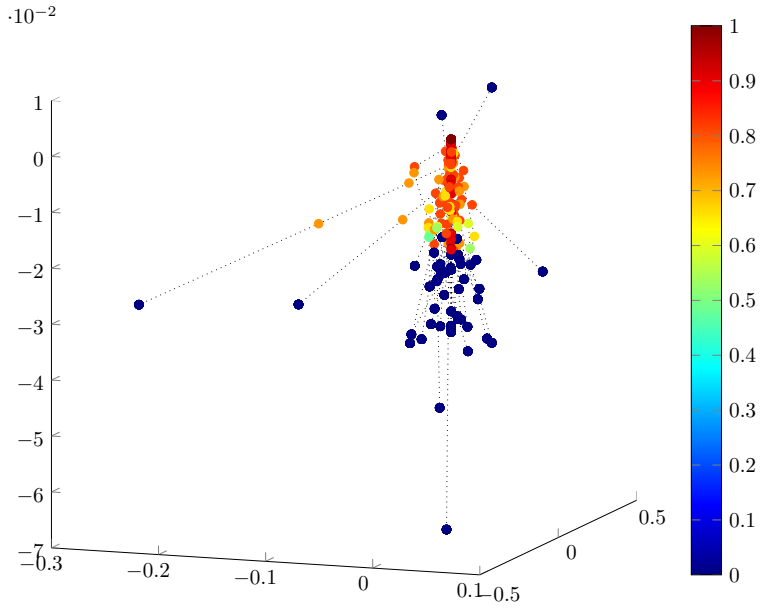


Figure 3.4: Random walk of some photon packets.
The dots are the reached interaction points and the color is indicative for the weight.

The light beam is launched from the origin $(0, 0)$; from here the dashed lines trace the route from one interaction point to the next one for each of the considered photons. The 3D reference system detects the volumetric domain, with the $x$, $y$ and $z$ axis corresponding to the width, length and depth of the skin-hair structure. The color of the dots at each step is representative of the weight of the photon packet, function of the residual energy. A red point represents a full statistical packet; due to absorption and scattering probabilities, the photon packets lose weight and their color changes in yellow, green and finally blue when the energy left is negligible. As we can see, some photons are traced outside the skin-hair structure. Those are reflected units and their blue color shows that they are considered as dead.
The evaluation of the weight loss in each voxel of the considered domain gives as a result the absorption map mentioned earlier. In Figure 3.5, we show the one obtained in our simulation

case. It illustrates a slice plot through the volumetric domain: the horizontal axis represents the width while the vertical is the depth inside the tissue. The color is proportional to the local rate of absorption; from the black representing no gained energy through the red to the yellow and white representing the maximum gain of energy. From dark to light colors we go in more absorbing tissues. The chosen wavelength (800 nm) targets the melanin and this can be seen in terms of increased absorption mainly in the hair structure and secondarily in the epidermis, where the melanin molecules are present. As expected, the black color shows that the launch of light has no effect on the dermis.

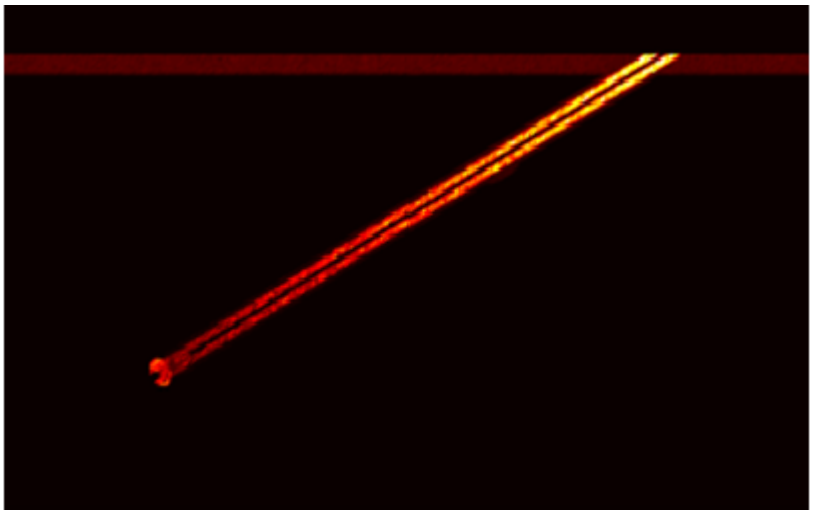

Figure 3.5: Slice plot through the skin-hair structure.
The color depends on the absorbed energy: the lighter compartments are the most absorbing.

As we know the absorption rate to be strongly dependent on the optical parameters of the skin-hair structure, we depict a Design of Experiment to estimate its variability.

## 3.3 Design of Experiment

The term Design of Experiment refers to the analysis of the sensibility of the response to the variability of the input parameters. The purpose of this section is the understanding of how much the rate of absorption changes when a kind of uncertainty in the tissue optical properties is introduced. We consider typical values taken from the literature for the four optical parameters: absorption coefficient $\mu_a = 150$ cm$^{-1}$, scattering coefficient $\mu_s = 11$ cm$^{-1}$, anisotropy factor $g = 0.85$ and index of refraction $n = 1.548$. We introduce an uncertainty of $\pm 15\%$ around the typical values and analyze the corresponding rate of absorption. The range of variation of the parameters is small and is used as a picket, in order to understand whether an ampler Design of Experiment is worth or not.

Each possible combination of the four optical parameters mimics a different tissue. This way we design a full factorial plane with three levels for each of the four factors. Through the in-house built Monte Carlo platform we simulate the application of the light treatment to all these tissues and we collect the resulting 81 rates of absorption. The device is set to constant settings with the same wavelength of 800 nm.

To understand the synergistic effect of the optical properties on the rate of absorption we plot the interaction effects (see Figure 3.6). Each sub-figure shows the combined effect of two factors:

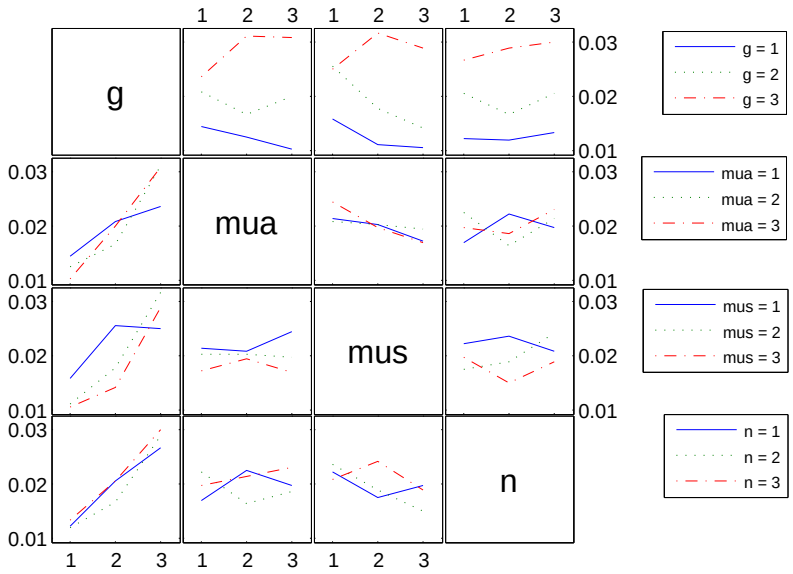


Figure 3.6: Interaction plot for a full factorial design with 4 factors at 3 levels.
The response is the rate of absorbed energy and the factors, coefficient of anisotropy $g$, coefficient of absorption $\mu_a$, coefficient of scattering $\mu_s$ and index of refraction $n$.

the absorption rate is treated as dependent variable evaluated with respect to one factor (the independent variable) while the other is a parameter, leading to the three lines in different colors on each graph. As the legend and the x-axis show, the three levels are named $1, 2, 3$ and correspond to low level ($-15\%$ average value), average level (the value from literature listed above) and high level ($+15\%$ average value) respectively.
All the parameters are significant and their variation of 15% induces a non negligible consequence on the rate of absorption in the tissue. The amount of gained energy in the simulated tissues varies of more than 30%. Moreover, we can not extrapolate a general trend looking at Figure 3.6: not only the slope is different between various lines, but also each line itself appears to change the gradient sharply.

## 3.4 Conclusion

The Monte Carlo method for light diffusion is introduced and the algorithm is implemented; it allows the simulation of different amounts of energy (by setting the number of photon packets). The optical properties of the tissue, i.e. coefficient of absorption, coefficient of scattering, index of refraction and coefficient of anisotropy, are wavelength-dependent. Thus, by tuning the wavelength it is possible to vary the rate of absorption and also, by setting the light profile, we can optimize the light delivery at the target depth. By using the Monte Carlo simulation platform, we study the dependence of the rate of absorbed energy on the optical properties of the tissue. We observe that a variation of $\pm 15\%$ in the tissue optical parameters leads to a spread of 30% in the absorbed energy in the hair follicle.
In literature these values are shown to vary beyond the $\pm 15\%$ range depending on the experimental conditions such as the type of tissue (post-mortem, ex-vivo, frozen) and the way the experiment is performed. This variation affects significantly the outcome of the process: the interaction plot in Figure 3.6 shows that the relation between the factors and the response has not a clear trend and a severe interaction is present between various parameters. In order to get consistent results it is therefore recommended to use a single set of data of the skin layer, as obtained from a single source. Moreover, a special attention must be paid when using the method for the derivation of the optical parameters given an absorption map, i.e. when considering the inverse problem. This can be done under the condition that three out of the four parameters are known. Otherwise one have to deal with an ill-posed problem that may have multiple physical solutions.

In the next Chapter, the rate of absorbed energy is used to estimate the temperature variations in the treated skin. This requires the study of the mechanism at the basis of interactions between light, heat and tissue.

# Chapter 4

# Thermal response of the light irradiated tissue

The goal of this chapter is the estimation of the temperature rise inside the skin-hair structure as a consequence of the photoepilation treatment. As a first step, we quantify the thermal power deriving from the light beam and subsequently we solve numerically the equations governing the heat diffusion inside the tissue. The temperature profiles in some areas of the skin-hair structure reach high peaks, and it is likely that a phase transformation is caused there. We investigate the literature and suggest a phase change model. The temperature variation induced by specific treatment settings is then used, together with other parameters, to predict the clinical efficacy.

## 4.1 Interaction mechanisms

In the previous Chapters we introduced the relevant information about the skin-hair anatomy and the properties of light. We also presented a Monte Carlo simulation to describe the propagation of light in complex media. Now we go deeper in some photobiology aspects, indicating the biological response of the human body when treated with light.
The necessary additional knowledge is broad and complex because light-induced effects are manifold and specific for each tissue. Moreover, the same effect which might be good for a certain goal can be disastrous for another one.
The diversity of interaction mechanisms is due to both specific tissue characteristics and treatment settings. Among the optical parameters of the skin, we consider the coefficients of reflection, absorption and scattering as discussed in the previous chapter. They determine the total transmission and the amount of absorbed energy at a certain wavelength. Since we want to estimate the temperature profile by solving the heat equations, we consider also thermal properties of the tissue such as heat conduction and heat capacity. From the light source, we get many other parameters, such as the wavelength, the exposure time, the energy, the focal spot size, the energy density and the power density (see Appendix A for definitions and units of measure). Often the energy density is called fluence or radiant exposure and the power density can be found as intensity or irradiance. For sake of clarity, we gather the listed variables in the flowchart of the process depicted in Figure 4.1. As we can see, the parameter space is extremely wide, but previous studies identify the power density and the exposure time as crucial factors in the outcome of the treatment.

As a very preliminary consideration, we observe that thermal effects become irreversible for temperature higher than 60°C for very short time scales (otherwise even lower temperatures are sufficient to get protein denaturation) and the extent and the severity of the thermal damage grows with the exposure time. In literature (see [7]) the effects of the light radiation on biological tissues are discriminated by the "1 $\mu$s rule": an irradiation time greater than 1 $\mu$s is coupled with measurable thermal effects while shorter exposure time usually causes negligible consequences. However, this is a general rule and is valid for single applications, while when the treatment is

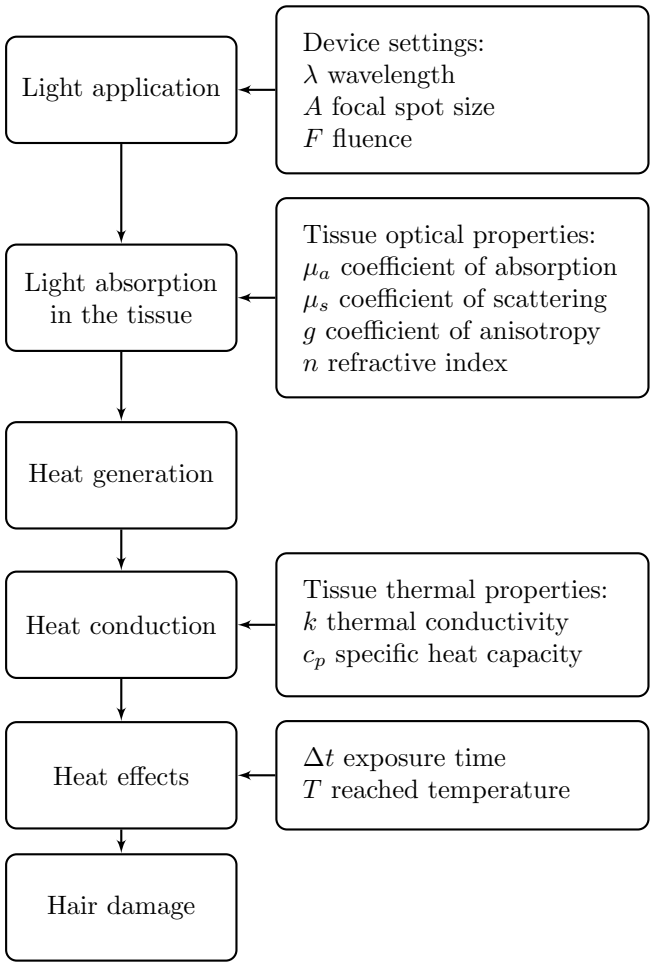


Figure 4.1: Relevant properties of the device and the tissue involved in light-tissue interactions.

repeated, a sort of cumulative effect must be taken into account.

The potential interaction effects between different high-power light emitting devices on various tissue targets were investigated since the invention of laser by Maiman in 1960. Nowadays, the classification under five main interaction types is commonly agreed upon (see [7]). These five basic mechanisms are shown in Figure 4.2; the horizontal axis represents the exposure time [s] while the vertical one is the power density [W/cm$^2$], both in the logarithmic scale. The circles give an estimate of the interaction mechanisms corresponding to a power density delivered for a certain exposure time. As we can see, all the possible interactions fall between the two dashed lines corresponding to a energy density of 1 J/cm$^2$ and 1000 J/cm$^2$, a relatively small range when compared with the extent of the vertical axis. Then, the effects are discriminated by the time of exposure:

1. Photochemical interactions $\tau > 1$ s;
2. Photothermal interactions 1 $\mu$s $< \tau <$ 1 s;
3. Photoablation 1 ns $< \tau <$ 1 $\mu$s;
4. Plasma-induced ablation $\tau <$ 1 ns;
5. Photodisruption $\tau <$ 1 ns.

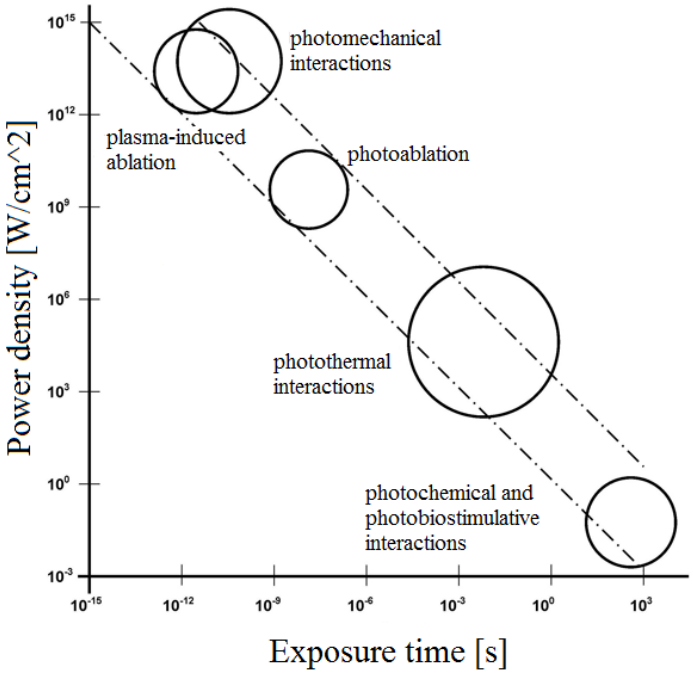


Figure 4.2: Schematic representation of laser-tissue interactions. Picture is taken from [7].

Each of these mechanisms gathers a wide range of cases and would require an extended presentation. Here we focus on the mechanism of photothermal interaction alone since it is the one taking place during photoepilation treatments.

### 4.1.1 Photothermal interactions

Thermal interactions correspond to a power density between 1 and $10^6$ W/cm$^2$ applied for a time varying between one $\mu$s and one second. The name gathers a very high number of cases, which have the increase of the local temperature as common main effect. Depending on the length of the time interval and the maximum temperature reached in the tissue, it is then possible to distinguish coagulation, vaporization, carbonization and melting.

Coagulation happens whenever the temperature rises above the threshold $T = 60$℃; the tissue becomes necrotic and darker than usual.

Vaporization can be seen as a thermomechanical effect since the damage is caused by the pressure build-up induced by the temperature increase. It occurs when a wavelength strongly absorbed by water is used. Then the peak temperature makes the water evaporate; evaporating, the water increases in volume and causes local explosions in the surrounding material.

When the temperature is higher than 100℃ , carbonization is observed: the tissue releases carbon, leading to a blackening in color. In medical light applications it is avoided since it reduces visibility and lower energies are sufficient to make the tissue become necrotic.

Finally, melting. Cracks originate from thermal stress induced by local temperature gradients. The temperature raises above $T = 100$℃ for a fraction of second and it cools down for repeated times.

Thus, the estimation of the temperature variation allows the understanding of the kind of interaction between the light and the skin-hair structure. In turn, this can be used to optimize the device settings to reduce side effects while getting high efficacy. We aim then to estimate the temperature increase during photoepilation. This is obtained by solving the governing equations

for the heat diffusion inside the skin, where the main biological processes are perturbed by the light-based treatment. First of all, the heat source must be derived from the absorption map computed in Chapter 3.

## 4.2 From light to heat

When a light beam is launched, a part of photons is absorbed by the molecules of the tissue, which are driven in an excited state. Collisions with other molecules lead to a gradual deactivation of the first ones and an increase in the kinetic energy of those they collide with. This increase in the kinetic energy of the molecules is, on a macro-scale, an increase in the temperature of the tissue. From a modeling point of view, this process makes a conversion needed from the light absorption (derived from the stochastic Monte Carlo model) to the equivalent heat source in the diffusion-convection-reaction equation. Note that using the stochastic approach, the treatment is considered out from any time reference, but if the real event is considered, it is natural to think that at least at the beginning the power rate will not be constant, but rather $I_0 = I_0(x,t)$ before reaching the steady state. What is often implied is the assumption of instantaneous photon transport. Roughly speaking, it means that the power is assumed to reach the optical steady state instantaneously when the light beam is launched, so that a separation of variables becomes possible:

$$I_0(x,y,z,t) = I_0(x,y,z)f(t) \quad [\mathrm{W/m^3}]. \tag{4.1}$$

Here $f(t)$ is a dimensionless function of time describing the shape of the pulse.
First, since the heat source must be expressed as a power rate $I_0$ and the device specifications give the delivered energy density (or fluence) $F$, we must derive the corresponding power $I_0$. The relation between power $I_0$ and energy $F$ $[\mathrm{J/m^2}]$ gives

$$F = \int_{-\infty}^{\infty} I_0 dt. \tag{4.2}$$

At the same time, the pulse shape can be considered as a signal and the related energy is given by

$$F_s = \int_{-\infty}^{\infty} |f(t)|^2 dt, \tag{4.3}$$

which must be converted into the physical meaning of energy through dividing by the magnitude $Z$ of the signal

$$F = \frac{F_s}{Z} = \frac{1}{Z}\int_{-\infty}^{\infty} |f(t)|^2 dt. \tag{4.4}$$

Comparing the two expressions for the fluence (4.2) and (4.4), we find

$$\int_{-\infty}^{\infty} I_0 dt = \frac{1}{Z}\int_{-\infty}^{\infty} |f(t)|^2 dt. \tag{4.5}$$

Since the magnitude of a signal is a measure of how far, in absolute value, the signal differs from zero, we can set $Z = \max(|f(t)|)$ and find

$$I_0 = \frac{1}{\max(|f(t)|)}|f(t)|^2. \tag{4.6}$$

Now, consider the launch of a light source with fluence $F$ or, equivalently, an initial optical intensity $I_0$ $[\mathrm{W/m^2}]$. The spot size of the source is $A$ $[\mathrm{m^2}]$. We statistically model this through the Monte Carlo method explained in the previous chapters, with a number of $N$ photon packets. Then the initial intensity per photon packet, the fraction of initial density (FII), is defined as

$$\mathrm{FII} = \frac{I_0 A}{N} \quad [\mathrm{W}]. \tag{4.7}$$

Keeping the convention of Monte Carlo model for which each photon packet is associated with a statistical weight $w \in [0,1]$, we have as output from the Monte Carlo model a map with the sum of weights absorbed in each voxel

$$w_{sum}(x,y,z) = \sum_{i=1}^{n} w_i(x,y,z), \tag{4.8}$$

where the term voxel refers to the elementary volumes in which the domain is discretized and the coordinates localize each of them in the space. $w_i(x,y,z)$ is the fraction of weight of the $i^{th}$ photon packet absorbed in the voxel with coordinates $(x,y,z)$.
Then, the absorbed power per photon is $w_i(x,y,z) \cdot \mathrm{FII}$ and summing up on the packets we can derive the volume fraction of absorbed intensity (FAI)

$$\mathrm{FAI}(x,y,z) = \frac{\mathrm{FII} \cdot w_{sum}(x,y,z)}{V(x,y,z)} \quad [\mathrm{W/m^3}], \tag{4.9}$$

where $V$ represents the volume of the considered voxel.
It is possible to rewrite the result in a $3D$ matrix containing the fraction of absorbed intensity in each voxel; this tensor will be referred to as absorption map. To write it, we need to fix a coordinate and let the other two vary

$$\begin{aligned}
\mathrm{AM}(x,y,z_0) &= \begin{pmatrix} \mathrm{FAI}(x_1,y_1,z_0) & \dots & \mathrm{FAI}(x_1,y_n,z_0) \\ \vdots & \dots & \vdots \\ \mathrm{FAI}(x_n,y_1,z_0) & \dots & \mathrm{FAI}(x_n,y_n,z_0) \end{pmatrix} \\
\mathrm{AM}(x,y_0,z) &= \begin{pmatrix} \mathrm{FAI}(x_1,y_0,z_1) & \dots & \mathrm{FAI}(x_1,y_0,z_n) \\ \vdots & \dots & \vdots \\ \mathrm{FAI}(x_n,y_0,z_1) & \dots & \mathrm{FAI}(x_n,y_0,z_n) \end{pmatrix} \\
\mathrm{AM}(x_0,y,z) &= \begin{pmatrix} \mathrm{FAI}(x_0,y_1,z_1) & \dots & \mathrm{FAI}(x_0,y_1,z_n) \\ \vdots & \dots & \vdots \\ \mathrm{FAI}(x_0,y_n,z_1) & \dots & \mathrm{FAI}(x_0,y_n,z_n) \end{pmatrix}
\end{aligned} \tag{4.10}$$

When the light spectrum is not pure but comes from a mix of wavelengths, then the contribution

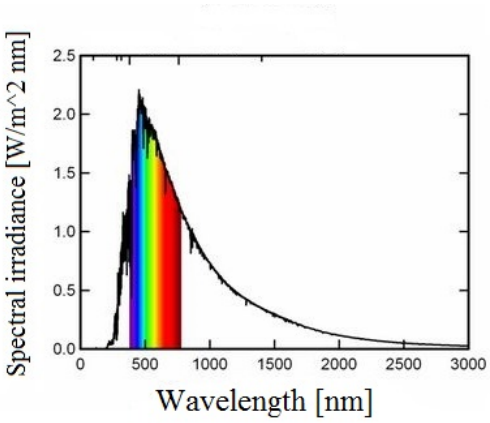


Figure 4.3: Spectrum of the irradiance as function of the wavelength.

of each wavelength is computed separately and then is summed up in order to get the combined

effect; note that the spectral irradiance varies in intensity as a function of the wavelength as shown in Figure 4.3, therefore the heat source $Q$ from laser application is given by the weighted sum:

$$\mathrm{Q} = \sum_i \mathrm{AM}_{\lambda_i}(x, y, z) \times S_{\lambda_i}. \tag{4.11}$$

## 4.3 The COMSOL model

In the previous Section we quantified the distribution of the heat source in the tissue as derived from the stochastic analysis. In this Section we list the necessary requirements to build a COMSOL simulation platform (see the manual [8]). This is then used to simulate how heat diffuses in the skin-hair structure after the light application.

### 4.3.1 The geometry

The model addresses a skin-hair reproduction where parameters such as hair thickness, depth and density are estimated and are part of the clinical input of the platform. The skin conformation introduced in Chapter 2 is schematically reproduced as shown in Figure 4.4a. It is a rather simplified geometry where the three layers, namely the epidermis, the dermis and the subcutis, are modeled as parallel slabs with thickness of 0.1, 1.2 and 0.9 mm respectively (see for instance [9, 10]). The additional upper layer is the ambient medium, usually air, included in the model geometry because it plays a fundamental role in the heat transfer, cooling the surface through convection and allowing evaporation.

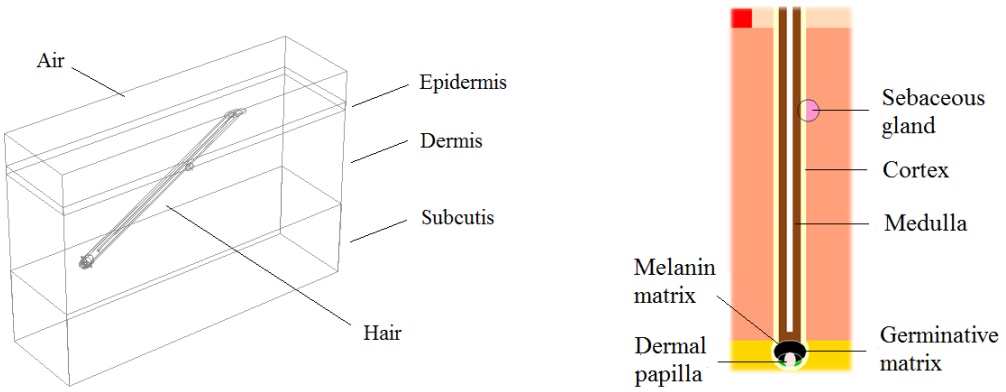


(a) Skin-hair structure.

(b) Hair reproduction.

Figure 4.4: The skin-hair structure, computational domain built in COMSOL.

The full geometrical hair model, composed of hair shaft and follicular compartments, is depicted in Figure 4.4b. We construct the hair shaft as a set of three coaxial cylinders, the medulla, the cortex and the outer root sheath with increasing radii. In addition, from histological analysis we identify the key follicular compartments, responsible for the hair growth (see [1, 2, 11, 12, 13]): the melanin-containing matrix, the non-absorbing germinative matrix and the dermal papilla. Those compartments are modeled using ellipsoid shapes. Finally, the little sphere beside the hair represents the sebaceous gland.

This skin-hair model allows the mimicking of various hair densities by replicating the single hair. This way it is possible to account for optical and geometrical shadowing.
The entire geometry is discretized through a tetrahedral mesh (see Figure 4.5). The element sizes of the mesh are chosen to fit the different structures: bigger ones such as the dermis and the fat layer have a coarse mesh whereas smaller structures, such as the hair follicle, have a fine mesh. The

heat source is mapped upon each grid point of the mesh through nearest neighbor interpolation of the source map.

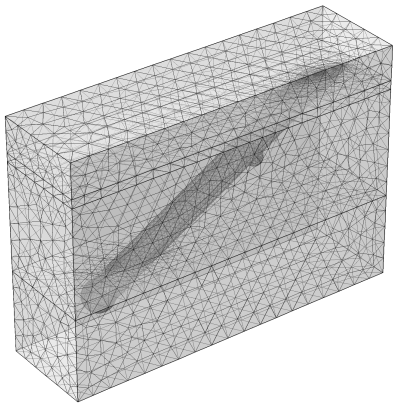

Figure 4.5: Mesh on the skin-hair structure. The element size varies according to the dimension of the considered part of the domain.

### 4.3.2 The governing equation and boundary conditions

We model the temperature response of the skin to laser irradiation by means of the heat conduction equation

$$\rho c_p \frac{\partial T}{\partial t} + \rho c_p u \cdot \nabla T = \nabla \cdot (k \nabla T) + Q, \tag{4.12}$$

where $T(x, y, z, t)$ [K] is the temperature in the skin-hair structure, $\rho$ [kg/m$^3$] is the tissue density, $c_p$ [J/kg K] is the heat capacity at constant pressure and $k$ [W/m K] is the thermal conductivity. The parameters $k$, $c_p$ and $\rho$ are specifically defined for each material and constant (both time and temperature independent). $Q(x, y, z, t)$ is the heat source derived from the rate of light absorption computed through Monte Carlo simulation (see 4.11).

The initial temperature is set to $T_0 = 37$℃ throughout the fat layer and decreases linearly in the dermis and epidermis till $T_0 = 33$℃ at the external surface. The cooling medium is placed on top of the epidermis (it can be water, sapphire or quartz) and is set to its real initial temperature. If no active cooling is required, the top of the epidermis is in contact with air that is maintained at the room temperature. Thus at the outer surface we set non homogeneous Neumann condition mimicking the convection/conduction depending on the chosen cooling medium. We choose for the simulation the case of free convection according to the Newton cooling law with $h$ [W/ m$^2$ K] the air heat transfer coefficient and $T_{ext}$ the temperature of the ambient medium

$$-n \cdot (-k \nabla T) = h(T_{ext} - T). \tag{4.13a}$$

The bottom of the fat layer is at a fixed temperature of $T_D = 37$℃ and is set through a Dirichlet boundary condition

$$T = T_D = 37\ ^\circ\text{C}. \tag{4.13b}$$

Finally, the lateral surface of the skin slab has a null outflow boundary condition to simulate the continuation of the domain; homogeneous Neumann condition are set

$$-n \cdot (-k \nabla T) = 0. \tag{4.13c}$$

### 4.3.3 Numerical simulation

A simulation is used to exhibit the thermal response predicted by the proposed model (4.12)-(4.13) with the heat source $Q$ given by (4.11). We consider a skin slab of dimensions $3.9 \times 1.1 \times 2.7$ mm; the hair has a radius of 50 $\mu$m with the follicle 1.2 mm deep inside the tissue. The hair shaft has a 30° inclination with respect to the skin surface. The photoepilation device delivers an energy density of 12 J/cm$^2$ for 20 milliseconds with the stepwise pulse shape as depicted in Figure 4.6. The governing equation (4.12) modeling heat transfer in solids with the boundary conditions

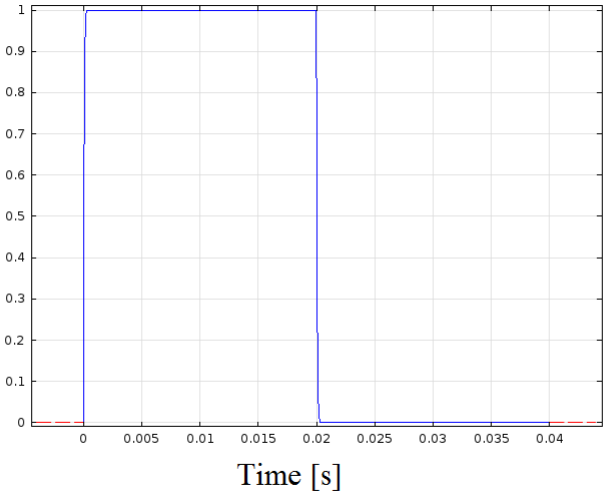


Figure 4.6: Temporal shape of the pulse. The device emits the light for 20 ms and then it switches off.

(4.13) are then numerically solved with COMSOL. We study the temperature variation in the different areas of the skin-hair structure. The average values in epidermis, dermis, in the hair and especially in the melanin blob and in the dermal papilla (two compartments of the hair follicle responsible for the hair growth) are plotted in Figure 4.7a.

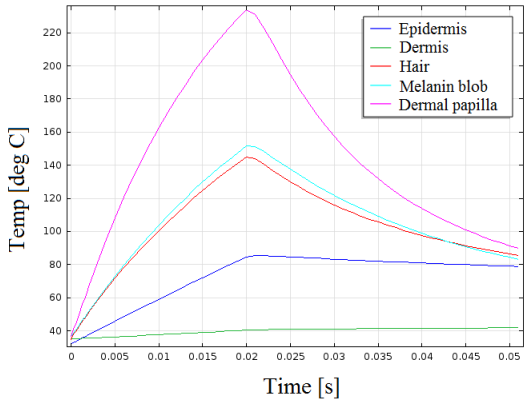


(a) Variation of the average temperature over time.

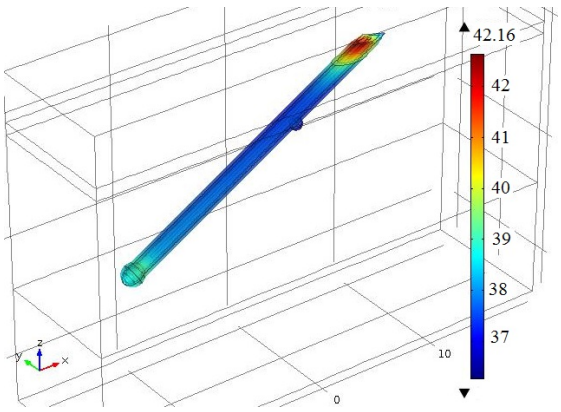


(b) Temperature distribution in the hair at time $t = 0.051$ s - after the light is switched off.

Figure 4.7: Temperature profile inside the skin-hair structure.

Again we have evidence that the treatment addresses the melanin: the most heated parts are the bulb compartments of the hair while the temperature increase in the epidermis is significantly smoother and the dermis remains almost untouched. The peak temperature is reached at the end of the energy delivery time: as we can see (Figure 4.6) at 0.02 seconds the light source is switched off, and from that moment the temperature stops rising and the cooling phase begins (see Figure 4.7).
Looking at the 3D temperature map focusing on the hair in Figure 4.7b, we can see that the highest temperature is reached at the hair top, where the light-emitting device is applied.

The model prediction of the temperature rise agrees with the qualitative expectations. However, the high peak values reached inside the skin-hair structure induce us to further investigate the phenomenon and look for some improvements.

## 4.4 An improvement to the model

Looking at the results of the simulation and at the ample literature available about medical applications of light, we aim to improve the model (4.12)-(4.13). First of all, we substitute the equation for heat diffusion in solids with the system of equations for the heat transfer in biological tissues. Further, we propose refined boundary conditions and we investigate whether a phase change may occur.

### 4.4.1 The bioheat equations

The bioheat equations were first introduced by Pennes in 1948 (see [14]) to understand the relationship between the temperature distribution and the biological response of the human body. Pennes analysis was addressing the case of the resting forearm, but after its introduction, the bioheat equation was widely applied to cases also far from their first application.

Thus, we upgrade the model (4.12) to the new governing equation

$$\rho c_p \frac{\partial T}{\partial t} = \nabla \cdot (k \nabla T) + \mathcal{P}(T) + Q_{bio} + Q, \tag{4.14}$$

where we keep the notations of the previous Section and $Q$ is defined by Equation (4.11). Two new terms are introduced: the heat transfer due to perfusion and the heat production due to metabolic processes $Q_{bio}$. The term perfusion refers to the process of nutritive delivery of arterial blood to a capillary bed in biological tissues and it is quantified by the expression

$$\mathcal{P}(T) = \omega_b \rho_b c_b (T - T_a). \tag{4.15}$$

Here $\omega_b$ is the blood perfusion rate (expressed as blood mass per unit mass tissue per second $[\mathrm{m}^3_{blood}/(\mathrm{sm}^3_{tissue})]$), $\rho_b$ is the density $[\mathrm{kg/m}^3]$ and $c_b$ the specific heat [J/(kg K)] of the blood. Finally, $T_a$ is the temperature of the arterial blood.

If we look at the Pennes equation (4.14), we see that when compared with the model for heat transfer in solids (4.12) it misses the convection term. Indeed, we assume that inside the skin it is not possible to detect a dominant flux in a given direction, but rather different velocities with diverging directions which on overall compensate each other. Thus the velocity $u$ in equation (4.12) results null.

### 4.4.2 Radiation at the external surface

For the boundary conditions at the external surface, we include now the thermal radiation. Radiation emitted by a body is a consequence of the thermal agitation of its composing molecules and takes place in form of emission of electromagnetic waves mainly in the infrared region. The radiation energy per unit time and unit surface area is proportional to the fourth power of the absolute temperature and is expressed by Stefan-Boltzmann law as

$$E(T) = \sigma(T^4_{amb} - T^4_{surf}). \tag{4.16}$$

Often in heat transfer simulations the radiation is neglected because the Stefan-Boltzmann coefficient $\sigma = 5.67 \cdot 10^{-8}$ [J/(sm$^2$K$^4$)] makes the contribution very small. However, during laser treatment high temperatures are reached as shown in the previous Section 4.3.3.

### 4.4.3 The phase change

In this Section, we aim to extend the model in order to approximate the phase change. The peak temperature reached inside the tissue and especially in the hair (see Figure 4.7) leads us to conjecture that phase changes may occur. Essentially, we are concerned with three: evaporation at the external surface, phase change of the water contained in the tissue and alteration of the hair structure.

**Evaporation at the external surface** We include now water loss from evaporation in the model boundary condition. The evaporation occurs when water molecules near the surface experience collisions that increase their energy above that needed to overcome the energy binding them to the surface. We are particularly interested in the energy loss associated with the phase change, coincident with the latent heat of water evaporation. The energy required to sustain the evaporation comes from the internal energy of the water which experiences a reduction in temperature. The evaporation of water is diffusion-limited and also highly dependent on both the relative humidity of the ambient medium and the temperature-dependent mass diffusion coefficients. We use this approach to estimate the rate of free-water surface vaporization loss. Essentially, it is based on the heat and mass transfer boundary layer analogy for evaporative cooling (see [15]),

$$Q_{evap} = h_{fg} h_m(T_s)(\rho_{v,e} - \rho_{v,sat})(T_s). \tag{4.17}$$

Here $Q_{evap}$ [W/m$^2$] is the vaporization loss term, $\rho_{v,e}$ [kg/m$^3$] is the density of water vapor in the air at the external temperature, $\rho_{v,sat}(T_s)$ [kg/m$^3$] is the mass density of saturated water vapor at the temperature of the tissue surface $T_s$, $h_{fg}$ [J/kg] is the phase change enthalpy of water and $h_m$ [m/s] is the convection mass transfer coefficient. The latter term is defined as

$$h_m = \frac{h_c}{\rho_a c_a L e^{2/3}},$$

where $h_c$ is the convection heat transfer coefficient, $h_c = Nu\ k_f/D$ for a quadratic flat surface, with $Nu$ Nusselt number, $k_f$ thermal conductivity of air and $D$ the characteristic length equal to the measure of one side of the considered domain.

**Phase change of the water contained in the tissue** The hair heats up by direct light absorption and conducts heat to the surrounding tissue. The skin consequently warms up. The effect tends to be weaker far from the hair, but still high temperatures are reached (see Figure 4.7a). We aim to include a phase change in the whole domain; we directly implement it in COMSOL, choosing the parameters of liquid water and water steam. The governing equations of the heat transfer inside biological tissue with phase change in COMSOL Multiphysics are here given by

$$\begin{cases} \dfrac{\partial}{\partial t}(\rho c_p T) + \rho c_p u \cdot \nabla T = \nabla \cdot (k \nabla T) + Q + Q_{bio} \\ k = \theta k_{ph_1} + (1-\theta) k_{ph_2} \\ c_p = \theta c_{p,ph_1} + (1-\theta) c_{p,ph_2} + L \dfrac{d\alpha}{dT} \\ \rho = \dfrac{\theta \rho_{ph_1} c_{p,ph_1} + (1-\theta) c_{p,ph_2} \rho_{ph_2}}{\theta c_{p,ph_1} + (1-\theta) c_{p,ph_2}} \end{cases} \tag{4.18}$$

Where $L = 2260$ [kJ/kg] is assumed to be the latent heat for the transformation of water into vapor, $T_{cr} = 100$℃ is the critical temperature and $\Delta T = 100$℃ is the transition interval between

| | Water (phase 1) | Steam (phase 2) |
|---|---|---|
| $k$[W/(m K)] | 0.58 | 1 |
| $\rho$[kg/(m$^3$)] | 995.6502 | 958.4 |
| $c_P$[J/(kg K)] | 4181.3 | 2080 |
| $\gamma$ | 1 | 1.3 |

Table 4.1: Properties of the two considered phases, liquid water and water steam, in the phase change.

the two phases. We still keep the hypothesis of velocity of convection $u = 0$. In Table 4.1 we list the values of the coefficients used in the simulation for liquid water and water steam.
with $\gamma$ the ratio of specific heats.

In addition, we implement another phase change model simply setting temperature-dependent parameters, density, heat capacity and heat conduction. Since the dermis is composed of water up to 80%, we inherit data obtained from the thermodynamics literature and interpolate them as follows:

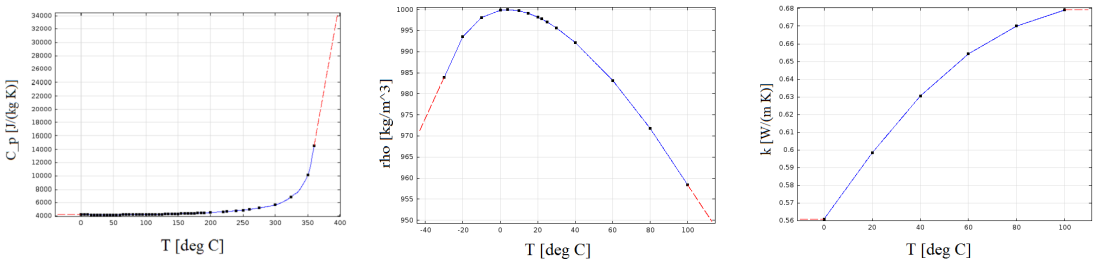


(a) Heat capacity $c_p$. (b) Density $\rho$. (c) Heat conductivity $k$.

Figure 4.8: Temperature dependence of the water properties.

**Alteration of the hair structure** Finally, the hair can reach a temperature greater than 100℃ and a modification happens, probably due to protein degradation. Thus we introduce a temperature-dependent heat capacity $c_p$ for the hair to simulate the melting. From literature, we know that it is a stepwise function of the temperature (see Figure 4.9):

$$c_p(T) = \begin{cases} 2789 & T < 220℃, T > 280℃ \\ 9539 & 220℃ < T < 280℃ \end{cases} \quad [\text{J/(kg K)}]. \tag{4.19}$$

$c_p$ is assumed to increase during the melting while it returns to its original values after the modification takes place. The area underlying the curve is the latent heat of the considered phase transition.

### Literature review on phase change transformations

The models proposed here for the phase changes occurring in the skin-hair structure are pretty simple. Time constraints did not allow to go deeper in more complex implementations, but the

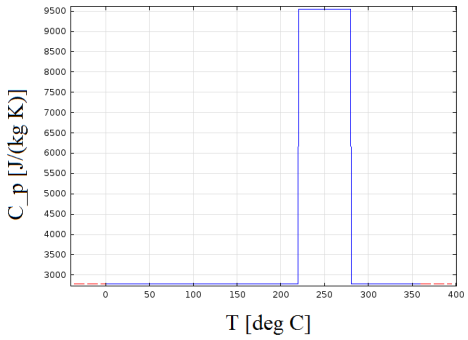


Figure 4.9: Temperature dependence of the specific heat capacity $c_p$ of the hair.

results obtained suggest that some improvements can still be achieved. We summarize here some references from literature for future investigations.

Jasinski [16] proposes a model based on the Pennes bioheat equation with perfusion rate coefficient and effective scattering coefficient dependent on the tissue damage, expressed by the Arrhenius damage integral. Other parameters, such as the metabolic heat source, are assumed to be constant.
Also Abraham and Sparrow [17] model the changes in tissue by the variations in blood perfusion rates depending on the local necrotic state of the tissue and the external pressure. Their model is based on the enthalpy method to account for liquid-to-vapor phase change with thermophysical properties dependent on the water content.
In thermodynamic, phase change is often modeled through the enthalpy method and this is observed to be an efficient method.
Sato and Niceno [18] propose instead an interface tracking method for the phase change: the mass transfer rate is directly calculated from the heat flux at the liquid-vapor interface. Finally, we cite a result not directly related to phase change but which could be worth in the understanding of the modifications caused by treatments: [19] couples the Pennes bioheat equation for heat transfer with the thermomechanical interactions in biological bodies at high temperatures, related to the damage of the tissue.

Many of the listed sources are related to studies on tissue coagulation or ablation. However, they could be driving insights in the tissue response to light treatment.

### 4.4.4 Numerical simulation for a phase change model

In this Section, we show the results from the numerical simulation of the improved model (4.14)-(4.13). Among the proposed modifications, we choose to implement the phase change and the hair denaturation through the temperature dependence of the parameters $\rho$, $k$ and $c_p$ of both the tissue and the hair. The heat flux due to perfusion and the heat production due to metabolic processes are proven to be negligible in studying laser treatment with exposure duration less than several seconds (see for instance [20, 21]).

We consider the same skin slab introduced in Section 4.3.3 and we study the application of the same treatment. The governing equations are those for the heat transfer in biological tissues (4.12); the phase change is simulated by using the dependence of parameters on the temperature and the heat capacity of the hair is defined as a step function of the temperature to model the melting (as explained in Section 4.4.3).

In Figure 4.10, we plot the variation over time of the average temperature in the melanin blob, dermal papilla, epidermis and dermis. The most heated compartments are again the dermal papilla (till 180 ℃) and secondarily the melanin blob (almost 130 ℃) since the treatment addresses the optically dark tissues. Thus the light is mostly absorbed in the hair. The curves look quite smooth even if we introduced a sharp discontinuity in the skin-hair structure properties.

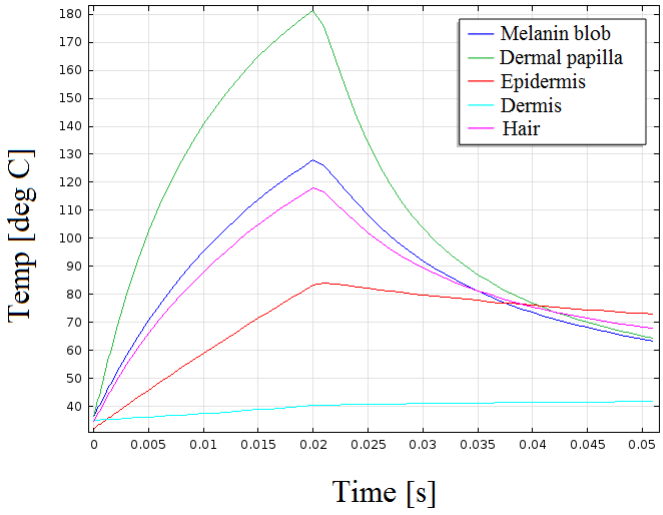


Figure 4.10: Average temperature behavior in different compartments of the skin-hair structure.

In Figure 4.11a we plot the profile of the maximum temperatures in the hair. Here we lose the regularity of the previous graph and we can see the sharp gradient expected when a phase change occurs: the heat deriving from the treatment makes the temperature inside the hair rise rapidly; after the temperature reaches its maximum value, due to some chemical modification, we observe a decrease. This is interpreted as the fusion of the hair. Then, the temperature flattens for a short time, in the re-solidification process and the tissue in the new configuration lately cools down to an equilibrium temperature.
By comparing (4.11a) and (4.11b) we can recognize the selectivity of the treatment again. Although our main focus is the estimation of the damage caused by the temperature increase, we should not overlook the side effects (e.g skin redness, hypo/hyper pigmentation, burning and pain) as it can be described by the temperature increase in the dermis and epidermis. In fact, the performance of the treatment is evaluated by both the achievement of the goal and the estimation of the unexpected effects.

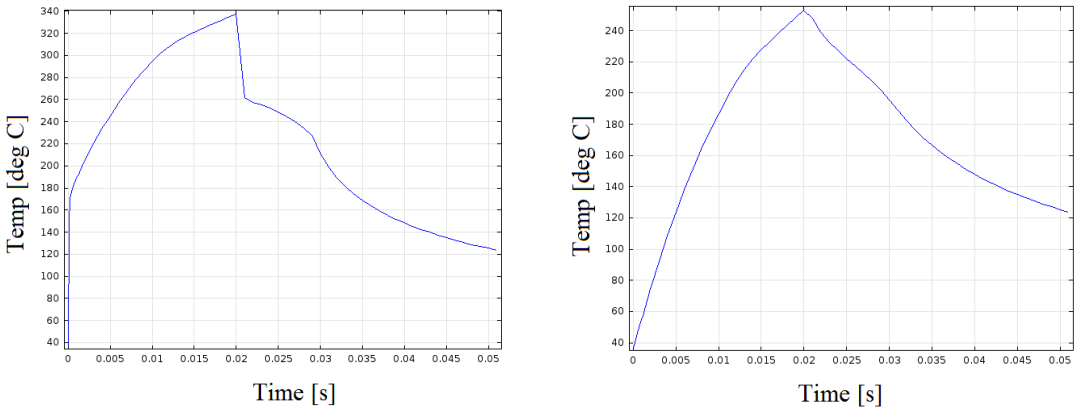


(a) Maximum temperature in the hair structure.

(b) Maximum temperature in the skin.

Figure 4.11: Maximum temperatures achieved in the skin-hair structure during photoepilation.

## 4.5 Conclusion

The main light-tissue interactions occurring in dermatological applications of light are presented. The absorbed optical energy is converted into the heat source for the equations of heat diffusion inside the skin. The numerical solution gives the temperature profiles in different areas of the skin-hair structure. We propose some possible approaches for phase changes and we suggest some further improvements following the literature results.

The maximum temperature is reached at the hair top, the optically dark area directly exposed to the light beam emitted by the device. Our guess is that here a phase change occurs and we propose the introduction of the evaporation and radiation terms in the boundary condition at the external surface. Actually, this observation is supported by the experimental evidence: in clinical trials the hair heating produces smoke and smell. This phenomenon is not recognizable inside the skin, at the bulb. Since our target is the bulb and not the hair top, we do not include evaporation and radiation in the simulation since it is not strictly relevant for the purpose of efficacy prediction but more for the estimation of side effects. However, the model can still be corrected and improved in the estimation in the temperature variation. To obtain a better forecast we recommend the inclusion of improved phase change models (for example some of the suggested literature) especially in the case treatments with higher energies are introduced at Philips.

# Chapter 5

# Predictive analysis for treatment efficacy

The severity of the damage, in terms of extension and permanency, depends on the time over which the temperature remains over a certain critical threshold (dependent on the exposure time) within the target tissue. For time scales of tenths of milliseconds, the protein (and thus the structure) denaturation is observable for values higher than 60℃, so that when the temperature rises above this thermal threshold, some irreversible effects can take place. Whether this happens and the severity of the consequences, is discriminated by the time the skin is exposed to the heat source. If we know the temperature profile $T(t)$, then we can estimate both the damage caused to cells and the probability of hair death.
The complexity of the analysis is due to the high number of variables from both the device settings and the clinical information. Moreover, repeated treatments can lead to non linear cumulative effects.
The understanding of the damage caused by the process can be useful in forecasting the treatment efficacy. A reliable model can drive the selection of the best device settings and can predict the efficacy range for given clinical cases. In this Chapter we first consider a method commonly used in biological predictions and then propose two new models. Both are tested against clinical data showing high correlation.

## 5.1 Design of the clinical study

The clinical study is summarized in Table 5.1: 133 volunteers took part to the photoepilation study. Each subject, invited for the intake session, received all the information about the study during the face-to-face intake, including advantages of light-based hair removal together with restrictions and potential risks. Subjects were informed about voluntary participation in the trial and the possibility of withdrawing at their own initiative with no adverse consequences. The original Informed Consent is stored in the subject file and each one did receive a copy. During the intake session volunteers had to complete a list with inclusion and exclusion criteria, including medical history, contraindicating medication etc. This was an integral part of the Informed Consent they were asked to sign. All the volunteers have a Fitzpatrick skin type II-III, a classification referring to the central Europe skin type with hair color varying from light brown to black.

The treatment focuses on two different areas (hereafter referred to as 1 and 2) which show systematic influence on the efficacy. Various available devices with pulse durations ranging from 6 to 40 ms and fluences between 6.5 and 10.4 J/cm$^2$ are used. Those devices are either laser based with 800 nm wavelength or intense pulsed light (IPL) devices with a broadband optical spectrum. At the start of the first treatment session, photographs are taken and evaluated for hair density, thickness and color; the number of present hairs before treatment $N_0$ is registered. At the follow-up session, typically two weeks after the end of the treatment, photographs are taken again and

| | |
|---|---|
| Nr. Volunteers | 133 |
| Fitzpatrick skin type | II-III |
| Hair color | light brown to black hair |
| Treated area | 1/2 |
| Pulse duration | 6-40 ms |
| Wavelength | [600-1300] nm |
| Fluence | 6.5-10.4 J/cm$^2$ |

Table 5.1: Clinical study overview.

the hair density is evaluated; the final number of hair is denoted as $N_f$. The treatment efficacy $Ef$ is then estimated by the complementary of the ratio between the number of residual hair over the number of hair before the treatment:

$$Ef = 1 - \frac{N_f}{N_0}. \tag{5.1}$$

Clinical inputs from each trial are used in the optothermal model. For simplicity, geometrical parameters such as hair depth, hair thickness and various skin layers thickness's remain constant for all the simulated cases. Also the optical parameters are fixed, reflecting a fair skin type with brown hair. Each clinical case is simulated with the use of the optothermal platform and the numerical solution shown in Chapter 4 gives the temperature variations in different compartments of the skin-hair structure.
Then, physical values are derived and used for efficacy prediction.

## 5.2 Arrhenius damage integral

In the literature of medical treatments with light (see for instance [3]), we notice a significant consensus in using the Arrhenius damage integral.
It is derived from the Arrhenius equation estimating the velocity of endothermic chemical reactions

$$\frac{dn}{dt} = -A \exp\left\{-\frac{\Delta E}{RT(t)} n\right\}, \tag{5.2}$$

where $n$ is the number of entities (molecules, living cells,...) that are not damaged yet, $R$ is the universal gas constant $\left(8.315 \frac{\text{J}}{\text{mol·K}}\right)$ and $T(t)$ is the temperature profile in the germinative matrix expressed in Kelvin. The two parameters are the molecular frequency factor $A$ [1/s] and the activation energy $\Delta E$ [J/mol], a threshold which must be reached in cells to have denaturation. Both $A$ and $\Delta E$ are function of the considered tissue. From (5.2), the ratio between undamaged entities at time $t$ and at time $t = 0$ is quantified by

$$\frac{n(t)}{n(0)} = \exp\{-\Omega(t)\}, \tag{5.3}$$

where

$$\Omega(t) = A \int_0^t \exp\left\{-\frac{\Delta E}{RT(s)}\right\} ds. \tag{5.4}$$

As the whole process describes a physical process rather than a chemical one, we rewrite equation (5.4) as

$$\Omega(t) = \int_0^t \exp\left\{\Lambda\left(1 - \frac{T_c}{T(s)}\right)\right\} ds. \tag{5.5}$$

Here the new constants

$$\Lambda = \ln(A) \quad \text{and} \quad T_c = \frac{\Delta E}{R\Lambda} \tag{5.6}$$

represent an amplification factor [1/s] and the critical thermal threshold [K] respectively. Note that the order of magnitude for $A$ and $\Delta E$ is $10^{200}$ and $10^6$ respectively, while the derived parameters $\Lambda$ and $T_c$ are much smaller. Thus the conversion is favourable in computational terms as well. We determine the values of $\Lambda$ and $T_c$ through optimization since they are poorly defined in literature and not known for the hair compartments. In particular, we maximize the correlation coefficient between the values of the damage integral and the measured clinical efficacy. The algorithm is based on the *fminsearch* MatLab function finding the maximum of an unconstrained scalar function of several variables, starting at an initial estimate. Multiple initial guesses chosen in a set of admissible values are used to detect and overcome the eventuality of multiple local maxima.

In Figure 5.1 we show the result of the predictive analysis with the Arrhenius damage integral. The horizontal axis represents the Arrhenius damage integral while the vertical one is the meas-

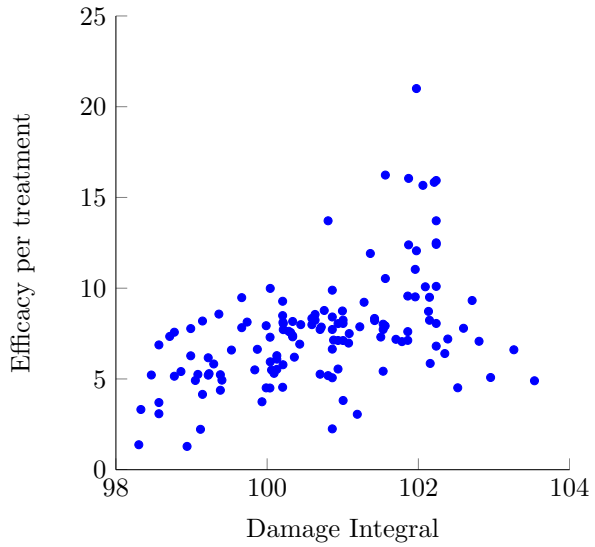


Figure 5.1: Efficacy prediction with the Arrhenius damage integral.

ured efficacy per treatment, directly obtained by dividing the highest efficacy by the number of treatments. This manipulation is needed because each clinical case was treated a different number of times, between 3 and 18, depending on the reached achievements. However, we suggest to improve the definition of the efficacy per treatment accounting for the cumulative effect of subsequent sessions. Each blue dot is one clinical trial and its position is determined by the computed and measured values. The shape of the dots distribution is a measure of the model optimality.
As we can see, the predictive power of this method applied to the available set of clinical data is very low. The maximum correlation is 47.91% obtained with optimized parameters ($\Lambda = 7.99$ and $T_c = 134.956$). In parallel, we investigate the correlation between the integral of the temperature profile over time and the measured efficacy (see Figure 5.2). The vertical axis represents the efficacy per treatment, this time plotted against the values of the integral of the temperature profile over time. Then, the values of each case of the clinical data set are computed and plotted. The distribution of the blue dots does not show a strong trend again. Further, from the comparison between Figure 5.1 and Figure 5.2, we infer that the damage integral does not bring any additional information to the simple integral of the temperature profile in our case.

Our guess is that the failure in the prediction with the Arrhenius damage integral is due to the lack of precision in simulations: we set average values for hair depth, radius, angle and also for the optical properties. Thus we homogenize many parameters losing sources of variability.

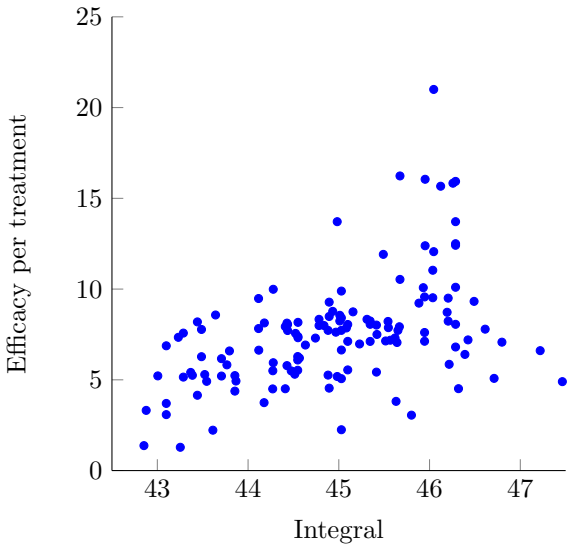


Figure 5.2: Efficacy prediction with the integral of the temperature profile over time.

At this point, we face the choice between the exact simulation for each of the 133 clinical trials and the use of a different method allowing the reintroduction of the neglected variability. However, the new simulations would require additional clinical data. For the sake of simplicity and time-costs saving, we decide to use the available set of values and apply statistical methods. In the following sections we propose two statistical methods, the multiple linear regression and an artificial neural network which allow the inclusion of degrees of freedom.

## 5.3 Multiple linear regression

First, we consider the multiple linear regression. In this model a response variable $y$ is related to a set of predictors $x_i$, with $i = 1, \dots, n$. In particular, we include the first order interactions between factors and the terms up to the second power:

$$y = b_0 + \sum_{i=1}^{n} b_i x_i + \sum_{i=1}^{n} \sum_{j=i}^{n} b_{ij} x_i x_j + \varepsilon. \tag{5.7}$$

Here $\varepsilon$ is the disturbance term, an unobserved random variable that adds noise to the multilinear relationship between the dependent variable and the regressors. It captures that influence on $y$ which is not explained by the predictors. When it is necessary to account for $\varepsilon$ as a random variable, some assumptions on it are needed, and those are usually independence and Gaussian distribution. In our case the independence is not trivial since there might be some additional structure in the data set which makes the trials not totally independent. This is the case, for example, of multiple treatments on the same subject. However, the requirements mentioned above are not needed when the model (5.7) is used for predictions, as $\varepsilon$ is a quantity which will be minimized. Here we are concerned with the distribution of the disturbance terms only: we expect them to be random values.

The coefficients $b_i$ are tuned to fit the data; the criterion is the minimization of the error $\varepsilon$ between the model outcome and the target value, i.e. the measured efficacy.
The clinical set of data introduced in Section 5.1 contains both treatment settings and clinical information: fluence rate, pulse duration, number of treatments, hair density, efficacy reached after each session and the maximum observed, treatment location, personal identifier and hair color. Beside those, we compute the Arrhenius damage integral derived in the previous Section to

be included among the predictors.
The qualitative variables are converted into reference numbers: the hair color variation observed in the clinical study is classified in three categories, namely black, brown and mixed - all those cases which can not be included in the previous classes. A number for each color group is then defined through the conversion from the RGB to the gray scale (see Table 5.2). In addition, the

| | |
|---|---|
| black | 0.1 |
| brown | 0.3 |
| mixed | 0.5 |

Table 5.2: Color conversion.

treatment location is distinguished by a binomial variable; we arbitrarily choose 1 and 2 as they showed the best results among the probed values.

Through a stepwise algorithm in MatLab, we check all the considered variables (both predictors, second power and interactions). This method excludes the factors with a p-value higher than a chosen threshold and thus also those presenting collinearities. In the end, we remain with the density, the number of treatments, the location, the color and the Arrhenius damage integral in the logarithmic scale. Among the second order terms, they remain the square of the density and the square of the number of treatments. Finally, the non-negligible interactions are density-number of treatments and color-location. The resulting equation for the multi linear regression is then

$$\begin{aligned}\frac{\mathrm{Ef}}{\mathrm{N.Tr}} = b_0 + b_1 \log_{10}(\mathrm{DI}) + b_2 \cdot \mathrm{den} + b_3 \cdot \mathrm{den}^2 + b_4 \cdot \mathrm{N.Tr} + b_4 \cdot \mathrm{N.Tr}^2 + \\ + b_5 \cdot \mathrm{loc} + b_6 \cdot \mathrm{col} + b_7 \cdot \mathrm{N.Tr} \cdot \mathrm{den} + b_8 \cdot \mathrm{loc} \cdot \mathrm{col},\end{aligned} \tag{5.8}$$

where $\frac{\mathrm{Ef}}{\mathrm{N.Tr}}$ is the predicted efficacy per treatment to be compared with the clinical one.
In the following, we show the results of the prediction through the built regression model (5.8). The clinical set of data is randomly divided into two subsets for the training and the testing of the model respectively.

### 5.3.1 Training of the model

This Section deals with the *training of the model*, i.e. the adaptation of equation (5.8) to our data estimating the weights $b_i$. We use a random sample consisting of 70% of the total amount of the available data and the MatLab function *regress* . It returns the best obtainable estimate for the coefficients $b_i$ and the error $\varepsilon$ committed in estimating the efficacy per treatment. This is defined as the difference between the outcome and the target, and is minimized through least-square method.

Figure 5.3 shows the result of the training. The horizontal axis represents the measured efficacy; then, different quantities are plotted in different colors according to the legend. The green line is the ideal prediction, in the case the outcome of the model equals the measured efficacy. The predicted values are shown as blue dots. Finally, the red lines delimit a 95% prediction interval. It means that future predictions will fall in this region with a 95% probability.

As we can see, the model prediction is accurate, the blue dots are close enough to the green line. The correlation between the computed and expected values is up to 0.9 and the squared coefficient of multiple correlation $R^2$ of the model is about 80%. In other words, the 80% of the variability is explained by the predictors.

### 5.3.2 Testing of the model

The remaining 30% of data is used to test the model. We want to see how good is the prediction when clinical cases not considered in the training are studied with the model (5.8). We plug the

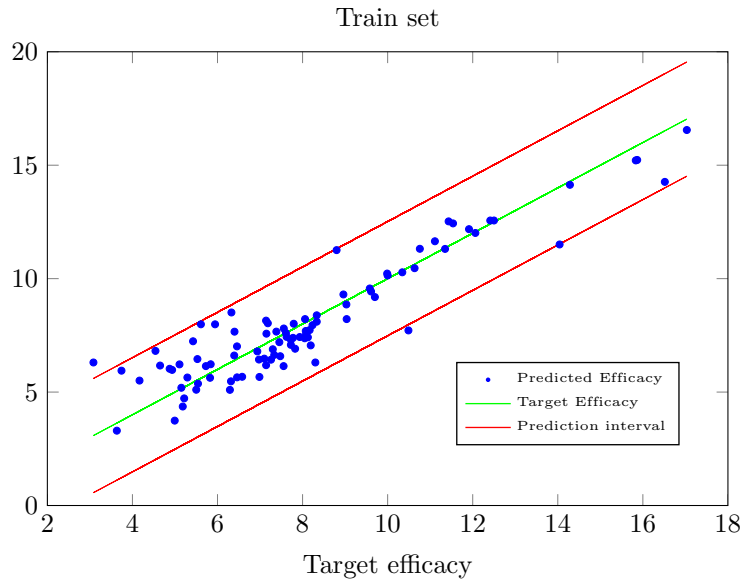


Figure 5.3: Efficacy prediction with multiple linear regression.

values of predictors and the coefficients derived from the training in the model equation, and we get the estimated efficacy per treatment for each trial. The testing is conducted to check whether we incurred in overfitting, i.e. the model is accurate on the training set but it has no generalization power.

In Figure 5.4 we show again the predicted values as blue dots, the target efficacy as a green line

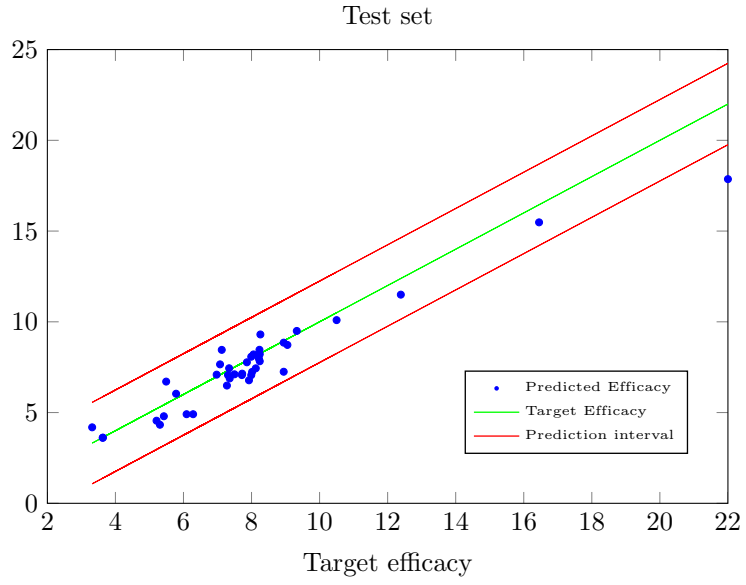


Figure 5.4: Efficacy prediction with multiple linear regression.

and the red ones as the prediction bounds. The model passes the test: when the analysis is made on new data, the predictive power is good and there is no evidence of overfitting. The blue dots are close enough to the green line with a correlation coefficient of 93% between the predicted and the measured efficacy per treatment.

### 5.3.3 Model interpretation

In this Section we analyze the regression model (5.8). Looking at the coefficients obtained (see Table 5.3), we can see that the bigger positive contribution is given by the Arrhenius damage integral - an expected result according to the literature. The density is associated with a negative coefficient. A higher density negatively affects the efficacy because of a shadowing effect that reduces the amount of light absorbed by each hair. Also the number of treatments has a negative coefficient because we are considering the efficacy per treatment as modeled response, and not the total one. Color and location are strongly related; when we consider one among the two distinguished areas, the efficacy decreases with the increase of the number chosen for the color. In fact, the lower number is associated with the optically darker hair, which consequently implies higher absorption and thus more efficient treatments. However, this relationship is not fully recognizable when we consider the cases concerning the treatment of the other location. Finally, since the second order coefficients (the square of the density and of the number of treatments) are very small, we interpret them as correction terms.

| Predictor | Coefficient |
|---|---|
| Damage integral | 0.2734 |
| Density | $-0.1157$ |
| Density$^2$ | $-0.0021$ |
| N. Treatments | $-2.4408$ |
| N. Treatments$^2$ | 0.0415 |
| Density * N. Treatments | 0.0198 |
| Location | -0.1363 |
| Color | $-0.2411$ |
| Location * Color | -2.2757 |

Table 5.3: Predictors and corresponding coefficients.

### 5.3.4 Model robustness

We design a robustness test with respect to the random sampling, 10000 times. Each time we build a model with different coefficients, due to the different random partition of the data set into the training and testing sets. For each model, we record the squared coefficient of variation $R^2$ and the coefficient of correlation between predicted and measured values (in both the training and testing sets).

The vector of the values of $R^2$ has a standard deviation of $\sigma = 0.0225$ and a corresponding coefficient of variation of

$$c_v = \frac{\sigma}{\mu} = \frac{0.0225}{0.8853} = 0.0254. \tag{5.9}$$

This value is a normalized measure of dispersion and gives a clear idea of the absolute variation from the mean value. The coefficient of variation in our case is very small and this is shown by the histogram in Figure 5.5a as well. It represents the occurrence of the $R^2$; the value is pretty stable around the mean value $\mu = 0.8853$.

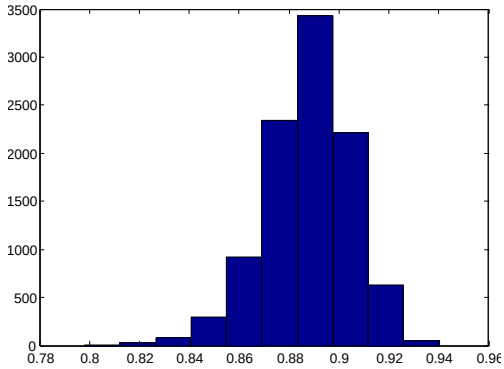


(a) Histogram for the values of $R^2$.

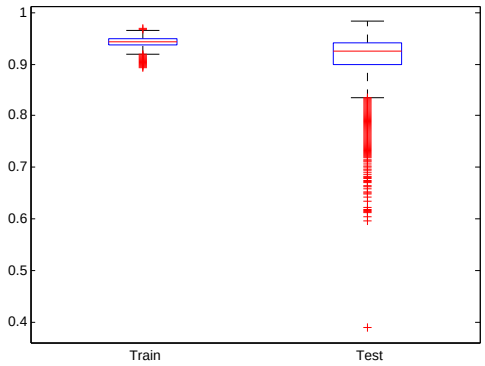


(b) Boxplots of the coefficients of correlation between predicted and measured efficacy in both testing and training.

Figure 5.5: Tests on the robustness of the model. The values are taken from 10000 models built on random sampling of data.

To understand the variation of the coefficients of correlation between predicted and measured efficacy, we plot two boxplots for the values in testing and training (see Figure 5.5b). We can see that also the correlation is stable: in training it is always above 90% with minimal deviation from the mean value, while in testing the variance is slightly higher, but still in a good range of values. If we do not consider the outliers, the correlation is higher than 80%. This with the previous results lets us conclude that the model is robust.

### 5.3.5 Prediction of the efficacy for some clinical trials with the regression model

As several tests in the Section 5.3.4 show, the method is robust. Here we explicitly show the achievements of the model (5.8) in prediction. We randomly select three cases with low, medium and high density from the clinical set of data. Some among the relevant values of treatment settings and clinical information are listed in Table 5.4. We obtain the expression for the efficacy

| Density | Fluence | FWHM | N. Tr. | Location | Color | Measured Eff. |
|---|---|---|---|---|---|---|
| 20 | 12.4 | 10 | 12 | 2 | brown | 98.2% |
| 40 | 11.172 | 15 | 12 | 1 | brown | 100% |
| 65 | 9.975 | 6 | 12 | 2 | brown | 75.8% |

Table 5.4: Device settings and clinical information of some treatments with low, medium and high density.

from Equation (5.8) just multiplying both sides by the number of treatments. Then we compare the computed values with the measured ones. In Figure 5.6 we plot the efficacy as a function of the number of treatments. As shown in the table, the case with lowest density achieved a clinical efficacy of 98.2% and a very close value is predicted by the model (98.06%). For the second clinical trial we predict an efficacy of 95.53% against the real one of 100% and finally, 72.01% against the measured 75.8% for the highest density case. In clinical studies this prediction is absolutely good, the committed error is smaller than 5% and corresponds to a relative error of about 8% in the worse cases.

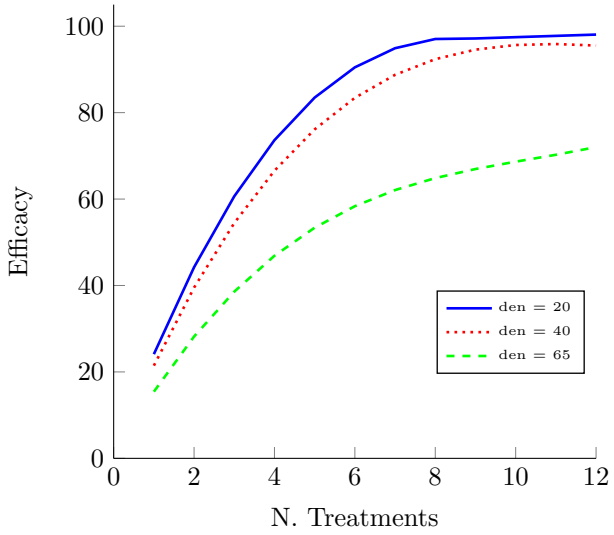


(a) Predicted efficacy at different number of treatments.

| Density | Measured Eff. | Predicted Eff. |
|---|---|---|
| 20 | 98.2% | 98.06% |
| 40 | 100% | 95.53% |
| 65 | 75.8% | 72.01% |

(b) Predicted and measured efficacy for the considered cases.

Figure 5.6: Prediction of the efficacy for some clinical cases.

The previous achievements of the model show it can be used in predictions. In other words, given the clinical information and the device settings, we can guess what to expect from the treatment. From a clinical point of view, this allows the definition of the optimal number of treatments to obtain the highest efficacy possible avoiding non needed sessions.
We consider a trial from the clinical data set which stopped early because of reasons other than the reached goal. As we can see in Table 5.5, the efficacy measured at the third and last treatment is estimated with good accuracy by the model.

| Density | N. Tr | Fluence | Meas. Ef. | Pred. Eff. |
|---|---|---|---|---|
| 35 | 3 | 11.837 | 51.1% | 50.03% |

Table 5.5: Predicted and measured efficacy for the considered case.

We investigate now what further sessions of photoepilation would lead to. In Figure 5.7 we plot again the efficacy as a function of the number of treatments, but rather than stopping at the used number of treatments, we consider the achievements of further sessions as a dashed line. We observe that in this clinical case an efficacy higher than 80% could be reached keeping treating.

Note that the regression models can be used for interpolation, but are not advisable for extrapolation. This means that it is possible to study the efficacy of clinical trials only if the values of the device settings and of the clinical information are in the range of the data used in the training of the model. In fact, the coefficients are tuned within that set of data and feeding the model with values beyond the given ranges can lead to unexpected results. Furthermore, the prediction interval (the red lines in Figure 5.3 and Figure 5.4) tends to be larger at the extremes of the interval, where the accuracy in prediction decreases. Thus, we strongly advise to carefully observe the ranges of the data used in the training since the use of the regression equation to predict values outside this interval is often inappropriate and can lead to wrong results.

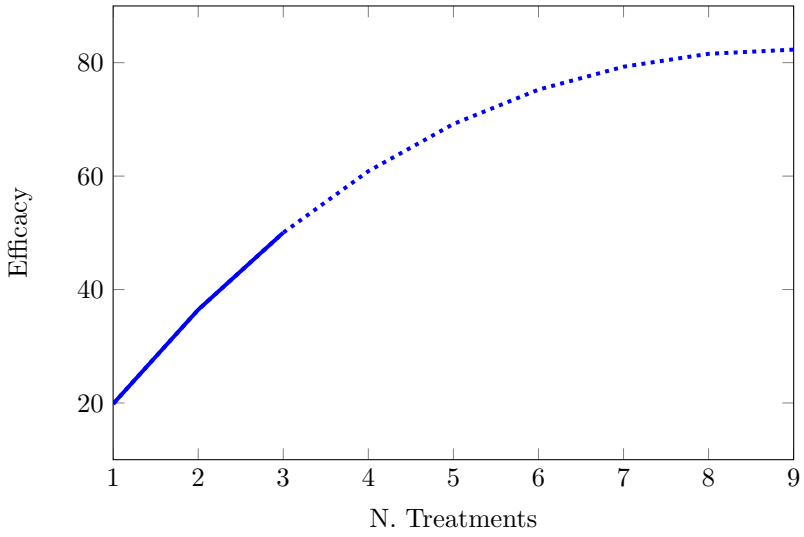


Figure 5.7: Hypothetical efficacy reached through a higher number of treatments.

## 5.4 Artificial neural networks

In parallel to the multilinear regression, we develop an artificial neural network to fit our data. The neural networks are part of the supervised learning, algorithms which use a known data set to make predictions. The available data are used both to build a model (training subset) and to check its strength (validation subset) just as in the multiple linear regression shown in Section 5.3. As expected, bigger datasets yield to models with higher predictive power that can generalize well for new datasets. Being functions designed to estimate relationships among data, their fitting power depends on the number of tunable parameters. The neural network receives some variables as input ($\underline{x}$), tunes the weights ($\underline{w}$) in the global summation and then transforms the result through a function $\varphi$ to get as closer as possible to the expected output. The schematic representation of the algorithm at the basis of neural networks is shown in Figure 5.8.

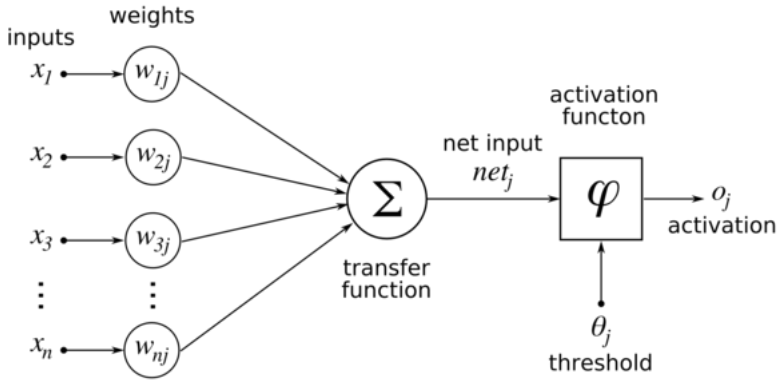


Figure 5.8: Schematic representation of the algorithm for artificial neural networks.

Mathematically, this can be translated as

$$o_j = \varphi(z_j) = \varphi\Big(w_{i0} + \sum_{k=1}^{n} w_{jk} x_k\Big) \tag{5.10}$$

Building a neural network involves a design issue about the number of hidden units: too many neurons in the internal layers cause poor generalization, while too few neurons make the accuracy of the network low. On the other hand, also the choice of the activation function $\varphi$ is involved in the network design [22]. Some among the possibilities are

- Heaviside (step) function
$$o_j = \begin{cases} 0, & z_j < \theta_j \\ 1, & z_j \geq \theta_j \end{cases} \tag{5.11}$$
- Sigmoid function
$$o_j = \frac{1}{1 + exp(-z_j)} \tag{5.12}$$
- Generalized logistic function
$$o_j = \frac{\exp(z_j)}{\sum_{i=1}^{n} \exp(z_i)} \tag{5.13}$$
- Hyperbolic tangent
$$o_j = \frac{\exp(z_j) - \exp(-z_j)}{\exp(z_j) + \exp(-z_j)} \tag{5.14}$$

The iterative algorithm for defining the weights which best fits the objective data is called training of the network; the most common used criterion is the least-squares method which consists in minimizing the objective function

$$E = \frac{1}{2} \sum_{j=1}^{n} \|o(x_j) - t(x_j)\|^2, \tag{5.15}$$

where $\underline{t}$ is the vector of the target values. Note that this method is pretty understandable but it is based on the strong assumption of Gaussian distributed targets with null mean.

**Lemma 5.4.1.** *The output of the network is the conditional average of the target data.*

$$o(x) = \mathcal{E}(t(x)|x)$$

*Proof.* From a statistical point of view, when the number of training data $n \longrightarrow \infty$, the least-squares training criterion (5.15) can be interpreted as

$$\begin{aligned} E &= \frac{1}{2} \int \int (o(x) - t(x))^2 p(t(x), x) dt dx \\ &= \frac{1}{2} \int \left\{ \int (o(x) - t(x))^2 p(t(x)|x) dt \right\} p(x) dx. \end{aligned} \tag{5.16}$$

The term in the curly brackets is

$$\begin{aligned} \int (o(x) - t(x))^2 p(t(x)|x) dt &= \int (o(x) - \mathcal{E}(t(x)|x) + \mathcal{E}(t(x)|x) - t(x))^2 p(t(x)|x) dt = \\ &= \int \Big( (o(x) - \mathcal{E}(t(x)|x))^2 + (\mathcal{E}(t(x)|x) - t(x))^2 + \\ &+ 2(o(x) - \mathcal{E}(t(x)|x))(\mathcal{E}(t(x)|x) - t(x)) \Big) p(t(x)|x) dt \end{aligned}$$

where the conditioned mean value is given by

$$\mathcal{E}(t(x)|x) = \int t(x) p(t(x)|x) dt(x). \tag{5.17}$$

Plugging this in the expression for $E$ given in (5.16) yields

$$E = \frac{1}{2}\int\int \Big((o(x) - \mathcal{E}(t(x)|x))^2 + (\mathcal{E}(t(x)|x) - t(x))^2 + \\ + 2(o(x) - \mathcal{E}(t(x)|x))(\mathcal{E}(t(x)|x) - t(x))\Big)p(t(x)|x)dt\ p(x)dx.$$

We can then rewrite the cost function as

$$E = \frac{1}{2}\int (o(x) - \mathcal{E}(t(x)|x))^2 p(x)dx + \frac{1}{2}\int (\mathcal{E}(t(x)^2|x) - \mathcal{E}(t(x)|x))^2)p(x)dx. \tag{5.18}$$

Since the second term is not dependent on the weights, it is not affected by the optimization scheme. Furthermore, the first term is nonnegative and thus is minimized when it equates zero. Thus, the result follows:

$$o(x) = \mathcal{E}(t(x)|x). \tag{5.19}$$

□

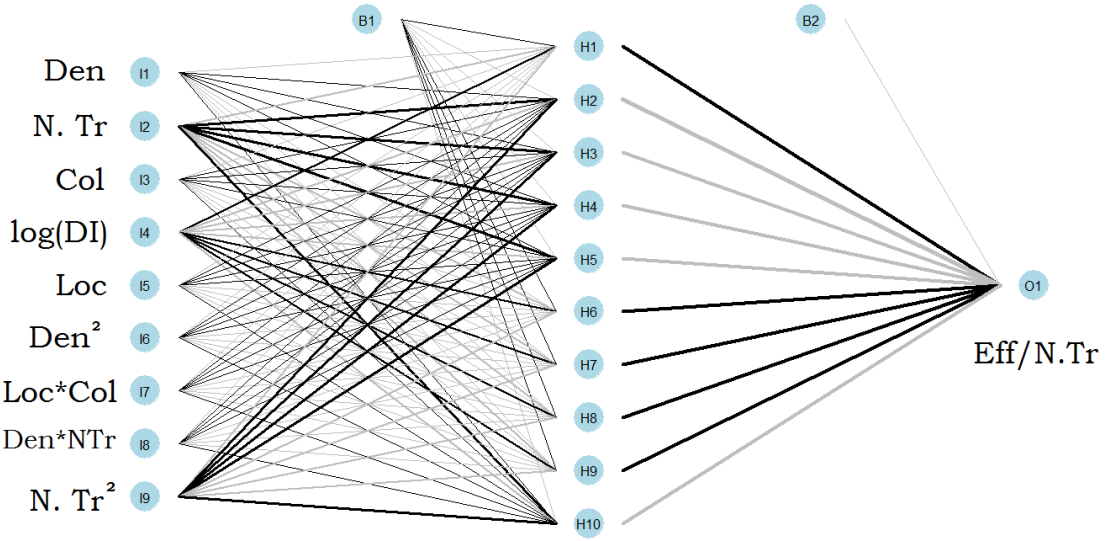


Figure 5.9: An artificial neural network built to fit the set of clinical data.

In Figure 5.9 we show an artificial neural network built on our set of data. We choose a single hidden layer with 10 neurons but the complexity of the network can be arbitrarily increased by adding layers and neurons in the existing hidden layers. We select the same predictors we use in the multilinear regression to be able to compare the two models. We show the prediction power of our neural network in both training (see Figure 5.10) and testing (see Figure 5.10b): the horizontal axis represents the measured efficacy while the vertical axis shows the predicted values. As in the multilinear regression, the dots fall close enough to the bisector with a correlation between predicted and measured values higher than 80% in both training and testing phases.

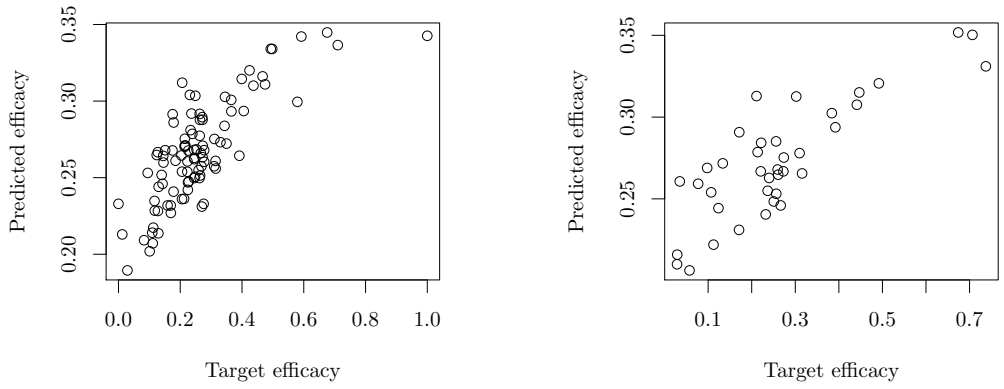


(a) Train set.

(b) Test set.

Figure 5.10: Efficacy prediction with artificial neural network. Training and testing sets.

The number of weights is so high that it would be meaningless to explicit all them. However, there exist efficient methods to interpret the outcome of the model. One of them is the graph in Figure 5.9. It is called Neural Interpretation Diagram (NID) and provides an insight into variable importance by visually examining the weights between the layers. The color is representative of the sign of the weight while the thickness is proportional to its absolute value. Those input variables that have strong positive associations with the response variable have many thick black connections between layers.

In Figure 5.11 we show a different way of interpreting the neural network. The weights of all the arrows connecting one input with the output through the network are summed (note that the weights can be either positive or negative). As a result, we obtain an overall coefficient estimating the influence of each predictor on the response. Here, we select those with bigger absolute value for sake of clarity. We can see that the result is the same we obtained in the analysis of the multiple linear regression model in Section 5.3.3. The Arrhenius damage integral is the stronger positive predictor while the hair density, the number of treatments and the hair color contribute negatively when their value increases.

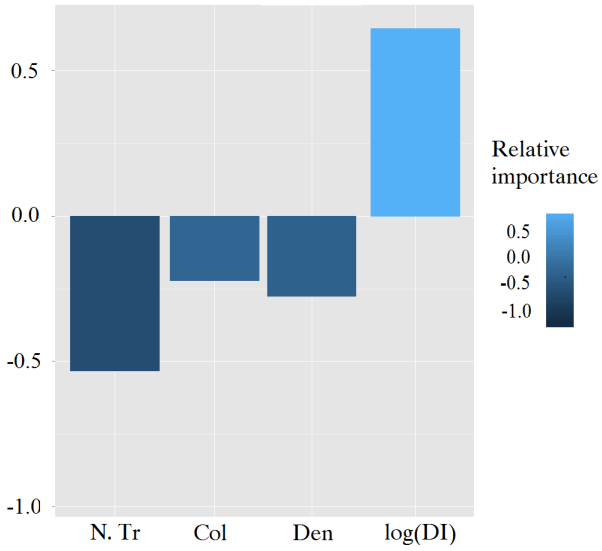


Figure 5.11: Relative influences of the predictors on the efficacy per treatment. Graphic derived from the neural network and agreeing with the results of the multilinear regression model.

## 5.5 Conclusion

The main goal of this Chapter was the prediction of the clinical efficacy. The Arrhenius damage integral did not give satisfactory results in our study, probably due to the use of average values for the optical properties, hair depth, hair inclination and hair thickness. Thus, we investigate two new statistical methods to reintroduce the missing variability; both the multiple linear regression and the neural network are robust and predict the treatment efficacy with an accuracy higher than 80%. Here, we use mainly the multiple linear regression for the efficacy prediction and the neural network to get an insight in the relationship between predictors and response.

We select the variables which are more influent in the treatment efficacy with a stepwise algorithm and we optimize the methods. However, both can still be improved.

First, redefining the efficacy per treatment: for the sake of simplicity we use a linear approximation defining the efficacy per treatment just dividing the final measured efficacy by the number of sessions. However, we know the subsequent sessions to have a cumulative effect on the treatment outcome and the efficacy as a function of the number of treatments to have a sigmoid shape. Thus we suggest the study of another method to estimate the efficacy of the single treatment.

Also, the predictive power of the models is seen to be strongly dependent on different conversions for the qualitative predictors, i.e hair color and treatment location. For the first, obtained through the conversion from the RGB to the gray scale, we recommend a refinement. This can be done, for example, by enlarging the number of color categories which define with more accuracy different browns or the blondish/reddish hair in the group gathering all those cases not black neither brown. For the location, we choose 1 and 2 as they showed the best results among the probed values. In fact, other choices such as $\{0, 1\}$ and $\{-1, 1\}$, lead to a model with lower predictive power. We interpret this as an insight in the influence of the two locations: both give a contribution to the efficacy, i.e none has zero coefficient, and they are not symmetric in the sense that they have not equal and opposite weight on the outcome of the treatment.

As said earlier, the neural network is used in parallel as a comparison and to interpret the results. We suggest the enhancement of the network. Since it has many degrees of freedom - i.e. number of hidden layers, number of neurons per layer and activation function - it can be arbitrarily improved.

For clinical purposes, we suggest the use of the multiple linear regression: it is tested and shows good predictions with an acceptable error.

# Chapter 6

# Mathematical analysis of a heat transfer model in biological tissues

In Chapter 4 we obtained the temperature variation inside the skin hair structure. The temperature profile is the numerical solution to the equation governing heat transfer inside the skin-hair structure and is obtained by using softwares for partial differential equations such as COMSOL Multiphysics. A preliminary dimensional analysis allows us to understand the role played by the different terms and to get an insight in characteristic lengths and time scales, useful parameters also for a suitable numerical approach. After setting an adequate functional framework, we transpose the boundary value problem into an abstract formulation and we study the well-posedness with specific methods from the theory of quasi-linear evolution equations. We prove the existence and uniqueness of weak solutions. First we consider a simplified linear case. Then, relaxing hypotheses, we get closer to the physical setting and we treat a quasi-linear problem.

## 6.1 Setting of the problem

Before focusing on the proof of the existence and the uniqueness of the solution, let us make some working hypotheses and remarks.

### 6.1.1 Geometry and parameters

The complexity of the real skin-hair structure is reduced to an elementary parallelepiped, a partition of the three layers (epidermis, dermis and fat) and the hair through these, i.e.

$$\begin{aligned} &\Omega = \Omega_E \cup \Omega_D \cup \Omega_F \cup \Omega_H \\ &\Omega_E \cap \Omega_D \cap \Omega_F \cap \Omega_H = \emptyset, \end{aligned} \tag{6.1}$$

where $\Omega_E, \Omega_D, \Omega_F, \Omega_H$ are depicted in Figure 6.1. The last condition means that the intersection of the subdomains is a set of null measure when we consider the Lebesgue measure $\lambda^3$ for volumes. Similarly, the external surface $\partial\Omega = \Gamma$ with normal outward unit vector $n$ is a partition of subsurfaces $\Gamma_D$, $\Gamma_N$, $\Gamma_R$ on which different boundary conditions are set

$$\begin{aligned} &\partial\Omega = \Gamma_D \cup \Gamma_R \cup \Gamma_N \\ &\Gamma_D \cap \Gamma_R \cap \Gamma_N = \emptyset, \end{aligned} \tag{6.2}$$

(see again Figure 6.1 for visualizing $\Gamma_D, \Gamma_R, \Gamma_N$). Here the last condition means that the intersection of the three parts of the surface is a set of null measure when the Lebesgue measure $\lambda^2$ for surfaces is considered. We assume in the following $\lambda^2(\Gamma_D) \neq 0$. On each layer characteristic properties (density, specific heat, thermal conductivity) are set. This would lead to a number of coupled governing equations corresponding to the number of distinguishable subdomains. In the

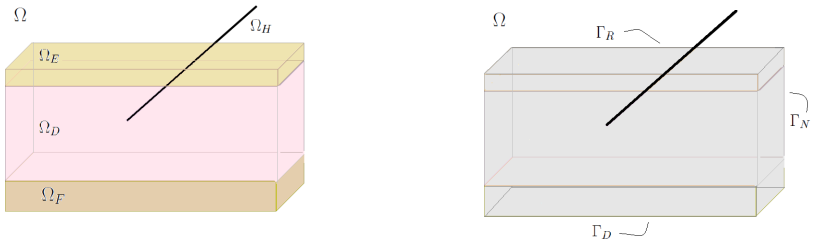


Figure 6.1: Domain Ω. Layers and boundary partition.

following we are assuming $\rho_i,\ c_{p_i},\ k_i \in L^\infty$ with $i \in \{E,\ D,\ F,\ H\}$ so that if we define the local solutions

$$T = \begin{cases} T_i & x \in \Omega_i \\ T_j & x \in \Omega_j \end{cases}, \tag{6.3}$$

at each interface $\Gamma_{ij}$ between the subdomains $i$ and $j$, then it holds the perfect transmission condition:

$$\begin{cases} T_i = T_j & \text{at } \Gamma_{ij} \\ j_{T_i} \cdot n = j_{T_j} \cdot n & \text{at } \Gamma_{ij} \end{cases}. \tag{6.4}$$

In other words, we want the continuity of the solution through the contact surfaces and consider a macroscopically homogeneous tissue in the remainder, with properties $\rho, c_p,\ k \in L^\infty$.

For what concerns the boundary conditions, they translate the physical phenomenon: on the internal surface $\Gamma_D$ (the bottom of the parallelepiped) the temperature is set to a fixed value, function of the depth; the flux through the lateral surface $\Gamma_N$ is set to zero to simulate the continuation of the domain. Finally, the upper surface $\Gamma_R$ is exposed to the ambient medium, so that here evaporation, convection and irradiation take place. The heat loss due to evaporation is modeled by

$$Q_{evap} = h_{fg} h_m [\rho_{v.sat}(T) - \rho_{v.\infty}], \tag{6.5}$$

which depends on the temperature through the density of the saturated water vapour $\rho_{v.sat}(T)$ and the other parameters are $\rho_{v,\infty}$ the density of water vapour in air at the ambient temperature (far enough from the heat source), $h_{fg}$ the phase-change enthalpy of water and $h_m$ the convection mass transfer coefficient. The convection is quantified through the Newton law of cooling with $h$ heat transfer coefficient and $T_{ext}$ the external temperature:

$$Q_{conv} = h(T_{ext} - T). \tag{6.6}$$

The radiation is modeled through the Stefan-Boltzmann law,

$$Q_{rad} = \sigma(T_{ext}^4 - T^4), \tag{6.7}$$

with $\sigma$ the homonym constant

$$\sigma = 5.67 \cdot 10^{-8} \left[ \frac{\mathrm{J}}{\mathrm{s} \cdot \mathrm{m}^2 \cdot \mathrm{K}^4} \right]. \tag{6.8}$$

Following the Pennes bioheat equation [14], the model is based on a diffusion-convection-reaction equation for the heat diffusion in the tissue; however, our assumption is that inside the skin it is not possible to detect a dominant flux in a given direction, but rather different velocities with diverging directions which on overall compensate each other; the convection velocity $u$ results then to be null. Note that the contribution of the tissue spraying is taken into account in the blood perfusion, modeled as

$$\mathcal{P}(T) = \omega_b \rho_b c_b (T - T_a), \tag{6.9}$$

where $\omega_b$ is the blood perfusion (defined in Chapter 4 as blood mass per tissue mass per second), $\rho_b$ and $c_b$ are the density and the specific heat of the blood, and $T_a$ is the temperature of the arterial blood. In the following we group under a new parameter $\alpha := \omega_b \rho_b c_b$. Recall that the laser radiation $f_\ell$ is modeled by a constant heat source corresponding to the light absorption quantified through the Monte Carlo simulation.

### 6.1.2 Basic functional spaces and inequalities

We define here the functional framework we are working in (for reference, see [23, 24]). After a brief introduction of the functional spaces and their norms, we gather the main theorems and inequalities which are largely used in the following.
$L^p(\Omega)$ $(1 \leq p < \infty)$ denotes the space of $p$-integrable measurable functions $v$ with finite Lebesgue norm,

$$\|v\|_{L^p(\Omega)} = \Big( \int_\Omega |v|^p \Big)^{1/p}. \tag{6.10}$$

For $p = \infty$, $L^\infty(\Omega)$ denotes essentially bounded functions,

$$\|v\|_{L^\infty(\Omega)} = \operatorname*{ess\,sup}_\Omega |v| \tag{6.11}$$

and $L^\infty_+(\Omega)$ is the space of the positive functions $v(x)$ limited almost everywhere. For $1 \leq p \leq \infty$, $L^p(\Omega)$ is a Banach space and particularly for $p = 2$, $L^2(\Omega)$ is a Hilbert space, with inner product

$$(u, v)_{L^2(\Omega)} = \int_\Omega uv dx. \tag{6.12}$$

The Sobolev space $W^{k,p}(\Omega)$ is the space of the functions of differentiability $k$ and integrability $p$. It consists of functions $v$ which are $k$-weakly differentiable and such that $D^\alpha v \in L^p(\Omega)$ for all $|\alpha| \leq k$. With the norm

$$\|v\|_{W^{p,k}(\Omega)} = \Big( \int_\Omega \sum_{|\alpha| \leq k} \|D^\alpha v\|^p dx \Big)^{1/p}, \tag{6.13}$$

the Sobolev spaces $W^{p,k}(\Omega)$ are Banach spaces. $W^{p,0}(\Omega)$ is essentially $L^p(\Omega)$ while when $p = 2$, we use a different notation $H^k(\Omega) = W^{2,k}(\Omega)$ because those are Hilbert spaces when we consider the inner product

$$(u, v)_{H^k(\Omega)} = \int_\Omega \sum_{|\alpha| \leq k} D^\alpha u D^\alpha v dx. \tag{6.14}$$

Note that $H^0(\Omega) = L^2(\Omega)$ and that $H^1(\Omega)$ denotes the space of functions $v$ of finite Sobolev norm

$$\|v\|^2_{H^1(\Omega)} = \int_\Omega (|\nabla v|^2 + |v|^2). \tag{6.15}$$

If the domain $\Omega$ is bounded with Lipschitz boundary $\Gamma = \partial\Omega$, then there exists a bounded linear operator $\tau : W^{1,p}(\Omega) \longrightarrow L^p(\Gamma)$ such that

$$\begin{aligned} \tau v &= v|_\Gamma && v \in W^{1,p}(\Omega) \cap C(\bar{\Omega}) \\ \|\tau v\|_{L^p(\Gamma)} &\leq C(p, \Omega) \|v\|_{W^{1,p}(\Omega)} && v \in W^{1,p}(\Omega) \end{aligned} \tag{6.16}$$

$\tau v$ is called trace of $v$ and is essentially the restriction of the function to the boundary of the considered domain. The trace operator is generally non surjective, but for $1 < p < \infty$ maps into the space $W^{1-\frac{1}{p},p}(\Gamma)$. Thus, in the case $p = 2$, we consider the Hilbert space for the trace $H^{\frac{1}{2}}$. This is a particular case of the fractional Sobolev spaces, defined below. Given a domain $\Omega \subseteq \mathbb{R}^n$, $1 \leq p < \infty$ and $0 < s < 1$, we define the space $W^{s,p}(\Omega)$ as the space of functions $v \in L^p(\Omega)$ for which it is defined the norm

$$\|v\|^p_{W^{s,p}(\Omega)} \coloneqq \|v\|^p_{L^p(\Omega)} + \int\int_{\Omega \times \Omega} \frac{|u(y) - u(x)|^p}{|y - x|^{sp+n}} dy\, dx. \tag{6.17}$$

Observe that the spaces $W^{s,p}(\Omega)$ are Banach spaces when associated with this norm.

Also, it is important to have an explicit characterization of the dual space of $H_0^1(\Omega)$, denoted by $H^{-1}(\Omega)$. In other words, $H^{-1}(\Omega)$ is the set of the bounded linear functionals $f$ on $H_0^1(\Omega)$ with norm

$$\|f\|_{H^{-1}(\Omega)} = \sup\{\langle f, v\rangle | v \in H_0^1(\Omega), \|v\|_{H_0^1(\Omega)} \leq 1\}. \tag{6.18}$$

Here $\langle \cdot, \cdot \rangle$ denotes the pairing between $H^{-1}(\Omega)$ and $H_0^1(\Omega)$. Note that the notation with negative apex for the Hilbert and Sobolev spaces holds in general for the corresponding dual spaces, and not only in the proposed case of $H^1$.

When we study time-dependent problems, we consider some other sorts of Sobolev spaces, these comprising functions mapping time into Banach spaces. Let $X$ denote a general real Banach space, with norm $\|\cdot\|$; then, the space $L^p(0, t_{final}; X)$ consists of all measurable functions $v : [0, t_{final}] \longrightarrow X$ with

$$\|v\|_{L^p(0,t_{fianl});X} \coloneqq \Big( \int_0^{t_{final}} \|v(t)\|^p dt \Big)^{1/p} < \infty \tag{6.19}$$

for $1 \leq p < \infty$, and

$$\|v\|_{L^\infty(0,t_{final};X)} \coloneqq \operatorname{ess} \sup_{0 \leq t \leq t_{final}} \|v(t)\| < \infty. \tag{6.20}$$

Similarly $H^1(S; L^2(\Omega))$ is the set of functions $v(t, \cdot) \in H^1(\Omega)$ for almost every $t \in S$ and

$$\int_0^{t_{final}} \|v(t, \cdot)\|_{L^2(\Omega)} dt < \infty. \tag{6.21}$$

$L_+^\infty(\Omega \times S)$ is the analogous of $L^\infty(\Omega)$ for positive functions of two variables $v(x, t)$ limited almost everywhere in both time and space.

*Holder inequality* Let $(S, \Sigma, \mu)$ be a measure space and let $p, q \in [1, \infty]$ with $\frac{1}{p} + \frac{1}{q} = 1$. Then, for all measurable functions $f$ and $g$ on s,

$$\|fg\|_{L^1(\Omega)} \leq \|f\|_{L^p(\Omega)} \|g\|_{L^q(\Omega)}. \tag{6.22}$$

*Cauchy-Schwartz inequality* Particular case of the Holder inequality when $p = q = \frac{1}{2}$

$$\|fg\|_{L^1(\Omega)} \leq \|f\|_{L^2(\Omega)} \|g\|_{L^2(\Omega)}. \tag{6.23}$$

*Minkowski inequality* suppose $f$ and $g$ are Lebesgue measurable. Then, for any $1 < p < \infty$

$$\|f + g\|_p \leq \|f\|_p + \|g\|_p, \tag{6.24}$$

with the cases $p = 1$ and $p = \infty$ coincident with the triangle inequality.

*Young inequality* given two positive numbers $a, b \geq 0$ and $p, q > 0$ with $\frac{1}{p} + \frac{1}{q} = 1$, then

$$ab \leq \frac{a^p}{p} + \frac{b^q}{q}. \tag{6.25}$$

In particular,

$$ab \leq \frac{a^2}{2} + \frac{b^2}{2}, \tag{6.26}$$

and

$$ab \leq \frac{a^2}{2\varepsilon} + \frac{\varepsilon b^2}{2}. \tag{6.27}$$

*Poincarè inequality* Let $\Omega$ be a limited open set. Then, there exists a constant $c_\Omega > 0$ such that for any function $v \in H_0^1(\Omega)$

$$\|v\|_{L^p(\Omega)} \leq c_\Omega \|\nabla v\|_{L^p(\Omega)}. \tag{6.28}$$

*Gauss theorem* Let $X : \Omega \longrightarrow \mathbb{R}^n$ be a $C^1$ vector field with $\Omega$ open bounded set with $C^1$-boundary. Then

$$\int_\Omega \mathrm{div} X dx = \int_{\partial\Omega} X \cdot n ds \tag{6.29}$$

with $n$ normal unit vector to the boundary $\partial\Omega$.

*Trace inequality* As we showed earlier, the trace operator satisfies the inequality

$$\|v\|_{H^{s-1/2}(\Gamma)} \leq c_s \|v\|_{H^s(\Omega)}. \tag{6.30}$$

*Gronwall inequality* Let $v : [0, t_{final}] \longrightarrow \mathbb{R}$ be a bounded nonnegative measurable function and $u : [0, t_{final}] \longrightarrow \mathbb{R}$ a nonnegative summable function for which there exists a constant $C$ such that

$$v'(t) \leq Cv(t) + u(t) \quad \text{for all } t \in S, \tag{6.31}$$

and initial condition $v(0) = v_0$. Then

$$v(t) \leq \exp(Ct)(v_0 + \int_0^t u(s)ds), \quad \text{for } 0 \leq t \leq t_{final}.$$

### 6.1.3 Setting of the model equations

We consider the time interval $S \coloneqq (0, t_{final}]$, with final instant of observation $t_{final} \in \mathbb{R}^+$. Based on the considerations in Chapter 4 and in Section 6.1.1, the problem can be stated as follows:

**Problem 1.** *Find $T(x,t)$ with $x \in \Omega$ and $t \in S$ satisfying*

$$\begin{cases} \partial_t(\rho(T)c_p(T)T) + div(-k(T)\nabla T) = \mathcal{P}(T) + f_{mp} + f_\ell\, \chi_\ell & \Omega \times S \\ -k\nabla T \cdot n = 0 & \Gamma_N \times S \\ T = T_D & \Gamma_D \times S \\ -k\nabla T \cdot n = h(T_{ext} - T) + Q_{evap} + \sigma(T_{ext}^4 - T^4) & \Gamma_R \times S \\ T(0,x) = T(t=0) = T_0 & \Omega \times (t=0) \end{cases} .$$

The notation $\chi_\ell(x,y,z,t)$ refers to the characteristic function which assumes unit value in the domain $\Omega_H$ for the limited time interval $S_\ell$ in which the energy is delivered, and vanishes elsewhere i.e.

$$\chi_\ell(x,y,z,t) = \begin{cases} 1 & (x,y,z) \in \Omega_H,\ t \in S_\ell \\ 0 & (x,y,z) \notin \Omega_H,\ t \notin S_\ell \end{cases} . \tag{6.32}$$

### 6.1.4 Setting of the working hypotheses

We consider the following hypotheses to be fulfilled:

(H1) $f_{mp} \in \mathbb{R}$;

(H2) $f_l = f_l(x,y,z) \geq 0$, for all $(x,y,z) \in \Omega$;

(H3) $\rho,\ c_p,\ \alpha,\ h,\ \sigma \in \mathbb{R}_+^*$ and $k$ is either in $\mathbb{R}_+^*$ or a strictly positive function of the temperature $T$, depending on the context;

(H4) $T_a \in L_+^\infty(\Omega \times S),\ T_D \in L_+^\infty(\Gamma_D \times S) \cap H^{\frac{1}{2}}(\Gamma_D),\ T_{ext} \in L_+^\infty(\Gamma_R \times S),\ T_0 \in L_+^\infty(\Omega)$;

(H5) $\frac{\partial}{\partial t} + L$ is an uniformly parabolic operator: it exists some positive constant $\theta > 0$ such that

$$\sum_{i,j=1}^n k^{ij}(x,t,T)\zeta_i\zeta_j \geq \theta|\zeta|^2 \quad \text{for all } (x,t) \in \Omega \times S,\ \zeta \in \mathbb{R}^n;$$

further $k$ is assumed to be symmetric. In the treated case, $k^{ij} = k$ for all $i,j = \{1,\dots,n\}$.

| variable | symbol | unit of measure | dimension |
|---|---|---|---|
| density | $\rho$ | $\frac{\mathrm{kg}}{\mathrm{m}^3}$ | $\frac{\mathrm{M}}{\mathrm{L}^3}$ |
| specific heat | $c_p$ | $\frac{\mathrm{J}}{\mathrm{kg\ K}}$ | $\frac{\mathrm{L}^2}{\mathrm{T}^2\ \theta}$ |
| thermal conductivity | $k$ | $\frac{\mathrm{W}}{\mathrm{m\ K}}$ | $\frac{\mathrm{M\ L}}{\mathrm{T}^3\ \theta}$ |
| heat transfer coefficient | $h$ | $\frac{\mathrm{W}}{\mathrm{m}^2\ \mathrm{K}}$ | $\frac{\mathrm{M}}{\mathrm{T}^3\theta}$ |
| radiative coefficient (Stefan-Boltzmann constant) | $\sigma$ | $\frac{\mathrm{J}}{\mathrm{s\ m}^2\ \mathrm{K}^4}$ | $\frac{\mathrm{M}}{\mathrm{T}^3\ \theta^4}$ |
| convection mass transfer coefficient | $h_m$ | $\frac{\mathrm{kg}}{\mathrm{s}}$ | $\frac{\mathrm{M}}{\mathrm{T}}$ |
| perfusion rate | $\omega_b$ | $\frac{\mathrm{m}_b^3}{\mathrm{s\ m}_t^3}$ | $\frac{1}{\mathrm{T}}$ |
| phase change enthalpy | $h_{fg}$ | $\frac{\mathrm{J}}{\mathrm{kg}}$ | $\frac{\mathrm{L}}{\mathrm{T}^2}$ |

Table 6.1: Dimensions and units of measure of parameters involved in the governing equation 6.33.

## 6.2 Dimensional analysis

In this section we non-dimensionalise the governing equation; we simply wish to understand the dominant physical processes using their natural dimensions and typical values. In particular, we are concerned with the radiative heat transfer, which is often neglected in bioheat analysis. The dimensional analysis is used to give an insight in the time scales and characteristic lengths, which are useful to tune the numerical solution (e.g. set the discretization step in the finite element methods).

Assume the parameters involved in Problem 1 to be independent of the temperature. In this case, the governing equations are

$$\begin{cases} \partial_t(\rho\ c_p\ T) + div(-k\nabla T) = \omega_b\ \rho_b\ c_b(T - T_a) + f_{mp} + f_\ell\ \chi_\ell & \Omega \times S \\ -k\nabla T \cdot n = 0 & \Gamma_N \times S \\ T = T_D & \Gamma_D \times S \\ -k\nabla T \cdot n = h(T_{ext} - T) + Q_{evap} + \sigma(T_{ext}^4 - T^4) & \Gamma_R \times S \\ T(0,x) = T(t=0) = T_0 & \Omega \times (t=0) \end{cases} \tag{6.33}$$

The fundamental dimensions are mass M, length L, time T and temperature $\theta$ while the parameters are listed in Table 6.1, with their unit of measure and dimension. We rescale the problem with respect to the reference quantities corresponding to the fundamental variables, $M_{ref}$, $x_{ref}$, $t_{ref}$ and $T_m = \|T\|_{L^\infty(S\times\Omega)}$; we derive the governing equations as functions of the dimensionless fundamental quantities $\hat{x}$, $\hat{t}$, $\hat{T}$,

$$\begin{aligned} T &= T_m\ \hat{T}, \\ x &= x_{ref}\ \hat{x}, \\ t &= t_{ref}\ \hat{t}. \end{aligned}$$

The dimensionless system of equations is thus

$$\begin{cases} \partial_t \hat{T} - \dfrac{k\, t_{ref}}{\rho c_p\, x_{ref}^2}\Delta\hat{T} = \dfrac{\alpha\, t_{ref}}{\rho c_p}(\hat{T}-\hat{T}_a) + \dfrac{t_{ref}\, f_{ref}}{\rho c_p\, T_m}(\hat{f}_{mp} + \hat{f}_\ell\, \chi_\ell) & \Omega\times S \\ -\nabla\hat{T}\cdot n = 0 & \Gamma_N\times S \\ \hat{T} = \hat{T}_D & \Gamma_D\times S \\ -\nabla\hat{T}\cdot n = \dfrac{h\, x_{ref}}{k}(\hat{T}_{ext}-\hat{T}) + \dfrac{x_{ref}\, Q_{ref}}{k\, T_m}\hat{Q}_{evap} + \dfrac{x_{ref}\,\sigma}{k}T_m^3(\hat{T}_{ext}^4-\hat{T}^4) & \Gamma_R\times S \\ \hat{T}(0,x) = \hat{T}(t=0) = \hat{T}_0 & \Omega\times(t=0) \end{cases} \tag{6.34}$$

Where $f_{mp} = f_{ref}\hat{f}_{mp}$ and $f_l = f_{ref}\hat{f}_l$. Note that $f_{ref}$ is the reference heat source, a bulk quantity, with

$$[f_{ref}] = \frac{\mathrm{W}}{\mathrm{m}^3}. \tag{6.35}$$

Further, the reference quantity of the heat lost through the surfaces is $Q_{ref}$ with

$$[Q_{ref}] = \frac{\mathrm{W}}{\mathrm{m}^2}. \tag{6.36}$$

The five coefficients in (6.34) are dimensionless, for dimensions of the involved parameters we refer to Table 6.1. We introduce now the typical values for heat transfer in light irradiated tissues to evaluate the driving physical processes in the governing equations.
The characteristic length is set according to the domain dimensions to $x_{ref} = 1$ mm. Since the skin-hair structure is composed by various components with different properties, the density $\rho$ varies between 1200 and 1310 [kg/m$^3$], the heat capacity $c_p$ between 1900 and 3800 [J/(kg m$^3$)] while for the blood is almost $c_b \sim 4000$ [J/(kg m$^3$)]. The heat conduction coefficient $k$ ranges in $(0.21, 0.61)$ [W/(m K)]. The estimation of the perfusion term follows [25] and is based on the constant values of $w_b = 0.028$ [m$_b^3$/(m$_t^3$ s)] for the perfusion rate, $\rho_b = 1080$ [kg/m$^3$] for the blood density and $c_b = 3500$ [J/(kg K)] its heat capacity. The rate of heat production due to metabolic processes is found at very different values in literature. However, we set $Q_{met} = 245$ [W/m$^3$] (following [16]). For the heat source we set $f_\ell$ corresponding to fluences of $(10, 12)$ [J/cm$^2$]. The surface heat transfer coefficient $h$ is set to a values in $(8, 10)$ [W/(m$^2$ K)] when the skin is exposed to the air. $\sigma$ is the Stefan Boltzmann constant introduced earlier (6.8). The typical value for $Q_{ref}$ is derived from a quantitative approximation (6.5) of the heat loss due to evaporation in a $(10^3, 10^4)$ [W/m$^2$] range. The temperature during light treatment varies in a wide range and we choose two typical values, namely $T_m = 60$℃ corresponding to chemical denaturation and $T_m = 100$℃ for water evaporation.

Finally, the time reference $t_{ref}$. We derive the diffusion time constant and use it as a time reference setting the diffusion coefficient to the unit:

$$t_{ref} = \frac{\rho\, c_p\, x_{ref}^2}{k} \sim (3.738, 23.7)\ [s]. \tag{6.37}$$

Note that other reference times can be chosen. From these considerations, we derive typical values for each dimensionless number (see Table 6.2).

As expected, and according with the literature [20], we see that the perfusion term can be neglected in the governing equation.

The physical terms involved in the external boundary conditions are all found to vary between $10^{-3}$ and $10^{-1}$. Thus we conclude that the term for the radiative heat transfer can not be neglected in the study of light-based treatments since high temperatures might be reached. In the study of the well posedness of the governing equations, we neglect this term for the sake of simplicity.

| dimensionless number | expression | typical value |
|---|---|---|
| $\mathcal{J}_1$ | $\frac{k\ t_{ref}}{\rho\ c_p\ x_{ref}^2}$ | 1 |
| $\mathcal{J}_2$ | $\frac{w_b\ \rho_b\ c_b\ t_{ref}}{\rho\ c_p}$ | $[0.008, 0.11]$ |
| $\mathcal{J}_3$ | $\frac{f_{ref}\ t_{ref}}{\rho\ c_p\ T_m}$ | $[0.1, 1.56]$ |
| $\mathcal{J}_4$ | $\frac{h\ x_{ref}}{k}$ | $[0.0131, 0.0476]$ |
| $\mathcal{J}_5$ | $\frac{x_{ref}\ Q_{ref}}{k\ T_m}$ | $[0.0044, 0.143]$ |
| $\mathcal{J}_6$ | $\frac{x_{ref}\ \sigma\ T_m^3}{k}$ | $[0.0034, 0.0140]$ |

Table 6.2: Dimensionless groups with their typical values.

## 6.3 Existence and uniqueness for a linear case

In this section, we study the well posedness of the linear problem. Thus, we make the additional assumption

(H6.a) the parameters $\rho$, $c_p$, $k$ and the natural metabolic processes $f_{mp}$ are independent of the temperature. Furthermore, $\sigma = 0$.

*Remark.* When the tissue properties are assumed to be independent of the temperature, $Q_{evap}$ defined in (6.5) is a constant.

If (H1)-(H6) hold, Problem 1 can be rewritten as

$$\begin{cases} \rho c_p \partial_t T + div(-k\nabla T) = \alpha(T - T_a) + f_{mp} + f_\ell\ \chi_\ell & \Omega \times S \\ -k\nabla T \cdot n = 0 & \Gamma_N \times S \\ T = T_D & \Gamma_D \times S \\ -k\nabla T \cdot n = h(T_{ext} - T) & \Gamma_R \times S \\ T(0,x) = T_0 & \Omega \times (t = 0) \end{cases} . \tag{6.38}$$

The corresponding problem with homogeneous Dirichlet boundary condition can be derived introducing $\tilde{T} = T - T_D$, where $T$ is a solution of (6.38). Since $T_D$ is constant in both time and space, the new variable satisfies the partial differential equation

$$\begin{cases} \rho c_p \partial_t \tilde{T} + div(-k\nabla \tilde{T}) - \alpha(\tilde{T} + T_D - T_a) = f_{mp} + f_\ell\ \chi_\ell & \Omega \times S \\ -k\nabla \tilde{T} \cdot n = 0 & \Gamma_N \times S \\ \tilde{T} = 0 & \Gamma_D \times S \\ -k\nabla \tilde{T} \cdot n = h(T_{ext} - \tilde{T} - T_D) & \Gamma_R \times S \\ \tilde{T}(0,x) = T_0 - T_D & \Omega \times (t = 0) \end{cases} . \tag{6.39}$$

In the following we denote $f = f_{mp} + f_\ell\ \chi_\ell$ and we simply indicate $\tilde{T}$ by $T$ when referring to the solution of the problem with homogeneous boundary conditions (6.39).

**Weak formulation**
Assume $T \in L^2(S; H_D^1(\Omega)) \cap H^1(S; L^2(\Omega))$ and consider a test function which vanishes on the

part of the boundary where the solution is imposed, $\varphi \in H^1_D(\Omega) \coloneqq \{\varphi \in H^1(\Omega) \text{ such that } \varphi = 0 \text{ on } \Gamma_D\}$. Then, for all $\varphi \in H^1_D(\Omega)$,

$$\begin{aligned}
\int_\Omega (\rho c_p \partial_t T - k\Delta T - \alpha(T + T_D - T_a))\varphi &= \textstyle\int_\Omega f\varphi \\
\rho c_p \int_\Omega \partial_t T\varphi - k\int_\Omega \Delta T\varphi - \alpha\int_\Omega (T + T_D - T_a)\varphi &= \textstyle\int_\Omega f\varphi \\
\rho c_p \int_\Omega \partial_t T\varphi - k\int_\Omega \nabla\cdot(\nabla T\varphi) + k\int_\Omega \nabla T\nabla\varphi - \alpha\int_\Omega (T + T_D - T_a)\varphi &= \textstyle\int_\Omega f\varphi \\
\rho c_p \int_\Omega \partial_t T\varphi - k\int_{\partial\Omega} (\nabla T\varphi)\cdot n + k\int_\Omega \nabla T\nabla\varphi - \alpha\int_\Omega (T + T_D - T_a)\varphi &= \textstyle\int_\Omega f\varphi.
\end{aligned}$$

The second boundary integral is derived applying the Gauss theorem and can be decomposed on the surfaces:

$$\begin{aligned}
-k\int_{\partial\Omega} (\nabla T\varphi)\cdot n &= -k\int_{\Gamma_N} (\nabla T\cdot n)\varphi - k\int_{\Gamma_D} (\nabla T\cdot n)\varphi - k\int_{\Gamma_R} (\nabla T\cdot n)\varphi \\
&= -k\int_{\Gamma_R} (\nabla T\cdot n)\varphi = \int_{\Gamma_R} h(T_{ext} - T - T_D)\varphi,
\end{aligned} \tag{6.40}$$

while the integrals on $\Gamma_N$ and $\Gamma_D$ vanish for the imposed boundary conditions. If we denote $T_1 \coloneqq T_{ext} - T_D$ and $T_2 \coloneqq T_D - T_a$, we get the weak formulation

$$\rho c_p \int_\Omega \partial_t T\varphi + \int_{\Gamma_R} h(T_1 - T)\varphi + k\int_\Omega \nabla T\nabla\varphi - \alpha\int_\Omega (T + T_2)\varphi = \int_\Omega f\varphi \qquad \text{for all } \varphi \in H^1_D(\Omega). \tag{6.41}$$

and, in the particular case of $T_{ext} = T_D = T_a$, the weak formulation becomes

$$\rho c_p \int_\Omega \partial_t T\varphi - \int_{\Gamma_R} hT\varphi + k\int_\Omega \nabla T\nabla\varphi - \alpha\int_\Omega T\varphi = \int_\Omega f\varphi \qquad \text{for all } \varphi \in H^1_D(\Omega). \tag{6.42}$$

**Definition 6.3.1.** We call $T \in L^2(S; H^1_D(\Omega)) \cap H^1(S; L^2(\Omega))$ satisfying (6.42) for all $t \in S$ a weak solution to Problem 1.

**Theorem 6.3.1.** *Assume (H1)-(H6) to hold. Then it exists a unique weak solution to (6.38) in the sense of Definition 6.3.1.*

*Proof.* The proof consists of 4 steps: first, we derive the Galerkin system of equations and we prove it admits a unique solution, then we pass to the limit for the dimension of the projection space to find the solution of the weak formulation. Finally, we recover the weak formulation and we prove the uniqueness of its solutions.

**Step 1: Galerkin discretization.** Given an orthonormal basis (with respect to the norm in $L^2$) $\{w_k\}_{k=1}^\infty$ for the considered space $L^2(\Omega)$, the solution to the PDE (6.39) can be approximated by

$$T_m = \sum_{k=1}^m d_k(t) w_k(x). \tag{6.43}$$

We have $T_m \in S_m = \text{span}\{w_1, \dots, w_n\}$ and it is a function in $L^2(S; H^1_D(\Omega)) \cap H^1(S; L^2(\Omega))$ for all $t \in S$. The initial conditions on the coefficients are given by

$$d_k(0) = (T_0 - T_D, w_k), \tag{6.44}$$

since the expression for the $d_k$ is given by $d_k(t) = \int_\Omega T_m w_k$ and the basis functions are orthonormal. Plugging the piecewise linear approximation of the solution (6.43) in the weak formulation (6.42)

and choosing $\varphi = w_j$ (a function of the basis) as test function,

$$\underbrace{\rho c_p \int_\Omega \partial_t T_m w_j}_{(a)} - \underbrace{\int_{\Gamma_R} h T_m w_j}_{(b)} + \underbrace{k \int_\Omega \nabla T_m \nabla w_j}_{(c)} - \underbrace{\alpha \int_\Omega T_m w_j}_{(d)} = \underbrace{\int_\Omega f w_j}_{(e)}, \tag{6.45}$$

for every $t$ in $S$.

**Lemma 6.3.2.** *Under the working hypotheses (H1)-(H6) there exists a unique solution $T_m \in S_m$ defined in (6.43) to (6.45).*

*Proof.* The terms in equation 6.45 can be rewritten as

$$(a) \qquad \rho c_p \int_\Omega \partial_t T_m w_j = \rho c_p \int_\Omega \sum_{k=1}^m d_k'(t) w_k(x) w_j(x) = \rho c_p \sum_{k=1}^m d_k'(t) \int_\Omega w_k w_j = \rho c_p d_j'(t).$$

$$(b) \qquad \int_{\Gamma_R} h T_m w_j = \int_{\Gamma_R} h \sum_{k=1}^m d_k(t) w_k(x) w_j(x) = h \sum_{k=1}^m d_k(t) \int_{\Gamma_R} w_k w_j = h d_j(t).$$

$$(c) \qquad k \int_\Omega \nabla T_m \nabla w_j = k \int_\Omega \sum_{k=1}^m d_k(t) \nabla w_k(x) \nabla w_j(x) = k \sum_{k=1}^m d_k(t) (\nabla w_k, \nabla w_j).$$

$$(d) \qquad \alpha \int_\Omega T_m w_j = \alpha \int_\Omega \sum_{k=1}^m d_k(t) w_k(x) w_j(x) = \alpha \sum_{k=1}^m d_k(t) \int_\Omega w_k w_j = \alpha d_j(t).$$

$$(e) \qquad \int_\Omega f w_j = f_j.$$

Plugging the results $(a) - (e)$ into (6.45), we get

$$\rho c_p d_j'(t) - h d_j(t) + k \sum_{k=1}^m d_k(t) (\nabla w_k, \nabla w_j) - \alpha d_j(t) = f_j \qquad \text{for all } j = 1, \dots, m. \tag{6.46}$$

We refer to the set of equations (6.46) as the Galerkin system of equations, obtained by approximating the weak solution through piecewise linear functions.

The Galerkin equations are in our case a system of ordinary differential equations with constant coefficients and initial condition (6.44); then it exists a unique solution $\underline{d} = (d_1(t), \dots, d_m(t))$, absolutely continuous, for every $t \in S$ (it is a classical result for ODE, see for example [26]). As a consequence, the linear approximation $T_m$ is uniquely defined and solves the projection problem (6.45) for every $t \in S$. □

**Step 2: Passing to the limit $m \longrightarrow \infty$.** We attempt now to pass to the limit $m \longrightarrow \infty$, extending the projection space $S_m$ to the given space $\Omega$. This is the way we treat the existence of the solution of the weak formulation.

**Lemma 6.3.3.** (Energy estimate) There exists a positive constant $C$, depending only on $\Omega$, $t_{final}$ and on the coefficients of the parabolic operator, such that

$$\max_{0 \le t \le t_{final}} \|T_m\|^2_{L^2(\Omega)} + \|T_m\|^2_{L^2(S;H^1(\Omega))} + \|T_m'\|^2_{L^2(S;H^{-1}(\Omega))} \le C\Big( \|T_0\|^2_{L^2(\Omega)} + \|f\|^2_{L^2(S;L^2(\Omega))} \Big). \tag{6.47}$$

*Proof.* Choose the test function in the weak formulation (6.42) to be the solution of the projection problem, $\varphi = T_m$.

$$\underbrace{\rho c_p \int_\Omega \partial_t T_m T_m}_{(a)} + \underbrace{k \int_\Omega \nabla T_m \nabla T_m}_{(b)} = \underbrace{\int_\Omega f T_m}_{(c)} + \underbrace{\int_{\Gamma_R} h T_m T_m}_{(d)} + \underbrace{\alpha \int_\Omega T_m T_m}_{(e)} \tag{6.48}$$

for every $t \in S$. Considering now term by term and recalling that $T_m \in L^2(S; H^1_D(\Omega)) \cap H^1(S; L^2(\Omega))$

$$
\begin{aligned}
&(a) \qquad \rho c_p \int_\Omega \partial_t T_m T_m = \rho c_p (T_m', T_m)_{L^2(\Omega)} = \rho c_p \frac{d}{dt}\Big(\frac{1}{2}\|T_m\|^2_{L^2(\Omega)}\Big)\\
&(b) \qquad \int_\Omega k \nabla T_m \nabla T_m = k\|\nabla T_m\|^2_{L^2(\Omega)} \geq \frac{k}{1+C_P^2}\|T_m\|^2_{H^1(\Omega)}\\
&(c) \qquad \int_\Omega f T_m = (f, T_m) \leq \frac{1}{2}\|f\|^2_{L^2(\Omega)} + \frac{1}{2}\|T_m\|^2_{L^2(\Omega)}\\
&(d) \qquad \int_{\Gamma_R} h T_m T_m = h\|T_m\|^2_{L^2(\Gamma_R)} \leq h C_{\Gamma_R}\|\nabla T_m\|^2_{L^2(\Omega)} \leq h C_{\Gamma_R}\|T_m\|^2_{H^1(\Omega)}\\
&(e) \qquad \alpha \int_\Omega T_m T_m = \alpha \|T_m\|^2_{L^2(\Omega)}.
\end{aligned}
$$

Plugging in these inequalities, it results

$$
\rho c_p \frac{d}{dt}\Big(\frac{1}{2}||T_m||^2_{L^2(\Omega)}\Big) + \Big(\frac{k}{1+C_P^2} - hC_{\Gamma_R}\Big)\|T_m\|^2_{H^1(\Omega)} \leq \frac{1}{2}||f||^2_{L^2(\Omega)} + (\alpha + \frac{1}{2})||T_m||^2_{L^2(\Omega)}
$$

Thus, setting

$$
C_0 = \frac{k}{\rho c_p (1+C_P^2)} - \frac{hC_{\Gamma_R}}{\rho c_p}, \quad C_1 = \frac{1/2+\alpha}{\rho c_p}, \quad C_2 = \frac{1}{2\rho c_p},
$$

we get for every $t \in S$

$$
\frac{d}{dt}\Big(||T_m||^2_{L^2(\Omega)}\Big) + C_0\|T_m\|^2_{H^1(\Omega)} \leq C_1\|T_m\|^2_{L^2(\Omega)} + C_2||f||^2_{L^2(\Omega)}. \tag{6.49}
$$

Now denote $\eta(t) = \|T_m(t)\|^2_{L^2(\Omega)}$ and $\zeta(t) = C_2\|f(t)\|^2_{L^2(\Omega)}$, so that (6.49) can be rewritten

$$
\eta'(t) \leq C_1\eta(t) + \zeta(t). \tag{6.50}
$$

Since $\eta(t)$ is a non negative continuous function on $S$, $C_1$ is a positive constant and $\zeta(t)$ is a non negative summable function on $S$, we can apply the Gronwall's inequality in the differential form to (6.50) to get

$$
\eta(t) \leq e^{C_1 t}\Big(\eta(0) + \int_0^t \zeta(s)ds\Big), \quad 0 \leq t \leq t_{final}. \tag{6.51}
$$

Since $d_k(0) = (T_0, w_k)$,

$$
\eta(0) = \|T_m(0)\|_{L^2(\Omega)} \leq \|T_0\|_{L^2(\Omega)}. \tag{6.52}
$$

Thus (6.51) can be rewritten as

$$
\begin{aligned}
\|T_m(t)\|^2_{L^2(\Omega)} &\leq e^{C_1 t}\Big(\|T_m(0)\|^2_{L^2(\Omega)} + \int_0^{t_{final}} C_2\|f(s)\|^2_{L^2(\Omega)}\Big)\\
&\leq e^{C_1 t}\Big(\|T_0\|^2_{L^2(\Omega)} + \int_0^{t_{final}} C_2\|f(s)\|^2_{L^2(\Omega)}\Big)
\end{aligned}
$$

and since $t \in S = [0, t_{final}]$, $e^{C_1 t}$ is limited: $e^{C_1 t} \leq e^{C_1 t_{final}} \leq C_t$ on a limited interval of time,

$$
\begin{aligned}
&\max_{t\in S}\|T_m(t)\|^2_{L^2(\Omega)} \leq C_t\Big(\|T_0\|^2_{L^2(\Omega)} + C_2\|f\|^2_{L^2(S;L^2(\Omega))}\Big)\\
&\max_{t\in S}\|T_m(t)\|^2_{L^2(\Omega)} \leq C\Big(\|T_0\|^2_{L^2(\Omega)} + \|f\|^2_{L^2(S;L^2(\Omega))}\Big).
\end{aligned} \tag{6.53}
$$

Returning now to the inequality (6.49) and integrating over the time interval, we have using the result above that

$$\|T_m(t)\|^2_{L^2(S;H^1(\Omega))} = \int_0^{t_{final}} \|T_m(t)\|^2_{H^1(\Omega)} \leq C\Big(\|T_0\|^2_{L^2(\Omega)} + \|f\|^2_{L^2(S;L^2(\Omega))}\Big). \tag{6.54}$$

Consider now a function $v \in H^1_0(\Omega)$ with $\|v\|_{H^1_0(\Omega)} \leq 1$ and call $v^1$ and $v^2$ the two components of the orthogonal decomposition of $v$ with respect to $\Omega_m = \text{span}\{w_k\}_k$,

$$v = v^1 + v^2, \quad v^1 \in \Omega_k, \quad (v^2, w_k) = 0, \text{ for all } k = 1, \dots, m.$$

From the properties of $v$,

$$\|v^1\|_{H^1_0(\Omega)} \leq \|v\|_{H^1_0(\Omega)} \leq 1.$$

Using now $v^1$ as test function in the weak formulation (6.42) we obtain

$$\rho c_p \int_\Omega \partial_t T_m v^1 - \int_{\Gamma_R} h T_m v^1 + k \int_\Omega \nabla T_m \nabla v^1 - \alpha \int_\Omega T_m v^1 = \int_\Omega f v^1 \qquad \text{for all } v^1 \in H^1_0(\Omega).$$

Since we can rewrite

$${}_{H^{-1}(\Omega)}\langle T'_m, v\rangle_{L^2(\Omega)} = (T'_m, v)_{L^2(\Omega)} = (T'_m, v^1)_{L^2(\Omega)}, \tag{6.55}$$

the previous equation becomes

$$\rho c_p (T'_m, v)_{L^2(\Omega)} = (f, v^1)_{L^2(\Omega)} + h(T_m, v^1)_{L^2(\Gamma_R)} - k(\nabla T_m, \nabla v^1)_{L^2(\Omega)} + \alpha (T_m, v^1)_{L^2(\Omega)}.$$

From this, we can estimate the inequality

$$\|T'_m\|_{H^{-1}(\Omega)} \leq C(\|f\|_{L^2(\Omega)} + \|T_m\|_{H^1(\Omega)}), \tag{6.56}$$

and therefore

$$\int_0^{t_{final}} \|T'_m\|^2_{H^{-1}(\Omega)} dt \leq C \int_0^{t_{final}} (\|f\|^2_{L^2(\Omega)} + \|T_m\|^2_{H^1(\Omega)}) dt \leq C\Big(\|T_0\|^2_{L^2(\Omega)} + \|f\|^2_{L^2(S;L^2(\Omega))}\Big). \tag{6.57}$$

□

The sequence $\{T_m\}_{m=1}^\infty$ is bounded in $L^2(S; H^1(\Omega))$ and $\{T'_m\}_{m=1}^\infty$ is bounded in $L^2(S; H^{-1}(\Omega))$, so it exists a subsequence $\{T_{m_l}\}_{l=1}^\infty \subset \{T_m\}_{m=1}^\infty$ and a function $T \in L^2(S; H^1(\Omega))$ with $T' \in L^2(S; H^{-1}(\Omega))$ such that

$$\begin{cases} T_{m_l} \longrightarrow T & \text{weakly in } L^2(S; H^1(\Omega)) \\ T'_{m_l} \longrightarrow T' & \text{weakly in } L^2(S; H^{-1}(\Omega)) \end{cases}. \tag{6.58}$$

**Step 3: Recovering of the weak formulation 6.42.** To prove now that the obtained limit function is actually the weak solution of our PDE, we fix an integer $N$ and choose a function $v \in C^1(S; H^1(\Omega))$ defined as

$$v(t) = \sum_{k=1}^N d^k(t) w_k, \tag{6.59}$$

where this time the coefficients $d_k(t)$ are given smooth functions. Choose then an integer $m \geq N$, multiply the Galerkin system of equations (6.46) by $d^k(t)$ and sum over $k = 1, \dots, m$. What we get is

$$\rho c_p (T'_m, v) + k(\nabla T_m, \nabla v) - (h T_m, v)_{L^2(\Gamma_R)} - \alpha (T_m, v) = (f, v). \tag{6.60}$$

Integrating over time and setting $m = m_l$ we find the weak limit for $l \longrightarrow \infty$

$$\int_0^{t_{final}} \rho c_p (T', v) + k(\nabla T, \nabla v) - h(T, v) - \alpha (T, v) = \int_0^{t_{final}} (f, v). \tag{6.61}$$

Since this is true for any $v \in L^2(0, t_{final}; H^1(\Omega))$ because the piecewise linear function defined in (6.59) are dense in this space, we can conclude that also the following equality holds

$$\rho c_p(T', v) + k(\nabla T, \nabla v) - h(T, v) - \alpha(T, v) = (f, v) \tag{6.62}$$

for almost every $t \in S$ and for each $v \in H^1(\Omega)$. Having proved that this is a solution to the PDE, it remains to show that also the initial condition is satisfied, $T(x, 0) = T_0(x),\ x \in \Omega$.

$$\begin{aligned}\int_0^{t_{final}} \langle T', v\rangle dt &= \int_0^{t_{final}} dt - \langle T, v'\rangle + \int_0^{t_{final}} \frac{d}{dt}\langle T, v\rangle dt = \\ &= \int_0^{t_{final}} -\langle T, v'\rangle dt + \Big((T(t_{final}), v(t_{final})) - (T(0), v(0))\Big) = \\ &= \int_0^{t_{final}} -\langle T, v'\rangle dt - (T(0), v(0))\end{aligned}$$

having assumed $v(t_{final}) = 0$.
Plugging this result in equation (6.61), we have

$$\int_0^{t_{final}} \Big( - \rho c_p \langle T, v'\rangle + k(\nabla T, \nabla v) - h(T, v) - \alpha(T, v)\Big) dt = \int_0^{t_{final}} (f, v) dt + (T(0), v(0)) \tag{6.63}$$

and this is true for any $v \in C^1(S; H^1(\Omega))$ with $v(t_{final}) = 0$.
In addition, if this is valid for $T$, then it is valid also for $T_m$ for any $m$; setting $m = m_l$ and passing to the limit we get then

$$T_{m_l}(0) \longrightarrow T_0 \text{ in } L^2(\Omega). \tag{6.64}$$

So that we find $T(0) = T_0$.

**Step 4: Uniqueness of solution.** To prove the uniqueness of the solution of the weak formulation, we assume that two different solutions $T_1$ and $T_2$ exist, satisfying the same initial and boundary data. Define $\zeta = T_1 - T_2$, it is solution of (6.39) with zero right hand side:

$$\begin{cases} \rho c_p \partial_t \zeta - k \cdot div(\nabla \zeta) - \alpha \zeta = 0 & \Omega \times S \\ -k \nabla \zeta \cdot n = 0 & \Gamma_N \times S \\ \zeta = 0 & \Gamma_D \times S \\ -k \nabla \zeta \cdot n = h\zeta & \Gamma_R \times S \\ \zeta(0, x) = 0 & \Omega \times (t = 0) \end{cases} . \tag{6.65}$$

Taking as test function $\varphi = \zeta$ gives

$$\begin{aligned} \rho c_p \frac{d}{dt}\Big(\frac{1}{2}\|\zeta\|^2_{L^2(\Omega)}\Big) + k(\zeta, \zeta)_{L^2(\Gamma_R)} + k(\nabla\zeta, \nabla\zeta)_{L^2(\Omega)} - \alpha(\zeta, \zeta)_{L^2(\Omega)} = 0 \\ \rho c_p \frac{d}{dt}\Big(\frac{1}{2}\|\zeta\|^2_{L^2(\Omega)}\Big) + k\|\zeta\|^2_{L^2(\Gamma_R)} + k\|\nabla\zeta\|^2_{L^2(\Omega)} - \alpha\|\zeta\|^2_{L^2(\Omega)} = 0. \end{aligned} \tag{6.66}$$

Using the inequalities obtained in the derivation of the energy estimate, we similarly get

$$\frac{d}{dt}(\|\zeta\|^2_{L^2(\Omega)}) + C_0\|\zeta\|^2_{H^1(\Omega)} \leq C_1\|\zeta\|^2_{L^2(\Omega)}. \tag{6.67}$$

Gronwall's inequality (6.51) yields the conclusion $\zeta = 0$. □

## 6.4 Continuity with respect to data and parameters for the linear case

In this section we conclude the proof of the well posedness for the linear case by showing that the weak solution depends continuously on data and parameters.

*Remark.* Note that the proof of the continuity of the solution on the data is a stronger result, which directly implies the uniqueness of the weak solution proved in the previous Section.

Let $T^{(1)}$ and $T^{(2)}$ be two weak solutions to Problem 1 in the sense of Definition 6.3.1. They correspond respectively to the parameters and initial/boundary data

$$\begin{aligned}(\rho^{(1)}, c_p^{(1)}, k^{(1)}, \alpha^{(1)}, f^{(1)}, T_D^{(1)}, h^{(1)}, T_0^{(1)}) &\longrightarrow T^{(1)}\\ (\rho^{(2)}, c_p^{(2)}, k^{(2)}, \alpha^{(2)}, f^{(2)}, T_D^{(2)}, h^{(2)}, T_0^{(2)}) &\longrightarrow T^{(2)}.\end{aligned} \tag{6.68}$$

In the following the numbers between brackets (1) and (2) refer to the corresponding sets of parameters, initial and boundary data and solution. We want to estimate the perturbation on the temperature profile $T^{(2)} = T^{(1)} + \delta$ consequence of a perturbation on the parameters and initial/boundary conditions.
For simplicity of notation, we use $\mathfrak{D}$ to denote the difference between the corresponding values in (6.68). Set thus $\mathfrak{D}(\rho) := \rho^{(2)} - \rho^{(1)}, \mathfrak{D}(k) := k^{(2)} - k^{(1)}, \mathfrak{D}(\alpha) := \alpha^{(2)} - \alpha^{(1)}, \mathfrak{D}(f) := f^{(2)} - f^{(1)}, \mathfrak{D}(T_D) := T_D^{(2)} - T_D^{(1)}, \mathfrak{D}(h) := h^{(2)} - h^{(1)}$ and $\mathfrak{D}(T_0) := T_0^{(2)} - T_0^{(1)}$.

**Theorem 6.4.1.** *Let $T^{(1)}$ and $T^{(2)}$ be two weak solutions of Problem 1. Then, there exists a positive constant $C$ such that*

$$\|\mathfrak{D}(T)\|^2_{L^2(S;H^1(\Omega))} \leq C\Big(\|\mathfrak{D}(T_0)\|^2_{L^2(\Omega)} + \|\mathfrak{D}(f)\|^2_{L^2(\Omega)} + \|\mathfrak{D}(\rho c_p)\|^2_{L^\infty(\Omega)} + \|\mathfrak{D}(h))\|^2_{L^\infty(\Omega)} + \|(\mathfrak{D}(k)\|^2_{L^\infty(\Omega)}\Big). \tag{6.69}$$

*Proof.* We derive the weak formulations and we subtract the weak formulation of the set (1) from the weak formulation of the set (2):

$$\begin{aligned}&(\rho^{(2)}c_p^{(2)}\partial_t T^{(2)} - \rho^{(1)}c_p^{(1)}\partial_t T^{(1)}, \varphi)_{L^2(\Omega)} - (h^{(2)}T^{(2)} - h^{(1)}T^{(1)}, \varphi)_{L^2(\Gamma_R)} +\\ &+ (k^{(2)}\nabla T^{(2)} - k^{(1)}\nabla T^{(1)}, \nabla\varphi)_{L^2(\Omega)} - (\alpha^{(2)}T^{(2)} - \alpha^{(1)}T^{(1)}, \varphi)_{L^2(\Omega)} = (f^{(2)} - f^{(1)}, \varphi)_{L^2(\Omega)}.\end{aligned} \tag{6.70}$$

By adding and subtracting the needed terms, we rewrite

$$\begin{aligned}(\rho^{(2)}c_p^{(2)}(\partial_t T^{(2)} - \partial_t T^{(1)}), \varphi)_{L^2(\Omega)} &+ (k^{(2)}(\nabla T^{(2)} - \nabla T^{(1)}), \nabla\varphi)_{L^2(\Omega)} =\\ &= (h^{(2)}(T^{(2)} - T^{(1)}), \varphi)_{L^2(\Gamma_R)} + (\alpha^{(2)}(T^{(2)} - T^{(1)}), \varphi)_{L^2(\Omega)} +\\ &+ (f^{(2)} - f^{(1)}, \varphi)_{L^2(\Omega)} + ((\rho^{(2)}c_p^{(2)} - \rho^{(1)}c_p^{(1)})\partial_t T^{(1)}, \varphi)_{L^2(\Omega)} +\\ &+ ((h^{(2)} - h^{(1)})T^{(1)}, \varphi)_{L^2(\Gamma_R)} - ((k^{(2)} - k^{(1)})\nabla T^{(1)}, \nabla\varphi)_{L^2(\Omega)} +\\ &+ ((\alpha^{(2)} - \alpha^{(1)})T^{(1)}, \varphi)_{L^2(\Omega)}.\end{aligned} \tag{6.71}$$

We choose now the test function to be $\varphi = T^{(2)} - T^{(1)}$ to obtain

$$\frac{1}{2}\min(\rho^{(2)}c_p^{(2)})\frac{d}{dt}\|T^{(2)} - T^{(1)}\|^2_{L^2(\Omega)} + \min(k^{(2)})\|\nabla(T^{(2)} - T^{(1)})\|^2_{L^2(\Omega)} \leq \sum_k |I_k|, \tag{6.72}$$

where the right hand side of (6.72) is the sum of the integrals $I_k$ defined by

$$
\begin{aligned}
|I_1| &= |(h^{(2)}(T^{(2)}-T^{(1)}),\varphi)_{L^2(\Gamma_R)}| \le \max(h^{(2)})\|T^{(2)}-T^{(1)}\|^2_{L^2(\Gamma_R)} \le \\
&\le C_{\Gamma_R}\max(h^{(2)})\|\nabla(\mathfrak{D}(T))\|^2_{L^2(\Omega)} \\
|I_2| &= |(\alpha^{(2)}(T^{(2)}-T^{(1)}),\varphi)_{L^2(\Omega)}| \le \max(\alpha^{(2)})\|\mathfrak{D}(T)\|^2_{L^2(\Omega)} \\
|I_3| &= |(f^{(2)}-f^{(1)},\varphi)_{L^2(\Omega)}| \le \frac{1}{2}\|\mathfrak{D}(f)\|^2_{L^2(\Omega)} + \frac{1}{2}\|\mathfrak{D}(T)\|^2_{L^2(\Omega)} \\
|I_4| &= |((\rho^{(2)}c_p^{(2)}-\rho^{(1)}c_p^{(1)})\partial_t T^{(1)},\varphi)_{L^2(\Omega)}| \le \frac{1}{2}(\max(\mathfrak{D}(\rho c_p))^2\|\partial_t T^{(1)}\|^2_{L^2(\Omega)} + \frac{1}{2}\|\mathfrak{D}(T)\|^2_{L^2(\Omega)} \le \\
&\le \frac{1}{2}C_e(\max\mathfrak{D}(\rho c_p))^2 + \frac{1}{2}\|\mathfrak{D}(T)\|^2_{L^2(\Omega)} \\
|I_5| &= |((h^{(2)}-h^{(1)})T^{(1)},\varphi)_{L^2(\Omega)}| \le \frac{1}{2}C_e(\max(\mathfrak{D}(h)))^2 + \frac{1}{2}\|\mathfrak{D}(T)\|^2_{L^2(\Omega)} \\
|I_6| &= |((k^{(2)}-k^{(1)})\nabla T^{(1)},\nabla\varphi)| \le \frac{1}{2\varepsilon}(\max(\mathfrak{D}(k))^2\|\nabla T^{(1)}\|^2 + \frac{\varepsilon}{2}\|\nabla\mathfrak{D}(T)\|^2_{L^2(\Omega)} \\
&\le C_e\frac{1}{2\varepsilon}(\max(\mathfrak{D}(k))^2 + \frac{\varepsilon}{2}\|\nabla\mathfrak{D}(T)\|^2_{L^2(\Omega)} \\
|I_7| &= |((\alpha^{(2)}-\alpha^{(1)})T^{(1)},\varphi)_{L^2(\Omega)}| \le \max(\mathfrak{D}(\alpha))\|T^{(1)}\|_{L^2(\Omega)}\cdot\|\mathfrak{D}(T))\|_{L^2(\Omega)} \le \\
&\le \frac{1}{2}(\max(\mathfrak{D}(\alpha)))^2\|T^{(1)}\|^2_{L^2(\Omega)} + \frac{1}{2}\|\mathfrak{D}(T))\|^2_{L^2(\Omega)} \le \frac{1}{2}C_e\max(\mathfrak{D}(\alpha))^2 + \frac{1}{2}\|\mathfrak{D}(T)\|^2_{L^2(\Omega)}
\end{aligned}
$$

where in $I_6$ we use the Young inequality to make the gradient of the difference of temperature as small as possible choosing $\varepsilon \in (0,1)$. Thus we get

$$
\begin{aligned}
\frac{1}{2}\min(\rho^{(2)}c_p^{(2)})\frac{d}{dt}\|\mathfrak{D}(T)\|^2_{L^2(\Omega)} + (\min(k^{(2)}) - C_{\Gamma_R}\max(h^{(2)}) - \frac{\varepsilon}{2})\|\nabla\mathfrak{D}(T)\|^2_{L^2(\Omega)} \le \\
\le (\max(\alpha^{(2)})+2)\|\mathfrak{D}(T)\|^2_{L^2(\Omega)} + \frac{1}{2}\|\mathfrak{D}(f)\|^2_{L^2(\Omega)} + \frac{1}{2}C_e(\|\mathfrak{D}(\rho c_p)\|^2_{L^\infty(\Omega)} + \\
+ \frac{1}{2}C_e\|\mathfrak{D}(h)\|^2_{L^\infty(\Omega)} + \frac{C_e}{2\varepsilon}\|\mathfrak{D}(k)\|^2_{L^\infty(\Omega)} + \frac{1}{2}C_e\|\mathfrak{D}(\alpha)\|^2_{L^\infty(\Omega)}.
\end{aligned} \tag{6.73}
$$

We assume now

$$
\min(k^{(2)}) - C_{\Gamma_R}\max(h^{(2)}) - \frac{\varepsilon}{2} > 0 \tag{6.74}
$$

and recall that $\|\nabla(\mathfrak{D}(T))\|^2_{L^2(\Omega)} \le C_P\|(\mathfrak{D}(T))\|^2_{H^1(\Omega)}$ for a positive constant $C_P$. Thus, we find an inequality of the form of (6.49)

$$
\begin{aligned}
\frac{d}{dt}\|\mathfrak{D}(T)\|^2_{L^2(\Omega)} + C_0\|\mathfrak{D}(T)\|^2_{H^1(\Omega)} \le C_1\|\mathfrak{D}(T)\|^2_{L^2(\Omega)} + \\
+ C_2\Big(\|\mathfrak{D}(f)\|^2_{L^2(\Omega)} + \|\mathfrak{D}(\rho c_p)\|^2_{L^\infty(\Omega)} + \|\mathfrak{D}(h))\|^2_{L^\infty(\Omega)} + \|(\mathfrak{D}(k)\|^2_{L^\infty(\Omega)}\Big)
\end{aligned} \tag{6.75}
$$

Thus, we can apply again Gronwall's inequality in the integral form to get

$$
\|\mathfrak{D}(T)\|^2_{L^2(S;H^1(\Omega))} \le C\Big(\|\mathfrak{D}(T_0)\|^2_{L^2(\Omega)} + \|\mathfrak{D}(f)\|^2_{L^2(\Omega)} + \|\mathfrak{D}(\rho c_p)\|^2_{L^\infty(\Omega)} + \|\mathfrak{D}(h))\|^2_{L^\infty(\Omega)} + \|(\mathfrak{D}(k)\|^2_{L^\infty(\Omega)}\Big). \tag{6.76}
$$

□

## 6.5 Existence for a non-linear case

*Remark.* When the only coefficient of diffusion $k$ is non linear i.e. $k = k(T)$, it is enough to assume

(H6.b) $k \in C(\mathbb{R})$, $k_1 \le k(\zeta) \le k_2$ for all $\zeta \in \mathbb{R}$ with $k_i \quad (i = 1, 2)$ positive constants.

to get to the existence of the weak solution in the sense of the Definition 6.3.1.
We can repeat the first three steps of the proof of Theorem 6.5.1 just adapting the inequality for the energy estimate in Lemma 6.3.3 to be

$$(c) \quad \int_\Omega k(T_m)\nabla T_m \nabla T_m \geq \frac{k_1}{1+c_p^2}\|T_m\|^2_{H^1(\Omega)} \tag{6.77}$$

And the conclusion follows applying Gronwall's inequality.

### 6.5.1 Non-linear diffusion coefficient and source term

In this section we are concerned with the study of the non-linearities occurring in the heat diffusion equations, focusing especially on the non linear conduction coefficient $k = k(T)$ and on the source term $f = f(T)$. Here source term is assumed to satisfy the following conditions

(H7) $f \in C(\mathbb{R})$, with the bounds

$$\begin{aligned} &|f(\zeta)| \leq C_1\Big(1+|\zeta|^{1+4/n}\Big) \quad \text{for all } \zeta \in \mathbb{R}, \quad C_1 > 0 \text{ constant}, \\ &f(\zeta)\zeta \geq -C_2(1+\zeta^2) \quad \text{for all } \zeta \in \mathbb{R}, \quad C_2 > 0 \text{ constant}. \end{aligned} \tag{6.78}$$

The problem can be stated as:

**Problem 2.** *Find $T(x,t)$ with $x \in \Omega$ and $t \in S$ satisfying*

$$\begin{cases} \rho c_p \partial_t T + div(-k(T)\nabla T) = \alpha T + f(T) & \Omega \times S \\ -k(T)\nabla T \cdot n = 0 & \Gamma_N \times S \\ T = 0 & \Gamma_D \times S \\ -k(T)\nabla T \cdot n = hT & \Gamma_R \times S \\ T(0,x) = T_0 - T_D & \Omega \times (t=0) \end{cases} .$$

Having already homogenized the boundary date with respect to the Dirichlet boundary conditions.
Existence and uniqueness of weak solutions to Problem 2 are proven through the following result.

**Theorem 6.5.1.** *Assume (H1)-(H5) are fulfilled and additionally (H6.b) and (H7) hold. Then there exists a function $T \in L^2(S;H^1(\Omega)) \cap C(S;L^2(\Omega))$ with $T' \in L^2(S;H^{-1}(\Omega))$ weak solution in the sense of definition (6.3.1) to Problem 2 for every $t \in S$.*

*Proof.* The proof follows the steps done while proving Theorem 6.3.1.

**Step 1: Galerkin discretization.** We consider the problem in the projection space $H^1(\Omega_m)$ with $m$ fixed positive finite number, and from the theory of differential equations we prove the existence and uniqueness of the solution $T_m \in L^2(S;H^1_D(\Omega_m))$ to the Galerkin system of equations

$$\rho c_p d_j'(t) - h d_j(t) + \sum_{k=1}^{m} k(T_m) d_k(t)(\nabla w_k, \nabla w_j) - \alpha d_j(t) = f_j \qquad \text{for all } j = 1,\dots,m. \tag{6.79}$$

A priori estimates can be found analogously to the proof of Lemma 6.3.3:

**Lemma 6.5.2.** (Energy estimate) There exists a constant $C$, depending only on $\Omega$, $t_{final}$ and the coefficients of the parabolic operator, such that

$$\max_{0\leq t\leq t_{final}} \|T_m\|^2_{L^2(\Omega)} + \|T_m\|^2_{L^2(S;H^1(\Omega))} + \|T_m'\|^2_{L^2(S;H^{-1}(\Omega))} \leq C\Big(\|T_0\|^2_{L^2(\Omega)} + \|f\|^2_{L^2(S;L^2(\Omega))}\Big) \tag{6.80}$$

*Proof.* We choose the test function to be the solution to the projection problem and integrate over $(0,t)$ with $t \in S$. We follow the steps in the proof of Lemma 6.3.3 with the two new inequalities

$$(c) \qquad \int_\Omega k(T_m)\nabla T_m \nabla T_m \geq \frac{k_1}{1+c_p^2}\|T_m\|^2_{H^1(\Omega)},$$
$$(e) \qquad |(f,T_m)| \leq \int_\Omega \frac{1}{2}|f|^2 + \int_\Omega \frac{1}{2}|T_m|^2 = \frac{1}{2}||f||^2_{L^2(\Omega)} + \frac{1}{2}||T_m||^2_{L^2(\Omega)},$$

to find (6.80). □

**Step 2: Passing to the limit $m \longrightarrow \infty$.** From Lemma 6.5.2 we conclude (by going to a subsequence) that when $m \longrightarrow \infty$

$$\begin{cases} T_m \longrightarrow T \text{ in } L^2(S;H^1(\Omega)) \\ T_m' \longrightarrow T' \text{ in } L^2(S;H^{-1}(\Omega)) \end{cases} \tag{6.81}$$

**Step 3: Recovering of the weak formulation 6.42.** Let now $N$ be an arbitrary integer, $\beta_j$, $j = 1,\dots,N$ be arbitrary reals and $\varphi = \varphi(t)$ test function depending only on time. From the weak formulation we can infer that

$$\begin{aligned} &-\rho c_p \int_0^{t_{final}} \Big(T_m, \varphi' \sum_{j=1}^N \beta_j w_j\Big)dt + \int_0^{t_{final}} \int_\Omega k(T_m)\nabla T_m \cdot \nabla\Big(\varphi \sum_{j=1}^N \beta_j w_j\Big)dxdt + \\ &- \int_0^{t_{final}} \int_{\Gamma_R} hT_m\Big(\varphi \sum_{j=1}^N \beta_j w_j\Big)dsdt - \alpha \int_0^{t_{final}} \int_\Omega T_m\Big(\varphi \sum_{j=1}^N \beta_j w_j\Big)dxdt = \\ &= \int_0^{t_{final}} \int_\Omega f(T_m)\Big(\varphi \sum_{j=1}^N \beta_j w_j\Big)dxdt, \end{aligned} \tag{6.82}$$

for any $m$ greater than $N$. We look at the term on the right hand side. Set

$$s = \frac{n}{n+2}, \qquad q = \frac{2(n+2)}{n+4}. \tag{6.83}$$

Then, $q > 1$ and

$$q' = \frac{q}{q-1} \leq \frac{2n}{n-2} \quad \text{if} n > 2. \quad \frac{2sn}{n-2s} = 2. \tag{6.84}$$

We can then write

$$\int_\Omega |T_m(t)|^{(1+4/n)q}dx = \|T_m(t)\|^{2n/n-2s}_{L^{2n/n-2s}(\Omega)} \leq C\|T_m(t)\|^{2sn/n-2s}_{H^1(\Omega)}\|T_m(t)\|^{2(1-s)n/n-2s}_{L^2(\Omega)} \tag{6.85}$$

for all $t \in S$ and $m = 1,2,\dots$. Here $C$ is a positive constant.

We can thus state

$$\int_0^{t_{final}} \int_\Omega |f(T_m)|^q dxdt \leq c\|T_m\|^2_{L^2(S;H^1(\Omega))} \leq C, \tag{6.86}$$

where the last inequality is direct consequence of the energy estimate. Together with hypothesis (H6.c)

$$\lim_{m\longrightarrow\infty} \int_0^{t_{final}} \int_\Omega f(T_m)\varphi \sum_{j=1}^N \beta_j w_j dxdt = \int_0^{t_{final}} \int_\Omega f(T)\varphi \sum_{j=1}^N \beta_j w_j dxdt. \tag{6.87}$$

Further, $k(T_m) \longrightarrow k(T)$ since $k$ is continuous and $T_m$ is uniformly bounded. Hence, by letting $m \longrightarrow \infty$ in Equation (6.82), we get

$$\begin{aligned}
&-\rho c_p \int_0^{t_{final}} \Big(T, \varphi' \sum_{j=1}^{N} \beta_j w_j\Big) dt + \int_0^{t_{final}} \int_\Omega k(T) \nabla T \cdot \nabla \Big(\varphi \sum_{j=1}^{N} \beta_j w_j\Big) dx dt + \\
&- \int_0^{t_{final}} \int_{\Gamma_R} hT \Big(\varphi \sum_{j=1}^{N} \beta_j w_j\Big) ds dt - \alpha \int_0^{t_{final}} \int_\Omega T \Big(\varphi \sum_{j=1}^{N} \beta_j w_j\Big) dx dt = \\
&= \int_0^{t_{final}} \int_\Omega f(T) \Big(\varphi \sum_{j=1}^{N} \beta_j w_j\Big) dx dt.
\end{aligned} \tag{6.88}$$

A standard argument implies the existence of $T' \in L^2(S; H^{-1}(\Omega))$ so that for almost all $t$ in $S$ and any $w_i$ in $H^1(\Omega)$

$$\langle T'(t), w_j \rangle + \int_\Omega k(T(t)) \nabla T(t) \cdot \nabla w_j dx - \int_{\Gamma_R} hT w_j - \alpha \int_\Omega T w_j = \int_\Omega f(T) w_j. \tag{6.89}$$

Finally, integration by parts yields $T(0) = T_0$ and indeed, $T$ is the weak solution to our problem. □

## 6.6 Uniqueness for a non linear case

To study the uniqueness of the solution found in Section 6.5, we further simplify the formulation and consider the class of equations

$$\partial_t u + div(-k(u) \nabla u) = f, \tag{6.90}$$

with homogeneous and/or Neumann boundary conditions and positive $k$.
Thus we assume the following hypotheses to be fulfilled

(H8.a) $k$ is a strictly positive function of the temperature, $k > 0$;

(H8.b) $\alpha = 0$, $h = 0$.

*Remark.* To get $\rho c_p = 1$, it is sufficient to rescale the problem without making any additional assumption. Also, the homogeneous Dirichlet boundary conditions are obtained by introducing a new temperature $\tilde{T} = T - T_0$ as done in Section 6.3.

The new problem under the assumptions (H1)-(H5) and (H8) is thus stated as follows:

**Problem 3.** *Find $T(x,t)$ with $x \in \Omega$ and $t \in S$ satisfying*

$$\begin{cases} \partial_t T + div(-k(T) \nabla T) = f & \Omega \times S \\ -k(T) \nabla T \cdot n = 0 & (\Gamma_N \cup \Gamma_R) \times S \\ T = 0 & \Gamma_D \times S \end{cases} \tag{6.91}$$

In this case, we can prove the uniqueness of the solution through this main result.

**Theorem 6.6.1.** *Assume (H1)-(H5) are fulfilled and additionally (H6.b) and (H8) hold. Then it is unique the weak solution $T \in L^2(S; H^1(\Omega)) \cap C(S; L^2(\Omega))$ with $T' \in L^2(S; H^{-1}(\Omega))$ in the sense of definition (6.3.1) to Problem 3 for almost all $t \in S$.*

*Proof.* To prove the uniqueness of the weak solution to Problem 3 we use an auxiliary formulation. We introduce the Kirchoff's transform

$$b(T) = \int_0^T k(y) dy \tag{6.92}$$

to map Equation (6.91) in

$$\partial_t \beta(T) - \Delta T = f. \tag{6.93}$$

Here $\beta$ is the inverse of the Kirchoff's transform, which exists because $b(u)$ is strictly increasing

$$\beta \coloneqq b^{-1}. \tag{6.94}$$

Thus, if we can prove the uniqueness of the solution to (6.93), we directly get the uniqueness of the solution to Problem 3.
We assume two weak solutions $T_1$ and $T_2$ to (6.93) exist and after deriving the weak formulations, we subtract the second to the first

$$(\partial_t \beta(T_1) - \partial_t \beta(T_2), \varphi) + (\nabla(T_1 - T_2), \nabla\varphi) = 0 \tag{6.95}$$

for any test function $\varphi \in H^1_D$. Consider now the following auxiliary problem:

**Problem 4.** *Find $G$ such that*

$$\begin{cases} -\Delta G = \beta(T_1) - \beta(T_2) \\ G = 0 \quad \Gamma_D \\ \nabla G \cdot n = 0 \quad \Gamma_n \cup \Gamma_R \end{cases} \tag{6.96}$$

The weak formulation associated with (6.96) is

$$(\nabla G, \nabla\psi) = (\beta(T_1) - \beta(T_2), \psi) \tag{6.97}$$

for every $\psi \in H^1_D(\Omega)$. Differentiate now (6.96) with respect to time. Commuting the time and space derivatives of $G$, we get

$$-\Delta(\partial_t G) = \partial_t(\beta(T_1) - \beta(T_2)). \tag{6.98}$$

The corresponding weak formulation with test function $\psi = G$ is thus

$$(\nabla\partial_t G, \nabla G) = (\partial_t(\beta(T_1) - \beta(T_2)), G) \tag{6.99}$$

and gives

$$\frac{1}{2}\frac{d}{dt}|\nabla G|^2 = (\partial_t(\beta(T_1) - \beta(T_2), G). \tag{6.100}$$

Integrating now (6.100) over time we obtain

$$\frac{1}{2}|\nabla G(t)|^2 - \frac{1}{2}|\nabla G(0)|^2 = \int_0^t (\partial_t(\beta(T_1) - \beta(T_2)), G) ds. \tag{6.101}$$

Since $G$ is the solution to the Laplace equation with homogeneous boundary conditions, we can deduce $|\nabla G(0)|^2 = 0$. In this case, the right hand side of (6.101) must be non negative

$$\int_0^t (\partial_t(\beta(T_1) - \beta(T_2)), G) ds \geq 0. \tag{6.102}$$

Hence, for almost every $t \in S$,

$$(\partial_t(\beta(T_1) - \beta(T_2)), G) \geq 0. \tag{6.103}$$

Choose now the test function in (6.95) to be $\varphi = G$. We have

$$(\partial_t \beta(T_1) - \partial_t \beta(T_2), G) + (\nabla(T_1 - T_2), \nabla G) = 0. \tag{6.104}$$

On the other hand, we choose $\psi = T_1 - T_2$ in (6.97) to get

$$(\nabla G, \nabla(T_1 - T_2)) = (\beta(T_1) - \beta(T_2), T_1 - T_2). \tag{6.105}$$

Thus, comparing the expressions (6.104) and (6.105) we derive

$$(\partial_t \beta(T_1) - \partial_t \beta(T_2), G) + (\beta(T_1) - \beta(T_2), T_1 - T_2) = 0. \tag{6.106}$$

Both terms in (6.106) are non negative. The first one because of the result (6.103), while the second one because of the monotonicity of the function $\beta$. By the fact that their sum must be zero we conclude that they both are null. Especially,

$$(\beta(T_1) - \beta(T_2), T_1 - T_2) = 0 \tag{6.107}$$

and the monotonicity of the function $\beta$ forces

$$T_1 = T_2 \tag{6.108}$$

for almost every $t \in S$ and $x \in \Omega$. This concludes our proof. □

## 6.7 Continuity with respect to data and parameters for a non linear case

*Remark.* The proof of the continuity of the solution with respect to parameters and initial/boundary values proposed in Section 6.4 can be repeated for the non linear case. However, the non linearity in the diffusion coefficient brings a significant increase in the complexity of the treatment, as shown in the proof of the uniqueness in a non-linear case (see Section 6.6). Because of the time narrowness we are forced to take decision about where to direct our study. For application purposes, we prefer to skip this section and focus on the inverse problem.

## 6.8 Identification of the parameters in the governing equations

For practical purposes, inverse problems in the analysis of photothermolysis are unavoidable. In fact, the coefficients can not be directly measured and the specificity makes the availability of the parameter values quite scarce in literature. On the other hand, the measurement of the temperature variation is difficult, it costs and has obtrusiveness limitation. An identification method to detect parameters would be an appreciable achievement towards the understanding of the thermal response of the light-irradiated tissue and in new achievements in clinical studies.

Thus our question becomes: *Can we estimate the parameters involved in the heat diffusion equation, by purely macroscopic measurements, i.e. having only information on parts of the domain $\Omega$, or even only on part of its boundary $\Gamma$?*
Assume we can measure the temperature $T_p(x) \in L^2(\Omega')$ at fixed time $t_{fix}$ on a subset $\Omega' \subset \Omega$ of positive measure.

We call $\Lambda \subset [L^2(\Omega)]^5$ the set of admissible parameters $\rho$, $c_p$, $k$, $\alpha$ and $h$ with elements $\lambda := (\rho,\ c_p,\ k,\ \alpha,\ h) \in \Lambda$. Then $\lambda$ is assumed to satisfy the following hypotheses:

(H9) $\lambda \in [C^p(\bar{\Omega})]^5$ with $p > 0$;

(H10) $\lambda \geq c_m$ with $c_m > 0$;

(H11) $\|\lambda\|_{[C^p(\bar{\Omega})]^5} \leq c_M$ with $c_M > 0$.

Further, the parameter space $\Lambda$ is assumed to be convex and closed in $[L^2(\Omega)]^5$. Let $T(t, x; \lambda)$ be the unique solution corresponding to the data $\lambda \in \Lambda$. Following [27], we propose a straight-forward least-squares approach consisting of finding the optimum parameters combination

$$\lambda^* := \arg\min_{\lambda \in \Lambda} \|T(t_{fix}, \cdot; \lambda) - T_p(\cdot)\|. \tag{6.109}$$

**Theorem 6.8.1.** *Under the regularity assumptions done in the previous sections (H1)-(H5), together with (H9)-(H11) for problem 1, an optimal $\lambda^*$ solving (6.109) exists.*

*Proof.* From the hypotheses (H9)-(H11), the subset $\Lambda$ is convex, bounded and closed. The operator mapping the parameters in the solution

$$F \ : \ \lambda \longrightarrow T \tag{6.110}$$

is weakly sequentially continuous; it follows that also the functional in (6.109) is weakly sequentially continuous and therefore takes a minimum in $\Lambda$. □

*Remark.* Note that even having the existence quite easily from the well posedness of the problem, the proof of the uniqueness of the identified parameters requires a deeper study, specific for the treated case. For example, in [28], the treated inverse problem consists of determining the unknown coefficient of diffusion in a non-linear parabolic problem. The authors show that the inverse problem admits a unique solution in the class of admissible coefficients - the proof uses the Kirchoff's transform (6.92) introduced earlier. Also [29] deals with the identification of the unknown diffusion coefficient in a non-linear diffusion equation. This case applies especially to the physical problem treated in this manuscript because gets as input overspecified data measured at the boundary. From a practical point of view, this measurement is the easiest and non obtrusive. [29] derives a uniqueness result for the inverse problem with this input.

## 6.9 Conclusion

In this Chapter we investigated the system of equations governing the heat transfer inside the tissue after the light energy is delivered by the photoepilation device. First we derive the equations, initial and boundary conditions from the physical problem. We use the bioheat equations (see [14]) because they model the reaction of the skin to the thermal stimulation.

Through the dimensional analysis we get an insight in the role played by the physical processes taking place during the light-based treatment.

The negligibility of the perfusion term, expected from the literature investigation, is confirmed and is due to the different time scales of the processes. The treatment lasts for less than 50 milliseconds and heat diffuses for a comparable time. On the other hand, the process of nourishment delivery by the blood is a slow process which does not affect the studied temperature variation.

The unexpected result is about the radiative term: although it is often neglected in biological studies, we show that during light-based treatment it is a relevant term because of the high temperatures reached. We avoid including this term in the rigorous analysis for the sake of simplicity. Nonetheless, we suggest to study this contribution since it might be useful in achieving better treatment outcomes. Even if it plays a marginal role not directly related to the hair damage, it could be used to create optimal treatment conditions. For example, insulating the treated skin, we could increase the overall temperature, consequently reducing the temperature gradient and the heat flux from the hair to the surrounding tissue.

Then, we set an adequate functional framework and with a rigorous mathematical approach, we deeply analyze the direct problem. We aim to use its well posedness to identify uncertain parameters, moving to the inverse problem. We prove the existence, uniqueness and continuous dependence on data for a linear case. The well posedness of the direct problem is shown to be sufficient to the parameter identification under suitable conditions. Pushed by the hypotheses of a phase transition (see Chapter 4), we move then to a quasi-linear parabolic equation. While the existence can be proven with some acceptable assumptions, the uniqueness and the dependence on data requires some further conditions. Some simple case is introduced and it can be generalized by future studies. We touch the inverse problem showing that indeed the parameters can be estimated. Not only in the diffusion coefficient but also for the heat source deriving from the light radiation (see for example [30, 31]) which is affected by a kind of uncertainty as shown by the Design of Experiment in Chapter 3.

The novel mathematical approach opens new opportunities in parameter identification, which can supply the lack in measurements and literature sources. For what we could no study, we give hints for further investigations, and we aim to follow up the work as well.

# Chapter 7

# Conclusion

In this manuscript, we investigate the whole photothermolysis process and implement both an optical and a thermal model. Then, coupling the two parts, we build a simulation platform which is used to estimate the temperature increase inside the skin-hair structure during the light-based treatment. Finally, we move to predictive analysis looking for a link between the simulation outputs and the clinical data. The investigated field is quite broad and the limited time forced us to choose selected topics to focus on. In conclusion of the work, we want to summarize the results and give suggestions for future researches.

In Chapter 3 we introduce the Monte Carlo method for light diffusion in biological tissues. We propose the results of a simulation showing the selectivity of the treatment based on the light properties. The model is first used to study the variability of the rate of absorbed light. We observe that the variation in the optical parameters affects significantly the outcome of the process. Thus we must try to homogenize the study as much as possible. In fact, the rate of absorbed energy is the term coupling the Monte Carlo platform to the model for the heat transfer in biological tissues. In addition, when considering the inverse problem, we need to know three out of the four optical parameters given the absorption map. Otherwise the ill-posedness may lead to multiple physical solutions. We consider a system of parabolic equations and we numerically solve it. Since high temperatures are reached, our guess is that some phase transitions might take place. This hypothesis is supported by evidence, since during the clinical trials it is sometimes observable smoke and smell at the external surface. The model introduced for the phase change partially improves the existing one and allows a better understanding of the physico/chemical processes taking place during light-based treatments. However, the implementation is limited to the simple case of temperature-dependent parameters and does not include yet the evaporation and the radiation terms at the external surface of the skin. Since these terms are shown to be significant contributions in the process of heat conduction by the dimensional analysis, we strongly advise further improvements on this side and we gather probed directions in the literature.

The most outstanding result is achieved in predictive analysis. We probe two different approaches, multiple linear regression and artificial neural networks, showing both high predictive power. With these methods, physical values derived from the temperature profile, such as the Arrhenius damage integral, together with the device settings and the clinical information, can forecast the efficacy of the treatment. Even more precise predictions might be obtained adding the non-measured values in the simulation platform: we use fixed radius, depth and inclination of the hair and fixed optical parameters too. In the case they can be estimated, the temperature profile inside the skin-hair structure would be more accurate leading to a possible better estimation of the probability of hair death. Also the derivation of the efficacy per treatment and the conversion of the qualitative variables could be improved. Furthermore, we suggest the optimization of the neural networks by investigating the best number of hidden layers, hidden neurons and the best activation function.

Last but not least, we introduce a novel mathematical approach which guarantees the identifiability of certain parameters for well-posed models. We prove the existence, uniqueness and

continuity on data and parameters of the weak solution to the linear case. Furthermore, we study the existence and uniqueness for the weak solution to a quasi-linear case, which is the governing equation when phase transitions are included. The uniqueness in the latter case requires some strong assumptions which could generalized by using different mathematical approaches. We strongly believe that the new investigation with the mathematical rigorousness is a useful approach in the understanding of the physical process. It can support the numerical solution and give alternative ways for estimating non-measurable coefficients in the governing equations. In fact, the well posedness of the direct problem is shown to be sufficient under some suitable condition to the identifiability of the parameters. Since the thermal properties of the tissue used in the governing equations are affected by some kind of uncertainty, as well as the heat source (as shown by the design of experiment in Chapter 3), this thus we intend to relax some hypotheses and aim to continue the work after the submission of this manuscript.

# List of Figures

# List of Tables

# Appendix A

# Glossary

- **Scattering**
  is the physical process for which the light is forced to deviate from a straight trajectory due to local non-uniformities in the medium through which it travels.

- **Mean free path**
  average distance treaded by a moving photon between successive collisions.

- **Fluorescence or quantum yield**
  ratio of the number of photons emitted to the number of those absorbed.

- **Wavelength** $\lambda$ [nm]
  is the spatial distance occurring between the wave's shape repetitions (peaks or zero crossing are considered as reference points).

- **Index of refraction** $n$
  ratio of speed of light in vacuum to phase velocity in medium

  $$n = \frac{c}{v}$$

  where $c$ is the speed of light in vacuum and $v$ is the velocity of light in the considered optical medium. It is dimensionless and describes how light propagates through that medium.

- **Coefficient of absorption** $\mu_a$ [$\mathrm{cm}^{-1}$]
  probability of photon absorption by the medium per unit (infinitesimal) path length; it determines how far into a material light of a particular wavelength can penetrate before it is absorbed. It strongly depends on the wavelength and obviously on the material. In biological tissues it originates from hemoglobin (both oxygenated and deoxygenated), melanin and water. Its inverse $\frac{1}{\mu_a}$ is called mean absorption length.

- **Scattering coefficient** $\mu_s$ [$\mathrm{cm}^{-1}$]
  When it encounters a scattering particle within a homogeneous medium, a photon moving in a direction $s$ is scattered into a new one $s'$. The new directions generally do not occur with equal probability and can be described by the differential scattering coefficient $d\mu(s, s')$. The integral over the all angles gives $\mu_s$ the total scattering coefficient

  $$\mu_s = \int_{4\pi} d\mu_s(s, s')ds'.$$

  Its inverse $\frac{1}{\mu_s}$ is the scattering mean free path.

- **Total attenuation coefficient or extinction coefficient** $\mu_t$ [$\text{cm}^{-1}$]

  probability of photon interaction with a medium per unit path length

  $$\mu_t = \mu_a + \mu_s$$

  the mean free path between two interaction events will then be defined as the reciprocal of the extinction coefficient.

- **Anisotropy factor** $g$
  is defined as the mean cosine of polar angles $\theta$, the angles between the incident $s$ and the scattered direction $s'$

  $$g = \int_{4\pi} p(\theta)\cos(\theta)ds'$$

  where $p(s, s') = \frac{1}{\mu_s} d\mu_s(s, s')$ is the scattering phase function. In the case of isotropic medium, $p$ is equal for all angles and $g$ will be equal to zero.

- **Exposure time** [$s$]
  in photothermolysis literature it is defined as the time interval in which the treatment is applied, i.e. the time the radiation power is transferred to the skin.

- **Energy density** [$\text{J/cm}^2$]
  it is also known as fluence and measures the amount of energy applied per unit area in Joules per square centimeter.

- **Irradiance** [$\text{W/cm}^2$]
  or power density is measured in Watt per square centimeter and is the time rate of energy delivery.

- **Persistent random walk** $S_t$, $t \in \mathbb{N}$ (see [32])
  A classical random walk $S_t$ is defined by

  $$S_t \coloneqq \sum_{n=0}^{t} X_n \tag{A.1}$$

  where the increments $\{X_n\}_{n\in\mathbb{N}}$ are one-order Markov-chain, a short memory is introduced in the dynamics of $(S_t)$. This so called *persistent* random walk is no longer Markovian and, under suitable conditions, the rescaled process converges towards the integrated telegraph noise (ITN) as the time-scale and space-scale parameters tend to zero.

# Appendix B

# Publishable results

The statistical platforms for the predictive analysis of treatment efficacy is already used in the department of Personal Care and Wellness at Philips. We are collecting the results of our studies in a paper which will be submitted. We propose here the abstract, avoiding other details because of confidentiality reasons.

# Predictive analysis for selective photothermolysis

M. Regis, M. Zeitouny, T. Verhoeven, N. Uzunbajakava

Philips Research, TU Eindhoven, TU Delft, Philips Research

**Abstract**

*This study focuses on the treatment for hair removal with light-based devices. In particular, we aim to model the process leading to the hair damage in order to predict the treatment efficacy.*
*Optical and thermal methods are used to calculate the temperature variation resulting from the interaction between light and tissue. Physical parameters such as the peak temperature and the Arrhenius damage integral are derived from the temperature profile estimated by the model. Then these values, together with the device settings and the clinical information, are used to forecast the treatment efficacy. We build two statistical platforms which allow the prediction. They are robust and estimate the outcome of the treatment with high accuracy: the correlation between the outcome of the model and the measured values has a correlation higher than 90%. This novel approach both validates the opto-thermal model and significantly improves its predictive power.*

# Appendix C

# Implemented codes

## C.1 Monte Carlo Modeling of photon transport - 3D model

Algorithm of Monte Carlo method for photon transport in biological tissues. It allows the simulation of a 3D geometry with a variable number of layers.

### Input data

It requires as input the number of photon packets which are used in the simulation, the optical properties and the depth of each layer and of the ambient medium.

```
N=1e7;
mua=[0 10 10];
mus=[0 90 90];
g=[0 0.75];
s0=0;
depth=[0.02];
n=[1 1 1];
```

### Photons as statistical packets

At any point the photons are described through their position, direction and weight. The direction and position are initialized at the launch ones while they are associated with initial unitary weight.

```
pos=zeros(N,3);
D=repmat([0,0,1],N,1);
W=ones(N,1);
nm=0;
Rsp=zeros(N,1);
boundaries=[s0,s0+cumsum(depth)];
Nt=length(depth);
s=zeros(N,1);
energy=0;
RF=0;
T=0;
```

### Monte Carlo method

We write a *Main* script for the Monte Carlo Method, recalling the auxiliary functions *CM* (Current Medium) to define the layer in which the photon currently lies, *Dist* (Distance) to compute the distance from the boundaries according to the set direction, *PT* (Photon Transport) following the

photon path inside the tissue. *Rfl* (Reflection) to compute the probability of reflection and *Scatt* (Scattering) to define the scattering direction.

```
[cm,W,energy]=CM(N,W,pos,Nt,boundaries,energy);
Spr=(n(cm)~=n(cm+1));
if sum(Spr)~=0
    Rsp(Spr)=(n(cm(Spr))-n(cm(Spr)+1)).^2./(n(cm(Spr))+n(cm(Spr)+1)).^2;
    W(Spr)=1-Rsp(Spr);
end
jj=1;
while sum(W)>1e-3
    nm=nm+1;
    [cm,W,energy]=CM(N,W,pos,Nt,boundaries,energy);
    [pos,W,D,s,energy,RF,T]=PT(N,W,D,boundaries,s,mua,mus,pos,cm,energy,RF,Nt,
                               g,n,T);
    W(W<1e-3)=0;
    jj=jj+1;
% Roulette (for energy conservation)
     ro=rand(N,1)<(1/10);
     W(ro)=W(ro)*10;
     W(~ro)=0;
end
```

### CM - Definition of the current medium

This function recalled in the main program is created to define the layer in which photons currently lie. Layers in the tissue are labeled with integer numbers; the current medium represents this integer for each photon at each step, so that the corresponding properties of the tissue are easily accessible. Photons which cross the deeper boundary are considered dead and their weight is recorded into the total amount of absorbed energy.

```
function [cm,W,energy]=CM(N,W,pos,Nt,boundaries,energy)
     cm=ones(N,1);
     cm(pos(:,3)<=boundaries(1))=1;
     for k=2:Nt+1
         cm(pos(:,3)>boundaries(k-1)& pos(:,3)<=boundaries(k))=k;
     end
     energy=energy+sum(W(pos(:,3)>=boundaries(end)));
     W(pos(:,3)>=boundaries(end))=0;
```

### PT - Photon Transport Function

This function defines the path of photons inside the skin-hair structure. Essentially, it divides all the possible interaction points into two big sets: those on the boundary and those others inside a layer. The first implies that the photon is either reflected or transmitted, while when the step size doesn't make the photon reach the boundary, the step is still inside the layer. The photon loses a part of the weight and changes its direction due to the interaction with the matter.

```
function [pos,W,D,s,energy,RF,T]=PT(N,W,D,boundaries,s,mua,mus,pos,cm,energy,RF,
                                    Nt,g,n,T)
    mut=mua+mus;
    sts=zeros(N,1);
    DW=zeros(N,1);
    s(s==0)=-log(rand(sum(s==0),1));
    [d,W,RF]=Dist(N,boundaries,D,pos,W,cm,RF);
```

Hit the boundary? NO -> [move, absorbe, scatter]

```
nhi=(d.*(mut(cm))'>s);
nhit=nhi & W~=0;
sts(nhit)=s(nhit)./mut(cm(nhit))';
pos(nhit,:)=[pos(nhit,1)+D(nhit,1).*sts(nhit),...
    pos(nhit,2)+D(nhit,2).*sts(nhit),pos(nhit,3)+D(nhit,3).*sts(nhit)];
[cm,W,energy]=CM(N,W,pos,Nt,boundaries,energy);
s(nhit)=0;
DW(nhit)=W(nhit).*mua(cm(nhit))'./mut(cm(nhit))';
W(nhit)=W(nhit)-DW(nhit);
D=scatt(N,D,g,cm,nhit);
```

Hit the boundary? YES -> [move to the boundary, reflect/transmit]

```
hit=(~nhi)& (W~=0);
pos(hit,:)=[pos(hit,1)+D(hit,1).*d(hit),...
    pos(hit,2)+D(hit,2).*d(hit),pos(hit,3)+D(hit,3).*d(hit)];
[cm,W,energy]=CM(N,W,pos,Nt,boundaries,energy);
[W,D,T,tr]=Rfl(N,W,D,n,cm,hit,T);
s(tr)=(s(tr)-d(tr))./(mut(cm(tr)+1))';
pos(tr,:)=[pos(tr,1)+D(tr,1).*s(tr),...
    pos(tr,2)+D(tr,2).*s(tr),pos(tr,3)+D(tr,3).*s(tr)];
```

For each photon a random step size and the distance from the boundary are calculated. From the comparison of these two quantities, two scenarios are possible:

- Hit the boundary: the photons move to the boundary and the remaining step length is recorded. At this point the photons can be subjected to reflection or transmission: those reflected (see reflection) while those transmitted terminate their step.
- Don't reach the boundary: in this case they move of a step of the random size along their own direction and the current medium is updated according to their new positions.

At the interaction site their weight is decreased for absorption and their direction is changed by the scattering events.

### Dist Photon - boundary distance computation

Function computing the distance between the actual interaction point and the layer the photon is directed to.

```
function [dd,W,RF]=Dist(N,boundaries,D,pos,W,cm,RF)
    RF=RF+sum(W(D(:,3)<0 & cm==1));
    W(D(:,3)<0 & cm==1)=0;
    dd=zeros(N,1);
    ne=(D(:,3))<0;
    neg=ne&(W~=0);
    po=(~ne)&(W~=0);
    dd(D(:,3)==0)=inf;
    dd(neg)=abs(pos(neg,3)-boundaries(cm(neg)-1).')./D(neg,3);
    dd(po)=abs(boundaries(cm(po)).'-pos(po,3))./D(po,3);
```

- the distance is computed between the photon and the nearest boundary, inwards if the direction is positive; outwards if the direction is negative;
- Those photons which are in the ambient medium directed outwards (with respect to the tissue) are considered dead since they will never interact with the tissue again. Their weight is recorded under the variable RF.

### Rfl - Photon Reflection Probability

This function computes the specular reflectance $R_{sp}$ and according to a random generated number from a uniform distribution decides whether the photons are transmitted or reflected.

```
function [W,D,T,tr]=Rfl(N,W,D,n,cm,hit,T)

    Rsp=zeros(N,1);
    hit=hit.';
    ai=acos(abs(D(:,3)));
    ai=ai.';
    ac=asin(n(cm+1)./n(cm));
    at=asin(sin(ai).*n(cm)./n(cm+1));
    Rsp(ai>=ac & hit)=1;
    Rs=(n(cm).*cos(ai)-n(cm+1).*cos(at)).^2./(n(cm).*cos(ai)+n(cm+1).*cos(at)).^2;
    Rp=(n(cm).*cos(at)-n(cm+1).*cos(ai)).^2./(n(cm).*cos(at)+n(cm+1).*cos(ai)).^2;
    Rsp(ai>0 & ai<ac & hit)=(Rs(ai>0 & ai<ac & hit)+Rp(ai>0 & ai<ac & hit))./2;
    Rsp(ai==0 & hit)=(n(cm(ai==0&hit))-n(cm(ai==0&hit)+1)).^2./(n(cm(ai==0&hit))+
                    +n(cm(ai==0&hit)+1)).^2;
    rf=(rand(N,1)<=Rsp);
    rf=rf.';
    D(rf&hit,3)=-D(rf&hit,3);
    W(rf&hit)=W(rf&hit).*(Rsp(rf&hit));
    tr=(~rf)&hit;
    W(tr)=W(tr).*(1-Rsp(tr));
    D(tr,:)=[D(tr,1).*n(cm(tr)).'./n(cm(tr)+1).',...
             D(tr,2).*n(cm(tr)).'./n(cm(tr)+1).',...
             cos(at(tr)).'.*sign(D(tr,3))];
```

- $\alpha_i$ is the angle of incidence which is that realted to the cosine directors D;
- $\alpha_t$ is the angle of transmission according to Snell's law

$$n_i \sin(\alpha_i) = n_t \sin(\alpha_t)$$

  where $n_i$ and $n_t$ are the refraction indices of the layers from which the photon comes and to which it is directed;

- $\alpha_c$, is the critical angle. Photons with any bigger angle of incidence are totally reflected;
- the specular reflectance is computed according to Fresnel law

$$R_{sp} = \frac{1}{2}\Big(\frac{n_i \cos(\alpha_i) - n_t \cos(\alpha_t)}{n_i \cos(\alpha_i) + n_t \cos(\alpha_t)} + \frac{n_i \cos(\alpha_t) - n_t \cos(\alpha_i)}{n_i \cos(\alpha_t) + n_t \cos(\alpha_i)}\Big)$$

- after the pseudorandom is generated, each photon is tagged as reflected (doesn't change position, opposite z-direction and decreased weight) or transmitted (it finishes the step it was supposed to do).

### scatt - Definition of the random direction for the next step

This function computes the random changes in direction of photons because of the interaction with the matter. When $g = 0$ the choice is completely random while in the other cases the direction is determined by the Henvey-Greenstein phase function.

```
function D=scatt(N,D,g,cm,nhit)
    theta=zeros(N,1);
     % if g==0
```

```
    costheta(g(cm)==0)=2*rand(sum(g(cm)==0),1)-1;
    theta(g(cm)==0)=acos(costheta(g(cm)==0));
     % g~=0
    any=(g(cm)~=0);
    ca=rand(N,1);
    theta(g(cm)~=0)=acos((1/2*g(cm(any)).*(1+g(cm(any)).^2+
              -((1-g(cm(any)).^2)./(1-g(cm(any))+2*g(cm(any)).*ca(any)')).^2)));
    costheta(g(cm)~=0)=cos(theta(g(cm)~=0));
    phi=2*pi*rand(N,1);
    % update scattered directions
    co=ones(N,1);
    a=sign(D(:,3));
    D(co&nhit,1)=sin(theta(co&nhit)).*cos(phi(co&nhit));
    D(co&nhit,2)=sin(theta(co&nhit)).*sin(phi(co&nhit));
    D(co&nhit,3)=a(co&nhit).'.*costheta(co&nhit);
```

## C.2 Multiple Linear Regression for prediction of treatment efficacy

Predictive platform for the forecast of treatment efficacy. We randomly divide the data set into two subsets: the regression model is fit on 70% of data, while the remaining 30% is used to test the generalizing power of the model. The predictors are chosen according to a stepwise algorithm

```
  Eff/t = b_0 - b_1 den - b_2 N. Tr - b_3 loc - b_4 col
        + b_5 log(DI) - b_6 den * den + b_7 N. Tr *N. Tr
        + b_8 den * N. Tr + b_9 loc * col
```

The goodness of the model is evaluated through the correlation with measured data. Note: the damage integral is obtained with $\Lambda = 74$ and $Tc = 326.75$.

```
[num,str,cases]=xlsread('dataset.xlsx');
global a
a=133;
EF=cell2mat(cases(2:(a+1),20));
Den=cell2mat(cases(2:(a+1),4));
Ntr=cell2mat(cases(2:(a+1),18));
Loc=cell2mat(cases(2:(a+1),30));
Col=cell2mat(cases(2:(a+1),29));
DI=cell2mat(cases(2:(a+1),31));
FL=cell2mat(cases(2:(a+1),9));
FWHM=cell2mat(cases(2:(a+1),10));

y=EF./Ntr;
ind=1:a;
NN=floor(133*0.7);
TrIndex=datasample(ind,NN,'replace',false);
p=1;
for k=1:a
    if sum(TrIndex==k)==0
        TestIndex(p)=k;
        p=p+1;
    end
end
```

```
LogDI=log(DI);
X=[ones(size(EF)) Den Ntr Loc Col LogDI Den.^2 Ntr.^2 Den.*Ntr Loc.*Col];
[b,bint,r,rint,stats]=regress(y(TrIndex),X(TrIndex,:));
% stats=[R^2 F-statistics p-value estimate of the error variance]
PredEf=b(1)*ones(size(EF(TrIndex)))+b(2)*Den(TrIndex)+b(3)*Ntr(TrIndex)+
      +b(4)*Loc(TrIndex)+b(5)*Col(TrIndex)+b(6)*LogDI(TrIndex)+
      +b(7)*(Den(TrIndex).^2)+b(8)*(Ntr(TrIndex).^2)
      +b(9)*(Den(TrIndex).*Ntr(TrIndex))+b(10)*(Loc(TrIndex).*Col(TrIndex));
figure
plot(y(TrIndex),PredEf,'.',y(TrIndex),y(TrIndex),'green',y(TrIndex),y(TrIndex)+
                           +2*stats(4),'r',y(TrIndex),y(TrIndex)-2*stats(4),'r')
legend('Predicted Efficacy','Target Efficacy','Prediction interval')
title('Train set')
xlabel('Target efficacy')
hold off
Correl_training=corr(PredEf,y(TrIndex));
```

### Testing the multilinear model on the testing set of data

```
PredEf_test=b(1)*ones(size(EF(TestIndex)))+b(2)*Den(TestIndex)+
           +b(3)*Ntr(TestIndex)+b(4)*Loc(TestIndex)+b(5)*Col(TestIndex)+
           +b(6)*LogDI(TestIndex)+b(7)*(Den(TestIndex).^2)+
           +b(8)*(Ntr(TestIndex).^2)+ b(9)*(Den(TestIndex).*Ntr(TestIndex))+
           +b(10)*(Loc(TestIndex).*Col(TestIndex));
figure
plot(y(TestIndex),PredEf_test,'.',y(TestIndex),y(TestIndex),'green',
     y(TestIndex),y(TestIndex)+2*sqrt(stats(4)),'r',
     y(TestIndex),y(TestIndex)-2*sqrt(stats(4)),'r')
legend('Predicted Efficacy','Target Efficacy','Prediction interval')
title('\bf{Test set}')
xlabel('Target efficacy')
Correl_test=corr(PredEf_test,y(TestIndex));
```

## C.3 GUI for predictive analysis

The Graphical User Interface (GUI) for efficacy prediction adapts a multiple linear regression model to a set of data and checks its goodness. First, it requires the selection of the file containing clinical data to be analysed; after running the application, it is enough to select the file to open. Afterwards, it requires as input

- *N. cases* - the number of clinical trials which were performed;
- *Training Percentage* the part of the clinical set to be used for the fitting of the model to data (for estimating the coefficients). The complementary part of the data set is then used for testing.

Then, the file is complete of all the needed information and can be used: pressing on the button 'Train' the model is fitted and the $R$ squared of the model together with the correlation between predicted and measured data in training is shown. The plot shows on the horizontal axis the target efficacy, the green line is the perfect fit, the blue dots are the predictions while the red lines are a 95% prediction interval.

Also, the model shows the weights corresponding to each predictor.

Pressing on the button 'Test', we can show instead the result in training, seeing the correlation between measured and predicted data and the graphic visualization of the result (with the same notations used in training).

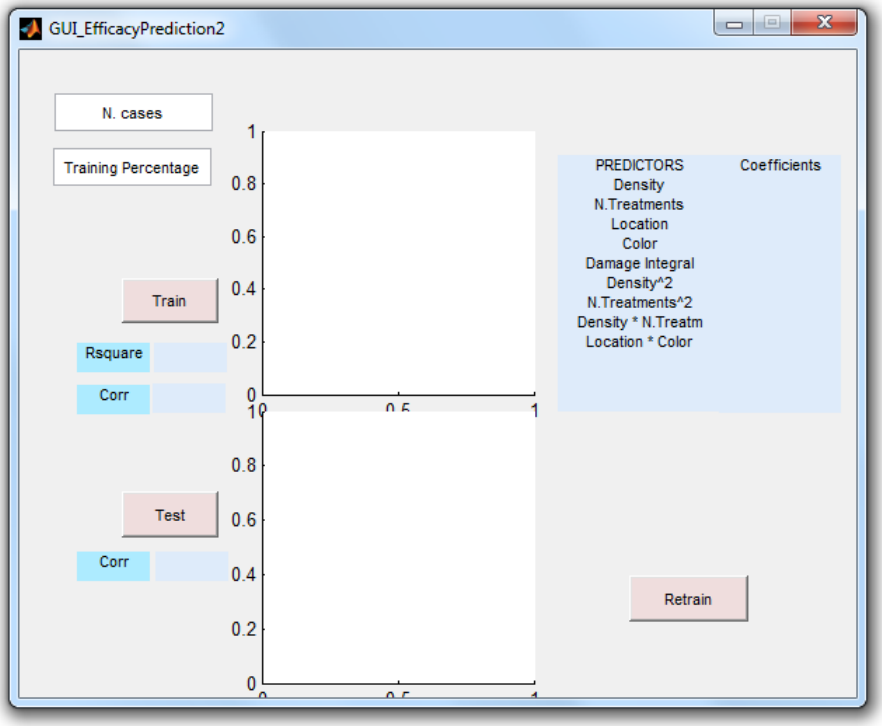
GUI_EfficacyPrediction2
N. cases
Training Percentage
Train
Rsquare
Corr
Test
Corr
PREDICTORS
Coefficients
Density
N.Treatments
Location
Color
Damage Integral
Density^2
N.Treatments^2
Density * N.Treatm
Location * Color
Retrain

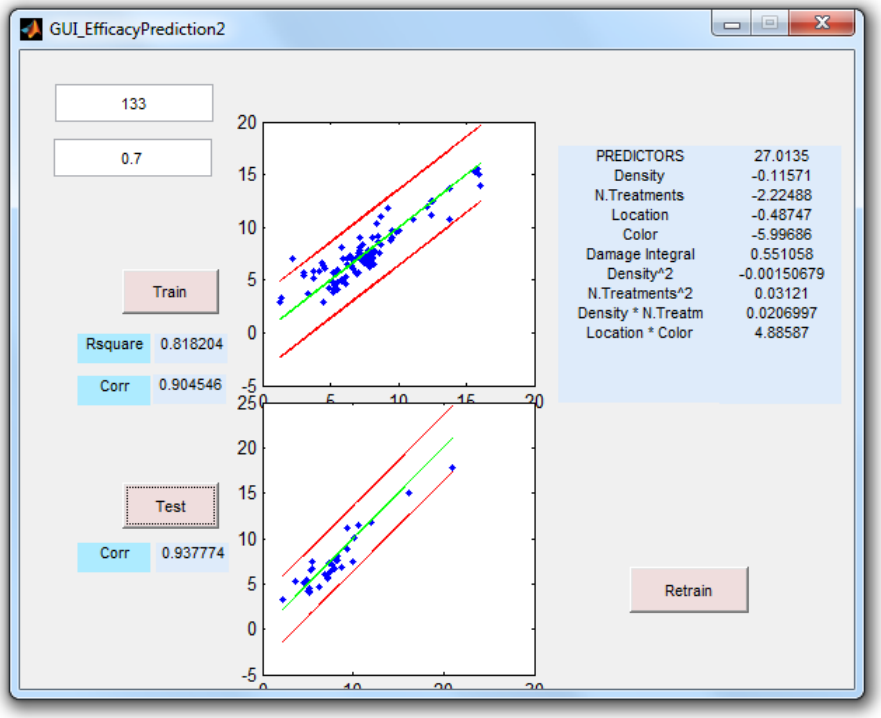
GUI_EfficacyPrediction2
133
0.7
Train
Rsquare 0.818204
Corr 0.904546
Test
Corr 0.937774
PREDICTORS 27.0135
Density -0.11571
N.Treatments -2.22488
Location -0.48747
Color -5.99686
Damage Integral 0.551058
Density^2 -0.00150679
N.Treatments^2 0.03121
Density * N.Treatm 0.0206997
Location * Color 4.88587
Retrain

Finally, it is possible to retrain the model. it means that we can look for a better model simply re-sampling the random subset for training and testing, but with the same percentage. the result in training is automatically shown while the testing must be specifically required.

## C.4 Artificial neural network

In parallel to the multiple linear regression, we build an artificial neural network using the same predictors. This is done on the statistical software R.

```
library(XLConnect)
Tdata<-readWorksheet(loadWorkbook("dataset.xlsx"),sheet=1)
library(nnet)
require(caret)

norm.fun=function(x){(x-min(x))/(max(x)-min(x))}
DD<-Tdata[,c('Highest.Efficacy....','Fluence','Density','No..of.treatm',
             'Damage.Integral','FWHM','colnum','locnum')]
target<-Tdata[,'Highest.Efficacy....']/Tdata[,'No..of.treatm']

logdi<- log(Tdata[,'Damage.Integral'])
DensitySquare<- ((Tdata[,'Density'])^2)
NtSquare<-(Tdata[,'No..of.treatm'])^2
DensityNt<-(Tdata[,'Density'])*(Tdata[,'No..of.treatm'])
LocCol<-(Tdata[,'locnum'])*(Tdata[,'colnum'])

input<-cbind(DD,target,logdi,DensitySquare,NtSquare,DensityNt,LocCol)
input<-as.data.frame(input)

trainIndex<-createDataPartition(input$target,p=0.7,list=F)
data.norm=apply(input,2,norm.fun)
target=as.data.frame(target)
target.norm=apply(target,2,norm.fun)
Dtrain<-data.norm[trainIndex,]
Dtest<-data.norm[-trainIndex,]

netnorm=nnet(target~Density+No..of.treatm+colnum+logdi+locnum+DensitySquare+LocCol+
             +DensityNt+NtSquare,data=Dtrain,size=10,decay=0.1)
actual=target.norm[-trainIndex]
predicted=predict(netnorm,Dtest)

# prediction on training data (correlation~80%)
  acc=target.norm[trainIndex]
  pre=predict(netnorm,Dtrain)

  plot(acc,pre,main="Training set",xlab="Target efficacy",ylab="Predicted efficacy")
  cor(actual,predicted)
  title('Training set')

# prediction on testing data (correlation~70%)
plot(actual, predicted)
cor(actual,predicted)
title('Test set')

RMSE<- sqrt(mean((predicted - actual)^2))
```

```
net.predict<-predict(netnorm,target[-trainIndex])
# net.predict<-compute(netnorm,target[-trainIndex])

# WEIGHTS OF THE NETWORK
netnorm$wts

# (number of) NODES OF THE NETWORK
netnorm$n

# VARIABLE IMPORTANCE IN THE NEURAL NETWORK
library(devtools)
gar.fun(netnorm$wts,netnorm)
vals.only <- unlist(gar.fun('y', netnorm, wts.only = T))
p1 <- gar.fun('Efficacy',vals.only, struct = c(8,8,1))
```

# Bibliography


[1] J. Lepselter and M. Elman, "Biological and clinical aspects in laser hair removal," *Journal of Dermatological Treatment*, vol. 15(2), pp. 72–83, 2004.

[2] G. S. Ahluwalia, *Cosmetic Applications of Laser and Light-Based Systems.* Norwich, USA: William Andrew Inc, 2009.

[3] A. J. Welch and M. J. C. van Gemert, *Optical-thermal Response of Laser-irradiated Tissue.* Springer, 2 ed., 2011.

[4] L. V. Wang and H. Wu, *Biomedical Optics. Principles and Imaging.* Wiley Interscience, 2007.

[5] L. Wang, S. L. Jacques, and L. Zheng, "MCML - Monte Carlo modeling of light transport in multi-layered tissues," *Computer Methods and Programs in Biomedicine*, vol. 47(2), pp. 131–146, 1995.

[6] J. A. J. v. Belkum, "Monte Carlo simulation of photon transport in tissue," *Master Thesis TU/e - Philips*, 2008.

[7] M. H. Niemz, *Laser-Tissue Interactions. Fundamentals and Applications.* Biological and Medical Physics, Biomedical Engineering, Springer, 2003.

[8] COMSOL Multiphysics, *Introduction to COMSOL Multiphysics.* 2011.

[9] R. Steiner, D. Russ, W. Falkenstein, and A. Kienle, "Optimization of laser epilation by simulation of the thermal laser effect," *Laser Physics*, vol. 11, pp. 146–153, 2001.

[10] K. G. Klavuhn and D. Green, "Importance of cutanoeus cooling during photothermal epilation: Theoretical and practical considerations," *Laser Surgery and Medicine*, vol. 31, pp. 97–105, 2002.

[11] G. Cotsarelis, T. Sun, and R. M. Lavker, "Label-retaining cells reside in the bulge area of pilosebaceous unit: Implications for follicular stem cells, hair cycle and skin carcinogenesis," *Cell*, vol. 61(7), 1990.

[12] N. Randall and V. A. Botchkareva, *The Biology of Hair Growth. Cosmetic Applications of Laser and Light-Based Systems.* William Andrew Inc., 2009.

[13] X. Wang, Y. Shi, Q. Zhou, X. Liu, S. Xu, and T. Lei, "Detailed histological structure of human hair follicle bulge region at different ages: A visible niche for nesting adult stem cells," *Journal of Huazhong University of Science and Technology*, vol. 32(5), pp. 648–656, 2012.

[14] H. H. Pennes, "Analysis of tissue and arterial blood temperatures in the resting human forearm," *Journal of Applied Physiology*, no. 2, pp. 93–122, 1997.

[15] B. Chen and S. L. Thomsen, "Modeling thermal damage in skin from 2000-nm laser irradiation," *Journal of Biomedical Optics*, vol. 11(6),064028, 2006.

[16] M. Jasinski, "Numerical modeling of tissue coagulation during laser irradiation controlled by surface temperature," *Scientific Research of the Institute of Mathematics and Computer science*, pp. 29–36, 2010.

[17] J. P. Abraham and E. M. Sparrow, "A thermal-ablation bioheat model including liquid-to-vapor phase change, pressure- and necrosis-dependent perfusion, and moisture-dependent properties," *International Journal of Heat and Mass Transfer*, vol. 50, pp. 2537–2544, 2007.

[18] Y. Sato and B. Niceno, "A sharp-interface phase change model for a mass-conservative interface tracking method," *Journal of Computational Physics*, vol. 249, pp. 127–161, 2013.

[19] W. Shen and J. Zhang, "Modeling and numerical simulation of bioheat transfer and biomechanics in soft tissue," *Mathematical Computer and Modelling*, vol. 41, pp. 1251–1265, 2005.

[20] A. J. Welch, E. H. Wissler, and L. A. Priebe, "Significance of blood flow in calculations of temperature in laser irradiated tissue," *Biomedical Engineering*, vol. 27(3), pp. 164–166, 1980.

[21] J. W. Tunnell, L. V. Wang, and B. Anvari, "Optimum pulse duration and radiant exposure for vascular laser therapy of dark port-wine skin: a theoretical study," *Applied Optics*, vol. 42(7), pp. 1367–1378, 2003.

[22] M. Gales, "Multi-layer perceptron: Introduction and training," *Advanced Pattern Processing. University of Cambridge*, vol. Paper I10, 2013.

[23] L. C. Evans, *Partial Differential Equations*. Providence: American Mathematical Society, 1998.

[24] W. W.-Y. Wong, "Lecture notes on Sobolev spaces for CCA," *Department of Pure Mathematics and Mathematical Statistics, University of Cambrige (UK)*, 2010.

[25] S. A. Baldwin, A. Pelman, and J. L. Bert, "A heat transfer model of thermal balloon endometrial ablation," *Annals of Biomedical Engineering*, vol. 29, pp. 1009–1018, 2001.

[26] W. A. Adkins and M. G. Davidson, *Ordinary Differential Equations*. Undergraduate Texts in Mathematics, Springer, 2010.

[27] S. Meier and M. Bohm, "Parameter identification for a two-scale model of reactive transport in porous media - some first steps," *Journal of Applied Mathematics and Mechanics*, vol. 7, p. 1061003–1061004, 2007.

[28] F. T. Akyildiz, S. Tatar, and S. Ulusoy, "Existence and uniqueness for a nonlinear inverse reaction-diffusion problem with a nonlinear source in higher dimensions," *Mathematical Methods in the Applied Sciences*, vol. 36, pp. 2397–2402, 2013.

[29] P. Duchateau, "Monotonicity and uniqueness results in identifying an unknown coefficient in a nonlinear diffusion equation," *SIAM Journal on Applied Mathematics*, vol. 41, pp. 310–323, 1981.

[30] A. E. Badia and T. H. Duong, "On an inverse source problem for the heat equation. application to a pollution detection problem," *Journal of Inverse Ill-Posed Problems*, vol. 10, pp. 585–599, 2002.

[31] Z. Wang and J. Liu, "Identification of the pollution source from one-dimensional parabolic equations models," *Applied Mathematics and Computation*, vol. 219, pp. 3403–3413, 2012.

[32] P. Cenac, B. Chauvin, S. Herrmann, and P. Vallois, "Persistent random walks, variable length Markov chains and piecewise deterministic Markov processes," 2012.

[33] N. Otberg, H. Ritcher, H. Schaefer, U. Blume-Peytavi, W. Sterry, and J. Lademann, "Variations of hair follicle size and distribution in different body sites," *Journal of Investigative Dermatology*, vol. 122, pp. 14–19, 2003.

[34] D. J. Goldberg, *Laser and Lights: Rejuvenation, Resurfacing, Hair Removal, Treatment of Ethnic Skin*, vol. 2. Elservier Saunders, 2005.

[35] Y. Dutil, D. R. Rousse, N. B. Salah, S. Lassue, and L. Zalewski, "A review on phase-change materials: Mathematical modeling and simulations," *Renewable and Sustainable Energy Reviews*, vol. 15, p. 112–130.

[36] M. J. van Gemert, S. L. Jacques, H. J. Sterenborg, and W. M. Star, "Skin optics," *IEEE Trans Biomed Eng*, vol. 36, 1989.

[37] E. Salomatina, B. Jiang, J. Novak, and A. N. Yaroslavsky, "Optical properties of normal and cancerous human skin in the visible and near-infrared spectral range," *Journal of Biomedical Optics*, vol. 11(6):064026, 2006.

[38] F. C. Henriques Jr, "Studies of thermal injury; the predictability and the significance of thermally induced rate processes leading to irreversible epidermal injury," *Archives of Pathology*, vol. 43(5), pp. 489–502, 1947.

[39] A. Muntean, "Continuity with respect to data and parameters of weak solutions to a Stefan-like problem," *Acta Math. Univ. Comenianae*, vol. 78, pp. 205–222, 2009.

[40] J. Naumann, "On a class of weakly nonlinear parabolic equations," *Seminarberichte, Humboldt-Universitat zu Berlin. Sektion Mathematik*, 1979.

[41] H. Brézis, "Some degenerate nonlinear parabolic problems," *Proceedings Symposium Pure Mathematics*, vol. 18/I, pp. 28–38, 1970.

[42] A. Quarteroni, *Modellistica Numerica per Problemi Differenziali.* Springer-Verlag, 2008.

[43] A. Muntean and M. Ness-Radu, "A multiscale Galerkin approach for a class of nonlinear coupled reaction-diffusion systems in complex media," *Journal of Mathematical Analysis and Applications*, vol. 371, pp. 705–718, 2010.

[44] Y. Fan and I. S. Pop, "A class of pseudo-parabolic equations: Existence, uniqueness of weak solutions, and error estimates for the Euler-implicit discretization," *Mathematical Methods in the Applied Sciences*, vol. 34(18), 2010.

[45] I. S. Pop and B. Schweizer, "Regularization schemes for degenerate Richards equations and outflow conditions," *Mathematical Models and Methods in Applied Sciences*, vol. 21, pp. 1685–1712, 2011.